



University of Kentucky
UKnowledge

University of Kentucky Doctoral Dissertations

Graduate School

2007

Computer Simulation and Modeling of Physical and Biological Processes using Partial Differential Equations

Wensheng Shen
University of Kentucky, wensheng@csr.uky.edu

[Right click to open a feedback form in a new tab to let us know how this document benefits you.](#)

Recommended Citation

Shen, Wensheng, "Computer Simulation and Modeling of Physical and Biological Processes using Partial Differential Equations" (2007). *University of Kentucky Doctoral Dissertations*. 501.
https://uknowledge.uky.edu/gradschool_diss/501

This Dissertation is brought to you for free and open access by the Graduate School at UKnowledge. It has been accepted for inclusion in University of Kentucky Doctoral Dissertations by an authorized administrator of UKnowledge. For more information, please contact UKnowledge@lsv.uky.edu.

ABSTRACT OF DISSERTATION

Wensheng Shen

The Graduate School
University of Kentucky
2007

COMPUTER SIMULATION AND MODELING OF
PHYSICAL AND BIOLOGICAL PROCESSES USING
PARTIAL DIFFERENTIAL EQUATIONS

ABSTRACT OF DISSERTATION

A dissertation submitted in partial fulfillment of the
requirements for the degree of Doctor of Philosophy in the
College of Engineering
at the University of Kentucky

By

Wensheng Shen

Lexington, Kentucky

Director: Jun Zhang, Ph.D., Professor of Computer Science

Lexington, Kentucky

2007

Copyright © Wensheng Shen 2007

ABSTRACT OF DISSERTATION

COMPUTER SIMULATION AND MODELING OF PHYSICAL AND BIOLOGICAL PROCESSES USING PARTIAL DIFFERENTIAL EQUATIONS

Scientific research in areas of physics, chemistry, and biology traditionally depends purely on experimental and theoretical methods. Recently numerical simulation is emerging as the third way of science discovery beyond the experimental and theoretical approaches. This work describes some general procedures in numerical computation, and presents several applications of numerical modeling in bioheat transfer and biomechanics, jet diffusion flame, and bio-molecular interactions of proteins in blood circulation.

A three-dimensional (3D) multilayer model based on the skin physical structure is developed to investigate the transient thermal response of human skin subject to external heating. The temperature distribution of the skin is modeled by a bioheat transfer equation. Different from existing models, the current model includes water evaporation and diffusion, where the rate of water evaporation is determined based on the theory of laminar boundary layer. The time-dependent equation is discretized using the Crank-Nicolson scheme. The large sparse linear system resulted from discretizing the governing partial differential equation is solved by GMRES solver.

The jet diffusion flame is simulated by fluid flow and chemical reaction. The second-order backward Euler scheme is applied for the time dependent Navier-Stokes equation. Central difference is used for diffusion terms to achieve better accuracy, and a monotonicity-preserving upwind difference is used for convective ones. The coupled nonlinear system is solved via the damped Newton's method. The Newton Jacobian matrix is formed numerically, and the resulting linear system is ill-conditioned and is solved by Bi-CGSTAB with the Gauss-Seidel preconditioner.

A novel convection-diffusion-reaction model is introduced to simulate fibroblast growth factor (FGF-2) binding to cell surface molecules of receptor and heparan sulfate proteoglycan and MAP kinase signaling under flow condition. The model includes three parts: the flow of media using incompressible Navier-Stokes equation, the transport of FGF-2 using a convection-diffusion transport equation, and the local binding and signaling by chemical kinetics. The whole model consists of a set of coupled nonlinear partial differential equations (PDEs) and a set of coupled nonlinear

ordinary differential equations (ODEs). To solve the time-dependent PDE system, we use second order implicit Euler method by finite volume discretization. The ODE system is stiff and is solved by an ODE solver VODE using backward differencing formulation (BDF). Findings from this study have implications with regard to regulation of heparin-binding growth factors in circulation.

KEYWORDS: Numerical simulation, partial differential equations, bioheat transfer, laminar diffusion flame, fibroblast growth factor

Wensheng Shen

May 15, 2007

COMPUTER SIMULATION AND MODELING OF
PHYSICAL AND BIOLOGICAL PROCESSES USING
PARTIAL DIFFERENTIAL EQUATIONS

By

Wensheng Shen

Jun Zhang, Ph.D.
Director of Dissertation

Grzegorz W. Wasilkowski, Ph.D.
Director of Graduate Studies

May 15, 2007
Date

DISSERTATION

Wensheng Shen

The Graduate School
University of Kentucky
2007

COMPUTER SIMULATION AND MODELING OF
PHYSICAL AND BIOLOGICAL PROCESSES USING
PARTIAL DIFFERENTIAL EQUATIONS

DISSERTATION

A dissertation submitted in partial fulfillment of the
requirements for the degree of Doctor of Philosophy in the
College of Engineering
at the University of Kentucky

By

Wensheng Shen

Lexington, Kentucky

Director: Jun Zhang, Ph.D., Professor of Computer Science

Lexington, Kentucky

2007

Copyright © Wensheng Shen 2007

ACKNOWLEDGEMENTS

It took about four years for the author to finish this dissertation. During his years of study at UKY, the author encountered many difficulties in life and study, and was once deeply worried about the possibility of completing his Ph.D. degree in Computer Science. Thanks for all kinds of support, help, and encouragement from many people, fortunately the author is managed to finish his thesis.

First of all, the author would like to thank his faculty advisor, Dr. Jun Zhang, who has inspired and encouraged him to conduct research in computer modeling and simulation, and led him to the area of computational biology. Dr. Zhang has been a great mentor on every account, and his broad knowledge and constructive suggestions to this dissertation are sincerely appreciated.

The author would like to thank other faculty members of his Advisory Committee: Dr. Fuhua (Frank) Cheng (Department of Computer Science), Dr. Grzegorz W. Wasilkowski (Department of Computer Science) and Dr. Fuqian Yang (Department of Chemical and Materials Engineering), for their insightful comments and useful suggestions on this work. The author would also like to thank the outside examiner Dr. James M. McDonough (Department of Mechanical Engineering) for taking the time to review this document and his helpful comments on this dissertation.

The author would like to express his appreciation to his research collaborators, Dr. Michael Fannon, Department of Ophthalmology and Visual Sciences, College of Medicine, University of Kentucky, Dr. Kimberly Forsten-Williams, Department of Chemical Engineering, Virginia Polytechnic Institute and State University, for their invaluable comments to this dissertation and interesting introduction in biology, Dr. Fuqian Yang, Department of Chemical and Materials Engineering, University of Kentucky, and Dr. Jing Liu, Cryogenics Laboratory, Technical Institute of Physics and Chemistry, Chinese Academy of Sciences, for collaboration in bioheat transfer.

Thanks also go to all members in the Laboratory for High Performance Scientific

Computing & Computer Simulation, Dr. Chi Shen, Dr. Jeonghwa Lee, Dr. Shuting Xu, Dr. Ning Kang, Ms. Eun-Joo Lee, Ms. Jie Wang, Mr. Ning Cao, Mr. Hao Ji, Mr. Yin Wang, Mr. Dianwei Han, Mr. Cheng Qin, Mr. Zhenmin Lin, Mr. Qi Zhuang, Ms. Beibei Li, Mr. Changjiang Zhang, Mr. Xuwei Liang, and Mr. Lian Liu, for helpful discussions and creating a friendly working environment together.

Finally the author would like to thank his family members. The author needs to thank his parents for giving him life and their continuous support of his education in his middle school, high school, and university studies. The author would like to thank his sister and brother for their efforts trying to make his life and study easier. Most important, the author should thank his wife, Hongyan Zhang, his daughter, Shirley, and his son, James for their endless love, ever-lasting support, and great patience during his graduate study in Lexington, KY toward a Ph.D. degree in Computer Science, his second Ph.D. degree.

The author would like to express his gratitude to the funding agencies that have provided financial support. The research work with this dissertation was supported in part by:

- U.S. National Science Foundation (NSF).
- U.S. National Institutes of Health (NIH).
- Kentucky Science and Engineering Foundation (KSEF).

Table of Contents

Acknowledgements	iii
List of Tables	vii
List of Figures	viii
List of Files	xii
1 Introduction	1
1.1 Motivation	1
1.2 Modeling Procedure	2
1.3 Solution Methods	4
2 Iterative Methods and Effective Preconditioners	7
2.1 Direct Methods	7
2.2 Stationary Iterative Methods	8
2.3 Krylov Subspace Based Iterative Methods	12
2.4 Multigrid Methods	15
2.5 Preconditioners	17
3 Bioheat Transfer and Biomechanics in Soft Tissue	22
3.1 Introduction	22
3.2 Constitutive Equations	24
3.2.1 Heat transfer process	24
3.2.2 Stress, strain, and displacement evolution	25
3.3 Numerical Techniques	28
3.3.1 Finite difference discretization	28
3.3.2 Iterative solver	29
3.4 Numerical Experiments and Discussion	31
3.4.1 Case study: hyperthermia model	31
3.4.2 Case study: sinusoidal surface heating model	35
3.4.3 Computational Performance	37
3.5 Summary	40
4 Thermal Response of Skin Subject to Laser Heating	42
4.1 Introduction	42
4.2 The Multilayer Model	44
4.3 Water Evaporation and Diffusion	47
4.4 Numerical Scheme and Solution Strategy	50
4.5 Stability Analysis	53
4.6 Numerical Experiments and Discussions	54
4.7 Summary	63

5	Thermal Injury Prediction with Strain Energy	65
5.1	Introduction	65
5.2	Thermal Stress and Deformation	66
5.3	Thermal Injury Prediction	68
5.4	Numerical Algorithm and Solution Procedure	69
5.5	Numerical Experiments and Discussions	70
5.6	Summary	77
6	Steady and Unsteady Diffusion Flame Solver	79
6.1	Introduction	79
6.2	Laminar Diffusion Flame Model	80
6.2.1	Vorticity-Velocity Formulation	80
6.2.2	Flame Sheet Model	81
6.2.3	Boundary Conditions	83
6.3	Newton's Method	83
6.4	Finite Difference Approximation and Linear Solver	86
6.5	Results and Discussion	87
6.6	Summary	93
7	Protein Transport in Capillary with Competitive Binding and Signaling . .	94
7.1	Introduction	94
7.2	Incompressible Navier-Stokes Equations	98
7.3	Transport Equation of FGF-2	99
7.4	Competitive Binding Kinetics	102
7.5	Numerical Procedure	106
7.6	Results	106
7.6.1	Media flow in artificial capillary	106
7.6.2	Ligand transport and binding at 4 °C	111
7.6.3	Ligand transport and binding at 37 °C	117
7.6.4	The effect of flow on ligand transport	122
7.7	Discussion	125
7.8	Summary	130
8	Conclusion and Future Work	132
8.1	Conclusion	132
8.2	Future Work	135
	Appendix	138
	Bibliography	139
	Vita	150

List of Tables

3.1	Thermal physical properties used in this computation.	24
3.2	Nomenclature for symbols used in Eq. (5.1).	27
3.3	Information on the coefficient matrix A for various mesh sizes (hyperthermia).	39
3.4	Computational performance with/without ILUT at $n = 6859$ (hyperthermia).	40
3.5	Computational performance with/without ILUT at $n = 59319$ (hyperthermia).	40
4.1	Skin thickness and thermal physical properties used in this model. . .	55
7.1	Chemical reactions included in the base model using mass-action kinetics and their relevant parameters.	105

List of Figures

3.1	An illustration of the computational domain of a soft tissue.	26
3.2	The 19 point finite difference stencil defined in a unit cube.	29
3.3	Temperature distribution at $x = 0.09$ m and $t = 200$ s (hyperthermia).	33
3.4	u displacement at $x = 0.009$ m and $t = 200$ s (hyperthermia).	33
3.5	Average normal stress \tilde{P} at $x = 0.009$ m and $t = 200$ s (hyperthermia).	34
3.6	Transient temperature distribution at (0.009, 0.032, 0.04)m (hyperthermia).	35
3.7	Transient displacement distribution at (0.009, 0.032, 0.04)m (hyperthermia).	36
3.8	Transient average stress distribution \tilde{P} at (0.009, 0.032, 0.04)m (hyperthermia).	37
3.9	Transient temperature at skin surface (sinusoidal heating).	38
3.10	Transient displacement at skin surface (sinusoidal heating).	38
3.11	Transient average normal stress at skin surface (sinusoidal heating).	39
4.1	The computational domain of a soft tissue (a three layer skin).	46
4.2	The interface between two different materials.	55
4.3	3D temperature distribution of the skin subject to laser-heating with Gaussian profile at $t = 2$ s. (a) The mesh of the computational domain, uniform in the y and z directions, non-uniform in the x direction. (b) Contour plot of temperature viewed from the skin surface ($y - z$ plane at $x = 0.01208$ m). (c) Contour plot of temperature viewed from one side ($x - z$ plane at $y = 0.005$ m) of the computational domain. (d) Contour plot of temperature viewed anatomically (starting from the point $x = 0.01208$ m, $y = 0$ m, and $z = 0$ m to view the temperature distribution on the three adjacent orthogonal planes. The grids and scales are on in (a) and (b) but off in (c) and (d). The boundaries of computational domain are plotted in red. The blue color indicates the interface between epidermis and dermis, and the green color indicates the interface between dermis and subcutaneous. The parameters of the Gaussian shaped laser beam corresponding to Eq. (4.2) are $P = 12$ W, $W = 0.0025$ m, and $\mu_a = 80, 2.4,$ and 1 mm^{-1} in the epidermis, dermis and subcutaneous layers respectively.	58
4.4	The temperature change as a function of skin depth with/without evaporation.	59
4.5	The temperature history in the center of the heated region on the skin surface which is subject to periodic pulsed laser-heating for the time duration from 0 to 2 s. (a) Water evaporation and diffusion are not considered. (b) Water evaporation and diffusion are considered.	60
4.6	Water transport in skin due to temperature rise caused by periodic pulsed laser-heating for the time duration from 0 to 2 s. (a) The distribution of water content in skin in three-dimension. (b) Water content as a function of time at the point of $x = 0.01208$ m, $y = z = 0$ m.	61

4.7	Temperature and water content as a function of x along the center line ($y = z = 0$ m) at different time. (a) Temperature distribution. (b) Water content distribution.	62
4.8	The thermal response of skin due to laser-heating when cryogen spray cooling is considered. (a) 3D temperature distribution. (b) Temperature variation as a function of x	63
5.1	Two-dimensional temperature and accumulated damage plots for laser heating with a Gaussian profile. (a) Temperature ($^{\circ}\text{C}$) distribution at the base of the epidermis layer after 50 s. (b) The contour of mechanical energy (J/cm^3) at the base of the epidermis layer after 50 s. (c) The contour of accumulated damage at the base of the epidermis layer after 50 s without the consideration of mechanical energy. (d) The contour of accumulated damage at the base of the epidermis layer after 50 s with the consideration of mechanical energy. Note: in Figs. 5.1(c) and 5.1(d) the accumulated damage is scaled to $\Omega' = 1 + \lg \Omega$	74
5.2	Contour plot of accumulated damage at the base of the dermis layer after 200 s. (a) Mechanical energy is not considered (b) Mechanical energy is considered. Note: the accumulated damage is scaled to $\Omega' = 1 + \lg \Omega$	75
5.3	Time to second degree burn at the base of skin epidermis.	76
5.4	Predicted time to the third degree burn for various steam temperature.	77
6.1	A sample 9-point grid.	88
6.2	The temperature profile obtained from the steady-state equations for the diffusion flame.	92
6.3	The dependency of flame temperature on time: (a) $t = 0.025$ s, (b) $t = 0.05$ s, (c) $t = 0.075$ s, (d) $t = 0.1$ s, and (e) $t = 0.125$ s.	92
7.1	Sketch of growth factor binding to receptors and HSPG and the formation of various compounds on the surface of a capillary. The symbols in the sketch are as follows: L=FGF-2, R=FGFR, P=HSPG, C= FGF-2-FGFR complex, G=FGF-2-HSPG complex, C_2 =FGF-2-FGFR dimer, G_2 =FGF-2-HSPG dimer, T=FGF-2-FGFR-HSPG complex, and T_2 =FGF-2-FGFR-HSPG dimer.	97
7.2	Finite volume notation of control volumes in axisymmetrical coordinates.	102
7.3	The reaction network for the base model. The same symbolic representation of the species as in Fig. 7.1 is used here. Only single signaling HSPG is considered in this model. Single arrowheads indicate an irreversible reaction and double arrowhead indicate a reversible reaction. Both FGFR and HSPG can mediated signaling through T_2 [40].	104
7.4	Visualization of laminar flow in part of the artificial capillary within $x = 0 \sim 0.005$ m. (a) Flood plot of velocity u . (b) Vector plot of velocities u and v	108
7.5	Comparison of velocity profile of fully-developed laminar flow in a circular pipe between numerical and exact solutions	109

7.6	The dependency of numerical solution on mesh size, (a) at $t = 5$ minutes, (b) at $t = 10$ minutes, (c) at $t = 20$ minutes, (d) at $t = 40$ minutes, and (e) at $t = 60$ minutes, where triangles, solid line, and circles represent numerical results of mesh size 1200×20 , 1400×24 , and 1600×24 respectively.	110
7.7	Visualization of ligand transport in the capillary at the condition of 4°C and inlet velocity $u = 0.0000866$ m/s, (a) at $t = 5$ minutes, (b) at $t = 10$ minutes, (c) at $t = 20$ minutes, (d) at $t = 40$ minutes, and (e) at $t = 60$ minutes.	114
7.8	The dependency of species concentration at capillary wall on axial axis (x) at $t = 5$ minutes, (a) ligand $[L]/[L_0]$, (b) FGFR, (c) HSPG, (d) FGF-2-FGFR complex, (e) FGF-2-FGFR dimer, (f) FGF-2-FGFR-HSPG complex and its dimer, (g) FGF-2-HSPG complex and its dimer, (h) summation of $[P] + [G] + [T] + 2[G_2] + 2[T_2]$, and (i) summation of $[R] + [C] + [T] + 2[C_2] + 2[T_2]$	115
7.9	The dependency of species concentration at capillary wall on axial axis (x) at $t = 10$ minutes, (a) ligand $[L]/[L_0]$, (b) FGFR, (c) HSPG, (d) FGF-2-FGFR complex, (e) FGF-2-FGFR dimer, (f) FGF-2-FGFR-HSPG complex and its dimer, (g) FGF-2-HSPG complex and its dimer, (h) summation of $[P] + [G] + [T] + 2[G_2] + 2[T_2]$, and (i) summation of $[R] + [C] + [T] + 2[C_2] + 2[T_2]$	116
7.10	The dependency of species concentration at capillary wall on axial axis (x) at $t = 20$ minutes, (a) ligand $[L]/[L_0]$, (b) FGFR, (c) HSPG, (d) FGF-2-FGFR complex, (e) FGF-2-FGFR dimer, (f) FGF-2-FGFR-HSPG complex and its dimer, (g) FGF-2-HSPG complex and its dimer, (h) summation of $[P] + [G] + [T] + 2[G_2] + 2[T_2]$, and (i) summation of $[R] + [C] + [T] + 2[C_2] + 2[T_2]$	117
7.11	The dependency of species concentration at capillary wall on axial axis (x) at $t = 40$ minutes, (a) ligand $[L]/[L_0]$, (b) FGFR, (c) HSPG, (d) FGF-2-FGFR complex, (e) FGF-2-FGFR dimer, (f) FGF-2-FGFR-HSPG complex and its dimer, (g) FGF-2-HSPG complex and its dimer, (h) summation of $[P] + [G] + [T] + 2[G_2] + 2[T_2]$, and (i) summation of $[R] + [C] + [T] + 2[C_2] + 2[T_2]$	118
7.12	The dependency of species concentration at capillary wall on axial axis (x) at $t = 60$ minutes, (a) ligand $[L]/[L_0]$, (b) FGFR, (c) HSPG, (d) FGF-2-FGFR complex, (e) FGF-2-FGFR dimer, (f) FGF-2-FGFR-HSPG complex and its dimer, (g) FGF-2-HSPG complex and its dimer, (h) summation of $[P] + [G] + [T] + 2[G_2] + 2[T_2]$, and (i) summation of $[R] + [C] + [T] + 2[C_2] + 2[T_2]$	119
7.13	Visualization of ligand transport in the capillary at the condition of 37°C and inlet velocity $u = 0.0000866$ m/s, (a) at $t = 5$ minutes, (b) at $t = 10$ minutes, (c) at $t = 20$ minutes, (d) at $t = 40$ minutes, and (e) at $t = 60$ minutes.	120

7.14	The effect of internalization on species distribution at $t = 5$ minutes, (a) ligand $[L]/[L_0]$, (b) FGFR, (c) HSPG, (d) FGF-2-FGFR complex, (e) FGF-2-FGFR dimer, (f) FGF-2-FGFR-HSPG complex, (g) FGF-2-FGFR-HSPG dimer, (h) FGF-2-HSPG complex, (i) FGF-2-HSPG dimer, (j) $[P]+[G]+[T]+2[G_2]+2[T_2]$, and (k) $[R]+[C]+[T]+2[C_2]+2[T_2]$.	122
7.15	The effect of internalization on species distribution at $t = 10$ minutes, (a) ligand $[L]/[L_0]$, (b) FGFR, (c) HSPG, (d) FGF-2-FGFR complex, (e) FGF-2-FGFR dimer, (f) FGF-2-FGFR-HSPG complex, (g) FGF-2-FGFR-HSPG dimer, (h) FGF-2-HSPG complex, (i) FGF-2-HSPG dimer, (j) $[P]+[G]+[T]+2[G_2]+2[T_2]$ and (k) $[R]+[C]+[T]+2[C_2]+2[T_2]$.	123
7.16	The effect of internalization on species distribution at $t = 20$ minutes, (a) ligand $[L]/[L_0]$, (b) FGFR, (c) HSPG, (d) FGF-2-FGFR complex, (e) FGF-2-FGFR dimer, (f) FGF-2-FGFR-HSPG complex, (g) FGF-2-FGFR-HSPG dimer, (h) FGF-2-HSPG complex, (i) FGF-2-HSPG dimer, (j) $[P]+[G]+[T]+2[G_2]+2[T_2]$, and (k) $[R]+[C]+[T]+2[C_2]+2[T_2]$.	124
7.17	The effect of internalization on species distribution at $t = 40$ minutes, (a) ligand $[L]/[L_0]$, (b) FGFR, (c) HSPG, (d) FGF-2-FGFR complex, (e) FGF-2-FGFR dimer, (f) FGF-2-FGFR-HSPG complex, (g) FGF-2-FGFR-HSPG dimer, (h) FGF-2-HSPG complex, (i) FGF-2-HSPG dimer, (j) $[P]+[G]+[T]+2[G_2]+2[T_2]$, and (k) $[R]+[C]+[T]+2[C_2]+2[T_2]$.	125
7.18	The effect of internalization on species distribution at $t = 60$ minutes, (a) ligand $[L]/[L_0]$, (b) FGFR, (c) HSPG, (d) FGF-2-FGFR complex, (e) FGF-2-FGFR dimer, (f) FGF-2-FGFR-HSPG complex, (g) FGF-2-FGFR-HSPG dimer, (h) FGF-2-HSPG complex, (i) FGF-2-HSPG dimer, (j) $[P]+[G]+[T]+2[G_2]+2[T_2]$, and (k) $[R]+[C]+[T]+2[C_2]+2[T_2]$.	126
7.19	Visualization of ligand transport in the capillary at the condition of 37°C and inlet velocity $u = 0.0001732$ m/s, (a) at $t = 5$ minutes, (b) at $t = 10$ minutes, (c) at $t = 20$ minutes, (d) at $t = 40$ minutes, and (e) at $t = 60$ minutes.	127
7.20	Visualization of ligand transport in the capillary at the condition of 37°C and inlet velocity $u = 0.00003464$ m/s, (a) at $t = 5$ minutes, (b) at $t = 10$ minutes, (c) at $t = 20$ minutes, (d) at $t = 40$ minutes, and (e) at $t = 60$ minutes.	128

List of Files

1.1 dissertation.pdf xii

1 Introduction

The purpose of this chapter is to state the motivation of the proposed dissertation research and give an introduction to Computer Aided Design and Engineering in areas of fluid mechanics, heat transfer, chemical reaction, and molecular binding, which are usually described by a set of partial differential equations (PDEs) and/or ordinary differential equations (ODEs). With the development of high-speed digital computers, the modeling and simulation of complex phenomena such as multi-dimensional combustion that couples fluid flow and chemical reaction is made possible in practice. For example, problems that now take a few seconds of CPU time in a modern computer would have taken years to complete with computers available twenty years ago [3]. An interesting phenomenon is that the growth of computer speed and that of computer costs are not at the same rate, and computer speed has increased much more rapidly than computer costs. The direct consequence of this trend is that the cost of performing a given calculation has been reduced substantially. According to an investigation on computation cost, the expense for a given task and algorithm has been reduced by a factor of 10 every 8 years [17].

1.1 Motivation

Traditionally, the research on fluid mechanics and heat transfer depends heavily on experimental and theoretical methods. The advantages of these two approaches are that the experimental approach produces most realistic results and the theoretical approach gives a clean solution in the formula form. However, both of them have some disadvantages. For the experimental method, test equipments are required and expensive in many cases, and the wind tunnel measurement is difficult and expensive in operating. The theoretical approach is usually restricted to some simple geometry and linear problems. The numerical method can overcome many of the drawbacks

mentioned above, such as cutting the cost due to wind tunnel experiments, being applied to complicated nonlinear problems, and obtaining a transient solution, despite the drawbacks of numerical errors, boundary condition specification, and needed computer cost [3]. In some situations, such as studying the heat transfer in human skin, it is not possible to conduct a direct experiment, numerical simulation with physical properties from animals is the only choice.

One of the important topics this dissertation involves is numerical simulation of laminar diffusion flame. Laminar diffusion flame itself is an important flame, and it can also be used as a prototype to simulate more complicated turbulent reacting flows. As it is known, combustion is the oldest technology of mankind, and it has been used for more than one million years and will still be used as the most important technology to provide energy service for the survival and advance of human being. At present, about 90% of our worldwide energy support is provided by combustion [128]. Examples of the application of combustion include automotive industry, aerospace industry, electrical power generation, and heating. Combustion is a very important process which involves fluid flow, chemical reaction, energy transform, and radiation heat transfer. A direct consequence of using fossil fuels is the formation of pollutant during combustion. This can be witnessed by the global climate change, which has attracted considerable attentions and will continue to be a central topic in the future. It is really worthwhile studying this process in terms of importance and complexity.

1.2 Modeling Procedure

The procedures involved in modeling and simulation usually include four steps: set up the mathematical model, rewrite the mathematical model such that it is suitable for computer simulation, develop computer programs, and verify simulation results [109]. In terms of economy, the application of computers often achieves a very low cost per calculation while a relatively high initial cost is required to develop the program. It

should be recognized, however, that once a computer program has been generated, the initial cost for reuse in subsequent projects is usually negligible or marginal.

Our research focuses on the modeling and simulation of physical and biological processes in nature, which are governed by partial differential equations (PDEs). So in our case, the first step in modeling procedure is to derive a set of PDEs or use the existing PDEs as the mathematical model.

A general second-order partial differential equation in standard form in a 2D space can be written as [3]

$$au_{xx} + bu_{xy} + cu_{yy} + du_x + eu_y + fu = g(x, y) \quad (1.1)$$

where a , b , c , d , e , and f are functions of (x, y) . Eq. (1.1) can be classified as hyperbolic, parabolic, and elliptic based on the values of a , b , and c . The PDE is hyperbolic if $b^2 - 4ac > 0$, parabolic if $b^2 - 4ac = 0$, and elliptic if $b^2 - 4ac < 0$. Elliptic PDEs govern boundary value problems, or equilibrium problems, which include steady-state temperature distributions, incompressible inviscid flow, and equilibrium stress distributions in solids. Hyperbolic or parabolic PDEs govern initial value or initial boundary value problems, which are frequently called marching or propagation problems.

In numerical simulation, systems of equations are frequently encountered, which can also be classified as hyperbolic, elliptic, parabolic, or mixed. A system is mixed if the roots of the characteristic equations of the coefficient matrix include both real and complex parts. Detailed information of the classification of systems of equations can be found in [3].

The mathematical model of PDEs is not suitable for direct computer simulation. The PDEs in the continuous problem domain must be discretized so that the dependent variables are considered to exist only at discrete points. Frequently used discretization techniques in numerical simulation include finite difference, finite volume, and finite element methods. Finite difference method has the property of easy

to implement by discretizing the differential equations directly, easy to obtain higher order accuracy by using higher order difference, and the coefficient matrix of the linear system obtained from implicit discretization is easy to solve, but it is difficult to apply to irregularly shaped domains. For both finite volume and finite element methods, the differential equations have to be written in an integral form before discretization. The major advantage of finite element and finite volume methods is their easy application in irregular domains and the use of fully unstructured grids composed of triangles and/or quadrilaterals [10]. It is worth noticing that finite volume method has a unique property of inherent flux conservation, which is the desired feature we want to pursue in numerical simulation of fluid flow and heat transfer. However, both finite volume and finite element methods have the drawback of increased computation cost in implicit discretization due to denser coefficient matrix. The selection of a discretization method depends on actual applications. In the case of simple geometry, finite difference method may be used for simplicity. In the case of complex geometry with irregular boundaries, finite volume or finite element may be applied.

1.3 Solution Methods

Numerical schemes which are employed to convert governing PDEs to discrete algebraic expressions are very important for the solution of equations in terms of accuracy, stability, and efficiency, and are usually problem dependent. Hyperbolic equations can be solved very efficiently using explicit methods, in which only one unknown appears in each equation. High resolution schemes have been developed using explicit discretization and flux limiters [116], such as the second order total variation diminishing TVD scheme [90], second order MUSCL type TVD scheme [122], third order piecewise parabolic method (PPM) [22], Runge-Kutta methods, and higher order weighted essentially non-oscillatory (WENO) scheme [106]. For these explicit schemes, there exists a common shortcoming: they are not unconditionally stable.

The stability of explicit numerical schemes is confined by CFL condition.

For problems governed by elliptic PDEs, such as steady-state heat conduction equation, simultaneous equations have to be solved, which involves inversion of the coefficient matrix. Such matrix is usually sparse, and its detailed structure depends on the dimensions of the problem and the discretization strategy. For parabolic equations, such as transient heat conduction equation, simple explicit method is highly dissipative. The commonly used method is the implicit treatment of the temporal terms, and again, simultaneous algebraic equations have to be solved.

When doing simulations in one space dimension, the coefficient matrix of the discrete algebraic equations is frequently tridiagonal or block tridiagonal. A very efficient numerical algorithm exists for tridiagonal matrices, the Thomas algorithm, which runs in linear time. For multidimensional applications, however, the coefficient matrix is very difficult to invert directly. Due to the very attractive feature of the Thomas algorithm, a multi-dimensional problem is frequently solved with multi-steps such that a tridiagonal matrix is formed for each step. Algorithms related to this technique include alternating-direction-implicit (ADI) method and fractional-step methods. For a two-dimensional heat equation [3],

$$\frac{\partial u}{\partial t} = \alpha \left(\frac{\partial^2 u}{\partial x^2} + \frac{\partial^2 u}{\partial y^2} \right),$$

the ADI method given by Peaceman and Rachford can be written as

$$\frac{u_{i,j}^{n+1/2} - u_{i,j}^n}{\Delta t/2} = \alpha \left(\frac{u_{i+1,j}^{n+1/2} - 2u_{i,j}^{n+1/2} + u_{i-1,j}^{n+1/2}}{(\Delta x)^2} + \frac{u_{i,j+1}^n - 2u_{i,j}^n + u_{i,j-1}^n}{(\Delta y)^2} \right)$$

and

$$\frac{u_{i,j}^{n+1} - u_{i,j}^{n+1/2}}{\Delta t/2} = \alpha \left(\frac{u_{i+1,j}^{n+1/2} - 2u_{i,j}^{n+1/2} + u_{i-1,j}^{n+1/2}}{(\Delta x)^2} + \frac{u_{i,j+1}^{n+1} - 2u_{i,j}^{n+1} + u_{i,j-1}^{n+1}}{(\Delta y)^2} \right),$$

and the splitting of the fractional-step gives the following expression

$$\frac{u_{i,j}^{n+1/2} - u_{i,j}^n}{\Delta t/2} = \alpha \left(\frac{u_{i+1,j}^{n+1/2} - 2u_{i,j}^{n+1/2} + u_{i-1,j}^{n+1/2}}{(\Delta x)^2} \right)$$

and

$$\frac{u_{i,j}^{n+1} - u_{i,j}^{n+1/2}}{\Delta t/2} = \alpha \left(\frac{u_{i,j+1}^{n+1} - 2u_{i,j}^{n+1} + u_{i,j-1}^{n+1}}{(\Delta y)^2} \right).$$

The splitting techniques of ADI and fractional-step do not work well in situations that are highly nonlinear, such as the strongly coupled chemical reacting flow. As reported by Xu [132], difficulties had been encountered in obtaining a converged solution of the pressure and pressure correction equations when using the splitting method for simulating two-dimensional laminar diffusion flame. Instead, the iteration converged smoothly when a direct sparse matrix solver was employed. Current work focuses on the application of newly developed Krylov subspace iterative method to the simulation of various physical and biological phenomena that are modeled by PDEs.

2 Iterative Methods and Effective Preconditioners

The purpose of this chapter is to give a literature review of methods solving linear system of equations, including direct methods, stationary iterative methods, Krylov subspace based iterative method, multigrid method, and finally efficient preconditioners.

2.1 Direct Methods

Gaussian Elimination is the basic method for solving linear system of algebraic equations $Ax = b$, where A is a square matrix and has the following form:

$$A = \begin{bmatrix} a_{11} & a_{12} & \cdots & a_{1n} \\ a_{21} & a_{22} & \cdots & a_{2n} \\ \cdots & \cdots & \cdots & \cdots \\ a_{n1} & a_{n2} & \cdots & a_{nn} \end{bmatrix}.$$

The algorithm of Gaussian elimination consists of two steps, forward elimination and back substitution. After forward elimination, the upper triangular system of equations

$$A'x = b'$$

is obtained, which can easily be solved, where

$$A' = \begin{bmatrix} a'_{11} & a'_{12} & \cdots & a'_{1n} \\ 0 & a'_{22} & \cdots & a'_{2n} \\ \cdots & \cdots & \cdots & \cdots \\ 0 & 0 & \cdots & a'_{nn} \end{bmatrix}.$$

For a linear system of n equations, the number of arithmetic operations required by Gaussian elimination is in the order of $O(n^3)$, due to the forward elimination step.

LU Factorization is a variant of Gaussian elimination. The original matrix A can be factorized into the product of two matrices $A = LU$, where L is a lower triangular matrix, and U is an upper triangular matrix. The LU factorization can easily be constructed from modifying Gaussian elimination with the upper triangular matrix U being the one produced by the forward step of Gaussian elimination and

the elements of the lower triangular matrix L being the multiplicative factors (a_{ji}/a_{ii}) used in the elimination process [35]. The computational cost of the LU factorization is equivalent to that of Gaussian elimination. The LU factorization has the advantage over Gaussian elimination in that the inverse of the lower triangular matrix L is still lower triangular and the factorization can be done without knowing the vector b . This is useful when a series of linear systems with the same coefficient matrix but multiple right-hand side vectors have to be solved.

Tridiagonal Matrix Algorithm and Cyclic Reduction are efficient methods for solving tridiagonal systems. Tridiagonal Matrix Algorithm (TDMA) or Thomas algorithm is a special case of Gaussian elimination, in which only one element needs to be eliminated from each row during the forward elimination step. Both the forward elimination and back-substitution steps run in linear time, proportional to n , provided pivoting is not needed.

The cyclic reduction method is for a specialized tridiagonal system, in which all of the elements on each diagonal are identical. This method recursively reduce the size of the linear system by a half on each recursive call, until only one equation is left. The last equation is solved directly, and the values of the remaining variables can then be obtained by a variant of back substitution. Assume the number of unknowns are a power of two, the cost of this method is proportional to $\log_2 n$.

2.2 Stationary Iterative Methods

There are ways to convert

$$Ax = b$$

to a linear fixed-point iteration. Methods such as Jacobi, Gauss-Seidel, and successive overrelaxation (SOR) iteration are based on splitting of A into the form [55]

$$A = A_1 + A_2$$

where A_1 is a nonsingular matrix constructed so that equations with A_1 as the coefficient matrix are easy to solve. Then $Ax = b$ is converted to the fixed point problem

$$x = A_1^{-1}(b - A_2x).$$

Jacobian Iteration The Jacobi iteration uses the splitting in the following way

$$A_1 = D,$$

and

$$A_2 = L + U,$$

where D is the diagonal of A and L and U are the lower and upper triangular parts. This leads to the iteration matrix

$$M_{Jacb} = -D^{-1}(L + U).$$

Let $(x_k)_i$ denote the i th component of the k th iterate we can express Jacobi iteration concretely as

$$(x_{k+1})_i = a_{ii}^{-1} (b_i - \sum_{j \neq i} a_{ij}(x_k)_j).$$

Note that A_1 is diagonal and hence trivial to invert.

Gauss-Seidel iteration Gauss-Seidel iteration overwrites the approximate solution with the new value as soon as it is computed. This results in the iteration

$$(x_{k+1})_i = a_{ii}^{-1} (b_i - \sum_{j < i} a_{ij}(x_{k+1})_j - \sum_{j > i} a_{ij}(x_k)_j),$$

the splitting is

$$A_1 = D + L, A_2 = U,$$

and the iteration matrix

$$M_{GS} = -(D + L)^{-1}U,$$

Note that A_1 is lower triangular, and hence $A_1^{-1}y$ is easy to compute for vector y . Note also that, unlike Jacobi iteration, the Gauss-Seidel iteration depends on the

ordering of the unknowns. Backward Gauss-Seidel begins the update of x with the n th coordinate rather than the first, resulting in the splitting

$$A_1 = D + U, A_2 = L,$$

and iteration matrix

$$M_{BGS} = -(D + U)^{-1}L.$$

A symmetric Gauss-Seidel iteration is a forward Gauss-Seidel iteration followed by a backward Gauss-Seidel iteration. This leads to the iteration matrix

$$M_{SGS} = M_{BGS}M_{GS} = (D + U)^{-1}L(D + L)^{-1}U.$$

If A is symmetric then $U = L^T$. In that event

$$M_{SGS} = (D + U)^{-1}L(D + L)^{-1}U = (D + L^T)^{-1}L(D + L)^{-1}L^T.$$

From the point of view of preconditioning, one wants to write the stationary method as a preconditioned Richardson iteration. That means that one wants to find B such that $M = I - BA$ and then use B as an approximate inverse. For the Jacobi iteration,

$$B_{Jac} = D^{-1}.$$

For symmetric Gauss-Seidel

$$B_{SGS} = (D + L^T)^{-1}D(D + L)^{-1}.$$

Successive Overrelaxation (SOR) The successive overrelaxation iteration modifies Gauss-Seidel by adding a relaxation parameter ω to construct an iteration with the iteration matrix

$$M_{SOR} = (D + \omega L)^{-1}((1 - \omega)D - \omega U).$$

The performance can be dramatically improved with a good choice of ω , but still not competitive with the Krylov methods. A further disadvantage of SOR is that the choice of ω is often difficult to make.

Symmetric Successive Overrelaxation (SSOR) If the coefficient matrix A is symmetric, the SSOR method can produce an iteration matrix similar to a symmetric matrix. SSOR include a forward SOR sweep and a backward SOR sweep. This method is usually used as a preconditioner to other iterative methods for symmetric matrices. The iteration matrix of SSOR is

$$M_{SSOR} = (D + \omega U)^{-1}((1 - \omega)D - \omega L)(D + \omega L)^{-1}((1 - \omega)D - \omega U).$$

Incomplete LU Decomposition: Stone's Method The LU factorization can be written as $M = LU = A + N$, where L and U are both sparse matrices and the magnitude of the elements in N is small [35]. The incomplete LU factorization (ILU) is a LU factorization such that for every zero element of the original matrix A , the corresponding element of L or U is set to zero. This is not an exact factorization of A , the product of the two factors L and U , however, can be used as the preconditioning matrix of an iterative method. Using Laplace's equation as an example, the discretization of the two-dimensional one on a five point stencil may be written in algebraic format as

$$A_P x_P^n + A_S x_S^n + A_W x_W^n + A_N x_N^n + A_E x_E^n = b_P.$$

The resulting coefficient matrix A is five-diagonal. The product of the lower and upper triangular matrices L and U generated by the standard ILU factorization of A , M is seven-diagonal, which has two more non-zero diagonals, corresponding to nodes NW and SE or NE and SW, depending on the ordering of the nodes in the vector. To make the factorization unique, every element on the main diagonal of U is set to unity. Let us consider the following vector

$$(Mx)_P = M_P x_P + M_S x_S + M_N x_N + M_E x_E + M_W x_W + M_{NW} x_{NW} + M_{SE} x_{SE}.$$

Each term in the equation corresponds to a diagonal of $M = LU$. Since $N = M - A$, the matrix N must contain diagonals NW and SE, and the following condition has

to be satisfied

$$N_P x_P + N_N x_N + N_S x_S + N_E x_E + N_W x_W + M_{NW} x_{NW} + M_{SE} x_{SE} \approx 0$$

Stone [114] proposed to use the following approximations,

$$x_{NW} \approx \alpha(x_W + x_N - x_P)$$

and

$$x_{SE} \approx \alpha(x_S + x_E - x_P),$$

where the stability requirement is $\alpha < 1$.

The LU factorization due to Stone's suggestion can be expressed as [35]:

Algorithm 1 Stone-ILU(A, L, U)

- 1: $L_W = A_W / (1 + \alpha U_N)$
 - 2: $L_S = A_S / (1 + \alpha U_E)$
 - 3: $L_P = A_P + \alpha(L_W U_N + L_S U_E) - L_W U_E - L_S U_N$
 - 4: $U_N = (A_N - \alpha L_W U_N) / L_P$
 - 5: $U_E = (A_E - \alpha L_S U_E) / L_P$
-

The algorithm solving the linear system $Ax = b$ using Stone's ILU method is listed in Algorithm 2, where ϵ is the convergence criteria, r the residual, k_{max} the maximum number of iterations, and δ the correction.

Algorithm 2 Stone(A, b, ϵ, L, U)

- 1: Initialization: $r = b - Ax, k = 1$
 - 2: **while** $\|r\|_2 > \epsilon \|InitialResidual\|_2$ and $k < k_{max}$ **do**
 - 3: $Y = (r - L_S Y - L_W Y) / L_P$
 - 4: $\delta = Y - U_N \delta - U_E \delta$
 - 5: $x = x + \delta$
 - 6: $k = k + 1$
 - 7: **end while**
-

2.3 Krylov Subspace Based Iterative Methods

Conjugate Gradient (CG) method is intended to solve a symmetric positive definite (SPD) matrix. Recall that a matrix A is symmetric if $A = A^T$ and positive

definite if its eigenvalues are all positive, i.e., $x^T Ax > 0$ for all $x \neq 0$. For a positive definite matrix, solving the system of equations $Ax = b$ is equivalent to finding the minimum of [35]

$$\phi(x) = \frac{1}{2}x^T Ax - x^T b = \frac{1}{2} \sum_{j=1}^n \sum_{i=1}^n a_{ij} x_i x_j - \sum_{i=1}^n x_i b_i$$

with respect to all the x_i . Note that if $\phi(x)$ is the minimal value in R^n then

$$\nabla \phi(\tilde{x}) = A\tilde{x} - b = 0,$$

and hence $\tilde{x} = x$. The conjugate gradient method is based on a remarkable discovery that it is possible to minimize a function with respect to several directions simultaneously while searching in one direction at a time. This is made possible by a clever choice of the directions. Using two directions as an example, letting x minimize ϕ in the plane of $p^1 - p^2$, we can write x as $x = x^0 + \alpha^1 p^1 + \alpha^2 p^2$. This problem can be reduced to the problem of minimizing with respect to p^1 and p^2 individually if the two directions are conjugate. That is $p^1 \dot{A} p^2 = 0$.

The rate of convergence of CG depends on the condition number $\kappa(A)$ with

$$\kappa(A) = \frac{\lambda_{max}}{\lambda_{min}},$$

where λ_{max} and λ_{min} are the largest and smallest eigenvalues of the matrix A . In numerical simulation of heat transfer and fluid flow, the condition numbers of resulting matrices are approximately the square of the maximum number of grid points in any direction [55]. To reduce the condition number and improve the performance of the iteration, the initial system $Ax = b$ can be replaced by another SPD system with the same solution. The new system may be written as $MAx = Mb$, and M is a nonsingular matrix. Since this may destroy the symmetry of matrix A , the preconditioner may take the following form:

$$C^{-1}AC^{-1}y = C^{-1}b,$$

where the conjugate gradient method is applied to the matrix $C^{-1}AC^{-1}$, and the unknown vector x can be found as $x = C^{-1}y$. One of the preconditioned CG algorithms is presented in Algorithm 3 [55]. In Algorithm 3, only five vectors need to

Algorithm 3 PCG($x, b, A, M, \epsilon, kmax$)

```

1: Initialization:  $r = b - Ax, \rho_0 = \|r\|_2^2, k = 1$ 
2: while  $\sqrt{\rho_{k-1}} > \epsilon\|b\|_2$  and  $k < kmax$  do
3:    $Mz = r$ 
4:    $s_{k-1} = z^T r$ 
5:   if  $k = 1$  then  $\beta = 0$  and  $p = z$  else  $\beta = s_{k-1}/s_{k-2}, p = z\beta p$ 
6:    $w = Ap$ 
7:    $\alpha = s_{k-1}/p^T w$ 
8:    $x = x + \alpha p$ 
9:    $r = r - \alpha w$ 
10:   $\rho_k = r^T r$ 
11:   $k = k + 1$ 
12: end while

```

be stored, $x, w, p, r,$ and z . This algorithm involves solving linear system $Mz = r$, where $M = C^{-1}$ and C is the preconditioning matrix. In the algorithm, $C^{-1}A$ is in fact never actually constructed [35]. It is required that M must be easy to invert, and is often chosen as the incomplete Cholesky factorization of A .

Bi-Conjugate Gradient Stabilized (BiCGSTAB) method was proposed by van der Vorst [123] with the purpose of extending the CG algorithm to non-symmetric matrices. The BiCGSTAB algorithm is summarized in [55]. In Algorithm 4, seven vectors need to be stored, $x, b, r, \hat{r}_0, p, v,$ and t . Four matrix-vector products are required in each iteration of the algorithm. The cost in storage and in floating point operations per iteration remains bounded for the entire iteration.

General Minimum Residual (GMRES) method is a projection method that minimizes the residual norm over all vectors in $x_0 + \mathcal{K}_k$, where x_0 is the initial value and \mathcal{K}_k is the k -th Krylov subspace with $v_1 = r_0/\|r_0\|_2$ [94]. The k -th Krylov subspace is

$$\mathcal{K}_k(A, r_0) = \text{span}(r_0, Ar_0, \dots, A^{k-1}r_0)$$

Algorithm 4 BiCGSTAB($x, b, A, \epsilon, kmax$)

```
1: Initialization:  $r = b - Ax$ ,  $\hat{r}_0 = r$ ,  $\rho_0 = \alpha = w_0 = 1$ ,  $v = p = 0$ ,  $k = 0$ ,  $\rho_1 = \hat{r}_0^T r$ 
2: while  $\|r\|_2 > \epsilon \|b\|_2$  and  $k < kmax$  do
3:    $k = k + 1$ 
4:    $\beta = (\rho_k / \rho_{k-1})(\alpha / w)$ 
5:    $p = r + \beta(p - wv)$ 
6:    $v = Ap$ 
7:    $\alpha = \rho_k / (\hat{r}_0^T v)$ 
8:    $s = r - \alpha v$  and  $t = As$ 
9:    $w = t^T s / \|t\|_2^2$  and  $\rho_{k+1} = -w \hat{r}_0^T t$ 
10:   $x = x + \alpha p + ws$ 
11:   $r = s - wt$ 
12: end while
```

where $r_0 = b - Ax_0$. This method seeks an approximate solution x_k from the affine subspace $x_0 + \mathcal{K}_k$ of dimension k by imposing the Galerkin condition

$$b - Ax_m \perp \mathcal{K}_k.$$

The k th GMRES iteration is equivalent to the least squares problem

$$\text{minimize}_{x \in x_0 + \mathcal{K}_k} \|b - Ax\|_2.$$

One implementation of GMRES with the Householder orthogonalization can be written as pseudocode in Algorithm 5 [55].

2.4 Multigrid Methods

The rate of convergence of an iterative method depends on the eigenvalues of the iteration matrix. The ratio of the largest and smallest eigenvalues determines how rapidly the solution is reached. The eigenvector associated with this eigenvalue determines the spatial distribution of the convergence error. The largest eigenvalues, however, are determined by the type of equations as well as the method used to solve the equations. Using Laplace's equation as an example, the Jacobian method has two largest eigenvalues that are real and of opposite sign, one representing a smooth function and the other a rapidly oscillating function. The convergence of Jacobian

Algorithm 5 GMRES($x, b, A, \epsilon, kmax$)

- 1: Initialization: $r = b - Ax$, $v_1 = r/\|r\|_2$, $\rho = \|r\|_2$, $\beta = \rho$, $k = 0$, $g = \rho(1, 0, \dots, 0)^T \in R^{kmax+1}$
 - 2: **while** $\rho > \epsilon\|b\|_2$ and $k < kmax$ **do**
 - 3: $k = k + 1$
 - 4: $v_{k+1} = Av_k$
 - 5: **for** $j = 1, \dots, k$ **do**
 - 6: $h_{jk} = v_{k+1}^T v_j$
 - 7: $v_{k+1} = v_{k+1} - H_{jk}V_j$
 - 8: **end for**
 - 9: $h_{k+1,k} = \|v_{k+1}\|_2$
 - 10: Test for loss of orthogonality and reorthogonalize if necessary.
 - 11: $v_{k+1} = v_{k+1}/\|v_{k+1}\|_2$
 - 12: **if** $k > 1$ apply Q_{k-1} to the k th column of H **then**
 - 13: $\nu = \sqrt{h_{k,k}^2 + h_{k+1,k}^2}$
 - 14: $c_k = h_{k,k}/\nu$, $s_k = -h_{k+1,k}/\nu$, $h_{k,k} = c_k h_{k,k} - s_k h_{k+1,k}$, and $h_{k+1,k} = 0$
 - 15: $g = G_k(c_k, s_k)g$
 - 16: **end if**
 - 17: **end while**
 - 18: $\rho = |(g)_{k+1}|$
 - 19: set $r_{i,j} = h_{i,j}$ for $1 \leq i, j \leq k$
 - 20: set $(w)_i = (g)_i$, for $1 \leq i \leq k$
 - 21: solve the upper triangular system $Ry^k = w$
 - 22: $x_k = x_0 + V_k y^k$
-

method is slow since the convergence error for the Jacobian method is a mixture of very smooth and very rough components. The Gauss-Seidel method has a single largest eigenvalue that is real and positive with an eigenvector that makes the convergence error a smooth function of the spatial coordinates. The SOR method has a number of largest eigenvalues with optimum over-relaxation factor lie on a circle in the complex plane, so the convergence error is very complicated [35].

If the error is smooth, the update can be computed on a coarser grid to save computational cost. For example, on a grid twice as coarse as the original one in two dimensions, the cost needed for iterations is only 1/4 that of the original grid. Furthermore, iterative methods converge much faster on coarser grids. So the total time can be saved substantially by using coarse grids. In order to do this, two basic steps have to be performed: smoothing the residual from the fine grid to the coarse one and interpolating the correction from the coarse grid to the fine one. Linear interpolation is the simplest interpolation from coarse to fine grids.

The most important property of the multigrid method is that the number of iterations on the finest grid required to reach a given level of convergence is roughly independent of the number of grid nodes. The iterative method on which the multigrid method is based must be a good smoother. Gauss-Seidel, incomplete LU decomposition, and conjugate gradient method preconditioned with incomplete Cholesky can be used as such smoothers.

A two-level multigrid method may include the following steps [35]:

2.5 Preconditioners

A preconditioner to a given linear system can be any form of explicit or implicit modifications of the original system that makes it “easier” to solve by an iterative method [94]. For the original system $Ax = b$, a preconditioned system $M^{-1}Ax = M^{-1}b$ can be formed, where the preconditioning matrix M^{-1} should be inexpensive

Algorithm 6 Multi-grid(x, b, A, ϵ)

- 1: Initialization: $r = b - Ax$ for $x_0 = 0$
 - 2: **while** $r > \epsilon$ **do**
 - 3: Solve $Ax = b$ on the fine grid using initial guess $x_0 = x_0$
 - 4: Calculate the residual $r = b - Ax_0$
 - 5: reduce A and r to a coarser grid
 - 6: Solve the correction equation $Ae = r$ iteratively on the coarse grid
 - 7: Interpolate the correction on the fine grid
 - 8: Update the solution on the fine grid $x_0 = x_0 + e$
 - 9: **end while**
-

to apply to a matrix-vector product. The construction of M^{-1} can be performed in different ways depending on applications.

Jacobi, GS, SOR, and SSOR Preconditioners A fixed-point iteration for the linear system $Ax = b$ has the form $x_{k+1} = M^{-1}Nx_k + M^{-1}b = Gx_k + f$ [94], where M and N are the splitting of A , $A = M - N$, $f = M^{-1}b$, and $G = M^{-1}N = I - M^{-1}A$. For Jacobian iteration, the preconditioning matrix is simply $M = D$, where D is the diagonal of A . For Gauss-Seidel iteration, the preconditioning matrix is $M = (D + E)$ for forward sweep and $M = D + F$ for backward sweep, where E and F are the strict lower part and upper part of A respectively. For successive over relaxation method, the preconditioning matrix is in the form of $M = (D + \omega E)$ or $M = (D + \omega F)$. The preconditioner matrices for the symmetric Gauss-Seidel iteration (SGS) and the symmetric SOR (SSOR) can be written as $M = (D + E)D^{-1}(D + F)$ and $M = (D + \omega E)D^{-1}(D + \omega F)$ respectively. It can be seen that the SGS and SSOR preconditioning matrix is of the form $M = LU$, where L and U have the same pattern as the L -part and U -part of A .

ILU(0) Preconditioner is the incomplete LU factorization of A with no fill-in, i.e., the zero pattern of matrix $M = LU$ is precisely the same as that of matrix A . As described before, for a 2D Laplace's equation, the coefficient matrix A is five-diagonal, but the matrix M is seven-diagonal. The entries in these extra diagonals are called fill-in elements. The ILU(0) factorization can be stated as: any pairs of matrices L

(unit lower triangular) and U (upper triangular) such that the elements of $A - LU$ are zero in locations where the elements of A are not zero. For any arbitrary matrix A , let $NZ(A)$ denote any nonzero elements in A , i.e., the set of pairs (i, j) such that $a_{i,j} \neq 0$, where $1 \leq i, j \leq n$, the algorithm of ILU(0) factorization can be written as [94]:

Algorithm 7 ILU(0)

```

1: for  $i = 2, \dots, n$  do
2:   for  $k = 1, \dots, i - 1$  do
3:     if  $(ik) \in NZ(A)$  then
4:       Compute  $a_{ik} = a_{ik}/a_{kk}$ 
5:       for  $j = k + 1, \dots, n$  do
6:         if  $(ij) \in NZ(A)$  then
7:           Compute  $a_{ij} = a_{ij} - a_{ik}a_{kj}$ 
8:         end if
9:       end for
10:    end if
11:  end for
12: end for

```

ILU(k) Preconditioner allows some fill-ins to increase the accuracy and improve the rate of convergence, where k is the level of fill. The product of L and U obtained from standard ILU factorization contains two extra diagonals. Assume that the original matrix A have the same pattern as M , where $M = LU$, with zero in the fill-in positions, the factors of L_1 and U_1 from ILU(1) factorization can be obtained by performing an ILU(0) factorization on the pretended matrix. The product of L_1 and U_1 has two additional diagonals in the lower and upper parts.

In ILU(k), all fill-in elements with level of fill less than k are kept. The higher the level, the smaller the elements. The initial level of fill of an element a_{ij} of a sparse matrix A is defined by $lev_{ij} = 0$ if $a_{ij} \neq 0$ or $i = j$, and $lev_{ij} = \infty$ otherwise. During the construction, the level of fill is updated by $lev_{ij} = \min(lev_{ij}, lev_{ik} + lev_{kj} + 1)$. Let a_{i*} indicates the i th row of A , The algorithm for ILU(k) factorization can be written as follows [94].

Algorithm 8 ILU(k)

```
1: Initialization
2: for  $a_{ij} \neq 0$  do
3:    $lev(a_{ij}) = 0$ 
4: end for
5: for  $i = 2, \dots, n$  do
6:   for  $k = 1, \dots, i - 1$  do
7:     if  $lev(a_{ik}) \leq k$  then
8:       Compute  $a_{ik} = a_{ik}/a_{kk}$ 
9:       Compute  $a_{i*} = a_{i*} - a_{ik}a_{k*}$ 
10:       $lev_{ij} = \min(lev_{ij}, lev_{ik} + lev_{kj} + 1)$ 
11:     end if
12:   end for
13:   for each  $a_{ij}$  in row  $i$  do
14:     if  $lev(a_{ij}) > k$  then
15:        $a_{ij} = 0$ 
16:     end if
17:   end for
18: end for
```

ILUT Preconditioner has two dropping parameters p and τ , where p is the parameter that helps control memory usage, while τ is used to reduce computational cost. There are two dropping steps in the ILUT algorithm. The first step is to drop any element w_k such that $w_k < \tau_i$, where w is a full length working row and w_k is the k -th entry of this row, τ_i is relative tolerance obtained by multiplying τ by the 2-norm of the i -th row. The second step is to drop again any element in the row that is less than the relative tolerance τ_i , and then keep only the p largest elements in the L part and p largest elements in the U part of the row in addition to the diagonal element. An algorithm of ILUT factorization can be written as [94]

Algorithm 9 ILUT

```
1: Initialization
2: for  $i = 1, \dots, n$  do
3:    $w = a_{i*}$ 
4:   for  $k = 1, \dots, i - 1$  do
5:     if  $w_k \neq 0$  then
6:        $w_k = w_k / a_{kk}$ 
7:       if  $w_k < \tau \|w\|_2$  then
8:          $w_k = 0$ 
9:       end if
10:      if  $w_k \neq 0$  then
11:         $w = w - w_k u_{k*}$ 
12:      end if
13:    end if
14:  end for
15:  for each element in row  $i$  do
16:    Apply dropping rule to that element
17:    Keep  $p$  largest elements in the  $L$  and  $U$  parts
18:  end for
19:  for  $j = 1, \dots, i - 1$  do
20:     $l_{ij} = w_j$ 
21:  end for
22:  for  $j = i, \dots, n$  do
23:     $u_{ij} = w_j$ 
24:  end for
25:   $w = 0$ 
26: end for
```

3 Bioheat Transfer and Biomechanics in Soft Tissue

3.1 Introduction

Diagnosis, surgery, and prosthesis are common medical procedures visible to us, but the biomechanics associated with them may not be as well known to us as they should be [101]. It would be much better if we could understand the mechanics in living tissues before a medical procedure is applied, as we can do in engineering area by solving constitutive equations. One of the major difficulties in biomechanics is to determine the mechanical properties of materials and tissues under investigation [41]. Therefore, numerical modeling plays an important role in biomechanics by either solving existing or assisting in determining unknown constitutive equations [101].

Heat transfer is a very fundamental and important process in living things, especially in human bodies, in order to maintain an almost constant temperature. In fact, interesting results related to bioheat transfer have been obtained in the past several decades, such as Pennes bioheat transfer equation [85] and other microstructure bioheat transfer models [129, 50, 18].

The modeling of heat related phenomena such as bioheat transfer and heat-induced stress is useful for the development of biological and biomedical technologies, such as thermotherapy and design of heating or cooling garments. A recent trend in bioheat transfer is the application of heat therapy on tumors due to the fact that heat helps the body treat cancers. Such examples of heat therapy are, to just list a few, the development of a model-predictive controller (MPC) of the thermal dose in hyperthermia cancer treatments [6], the use of mammary gland tumor for determining the performance parameters of a microwave radiometer [61], the reduction of large-scale, nonlinear ordinary differential equations due to nonlinear models of electromagnetic phased-array hyperthermia [58], three-dimensional finite-element analyses for radio-frequency hepatic tumor ablation [121], and so on. However, there is little study on

the thermal mechanical interaction at high temperature even though it is related to the thermal damage of tissue such as skin wrinkle and tissue shrinkage [101].

In this work, a thermomechanical model is proposed to investigate the thermomechanical interaction of biological bodies subjected to high temperature. The objective of this research is to obtain some quantitative descriptions of the thermomechanical behavior of soft tissue according to the relationship between heat transfer and heat-induced stress, and eventually to apply this useful information in diagnosis, surgery, prosthesis, and other medical interventions. Since the mechanical behavior may be coupled with electrical and biochemical processes, the analysis related to tissue is much more difficult than traditional structural mechanics. As a rudimentary step of the research, some assumptions are made to simplify the analysis [101]:

- (1) Only mechanical response is considered, electrical and biochemical responses are not included.
- (2) The tissue is isotropic, and the thermal and mechanical responses can be uniformly defined.
- (3) Possible mass transfer such as transport of moisture is ignored.

A three-dimensional numerical model is developed to predict the time dependent temperature distribution in biological tissues and the related deformation. In this work, a 19 point finite difference scheme is employed to discretize the displacement equation, while the heat equation is discretized using a 7 point central difference scheme based on the proposed model. We use an iterative method to solve the resultant linear systems. Simulation results are obtained which demonstrate the thermo-mechanical interactions of soft tissue.

3.2 Constitutive Equations

3.2.1 Heat transfer process

The heat transfer in soft tissue during the thermal exposure to high temperature can be described using Pennes bioheat equation, which is based on the classical Fourier law of heat conduction [85]. The Pennes model is used to address the heat transfer in living tissues. The model is based on the assumption of the energy exchange between the blood vessels and the surrounding tissues. Even though there may exist some differences in describing bioheat transfer in regimes, where vascular countercurrent heat exchange can possibly skew heat flux and temperature information, Pennes model may provide suitable temperature distributions in whole body, organ, and tumor analysis under study [30]. According to Pennes model, the total energy exchange by the flowing blood is proportional to the volumetric heat flow and the temperature difference between the blood and the tissue. The three dimensional expression of Pennes bioheat equation in a media with uniform material properties is given by [101]

$$\rho C \frac{\partial T}{\partial t} = k \frac{\partial^2 T}{\partial x^2} + k \frac{\partial^2 T}{\partial y^2} + k \frac{\partial^2 T}{\partial z^2} + w_b C_b (T_a - T) + Q_m + Q_r(x, y, z, t), \quad (3.1)$$

where T is temperature $^{\circ}C$, ρ the tissue density kg/m^3 , C the tissue specific heat $\text{J}/(\text{kg}^{\circ}C)$, k the tissue thermal conductivity $\text{W}/(\text{m}^{\circ}C)$, w_b the blood perfusion rate $\text{kg}/(\text{m}^3\text{s})$, C_b the blood specific heat, T_a the arterial temperature, Q_m the metabolic heat generation rate W/m^3 , and Q_r the regional heat sources W/m^3 . The actual values of these physical properties are shown in Table 3.1 [101].

Properties	Value	Properties	Value
Arterial temperature T_a ($^{\circ}C$)	37	Shear modulus G (Pa)	3.0×10^6
Thermal conductivity k ($\text{W}/(\text{mK})$)	0.5	Poisson's ratio for drained state ν	0.25
Density ρ (kg/m^3)	1000	Poisson's ratio for undrained state ν_u	0.31
Specific heat C ($\text{J}/(\text{kgK})$)	4000	Thermal expansion coefficient α (K^{-1})	1.0×10^{-4}
Blood perfusion rate w_b ($\text{kg}/(\text{m}^3\text{s})$)	0.5	Metabolic heat generation rate Q_m (W/m^3)	33800

Table 3.1: Thermal physical properties used in this computation.

In the case of bioheat transfer such as burn injury, the computational domain may be selected as a rectangular box as indicated in Fig. 3.1. The boundary conditions with respect to Eq. (3.1) corresponding to the computational domain shown in Fig. 3.1, where the space in the x direction starts from the body core ($x = 0$) and ends at the skin surface ($x = H$), can be described as [101]:

- (1) In the x direction, given temperature boundary condition is applied at the body core, i.e., $T = T_c$ at $x = 0$; convective boundary condition is used at the skin surface, $-k\frac{\partial T}{\partial x} = h_f(T - T_f)$ at $x = H$, which is the normal case that the skin surface is subjected to.
- (2) In the y direction, symmetric boundary conditions are employed on both the starting and ending edges, i.e., $-k\frac{\partial T}{\partial y} = 0$ at $y = 0$; $-k\frac{\partial T}{\partial y} = 0$ at $y = L$.
- (3) In the z direction, again symmetric boundary conditions are enforced, i.e., $-k\frac{\partial T}{\partial z} = 0$ at $z = 0$; $-k\frac{\partial T}{\partial z} = 0$ at $z = W$.

The specification of boundary conditions (2) and (3) can be justified as that the heating source is assumed to be located around the center in the $y - z$ plane at certain x position, for example, $x = h$, while the four borders parallel to the x axis in the computational domain are far away from the heating sources, hence symmetric boundary conditions can be used. The actual dimensions of the computational domain and locations of the heating sources will be given later.

3.2.2 Stress, strain, and displacement evolution

One of the destructive mechanisms for thermal damage of soft tissue is thermal induced high mechanical stress. To study the thermal induced deformation in soft tissue at high temperature, the thermoporoelasticity model is used in which stress, strain, pressure and temperature are related. The constitutive relation describing the elastic deformation of the soft tissue may be expressed by the modified Duhamel-Numann

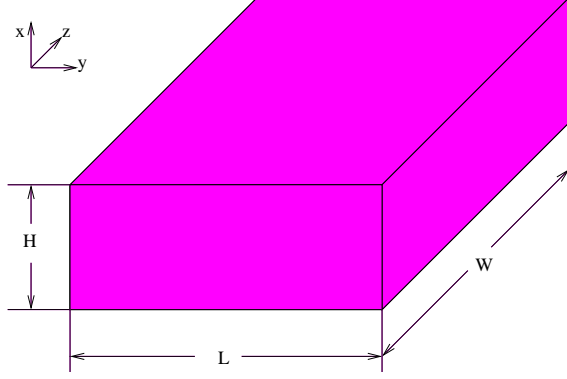


Figure 3.1: An illustration of the computational domain of a soft tissue.

equation for porous media as [59]

$$\sigma_{ij} = 2G(\varepsilon_{ij} + \frac{\nu}{1-2\nu}\epsilon_{kk}\delta_{ij}) - \frac{3(\nu_u - \nu)}{B(1+\nu_u)(1-2\nu)}p\delta_{ij} - \frac{2G\alpha(1+\nu)}{1-2\nu}\Delta T\delta_{ij}, \quad (3.2)$$

where $\epsilon_{kk} = \partial u_1/\partial x_1 + \partial u_2/\partial x_2 + \partial u_3/\partial x_3$, σ_{ij} and ε_{ij} are the second order total stress and average strain tensors ($i, j = 1, 2, 3$) respectively, p the fluid pressure inside the vasculature, and ΔT the temperature difference. Here, the temperature difference means the difference between the actual temperature and the reference temperature. In the case of human soft tissue, the reference temperature may be taken as 37 °C. The temperature for the tissue and the fluid in capillary beds is considered the same due to the fact that local heat exchange between the components may be rapid enough in comparison with global heat transfer and fluid flow. Other symbols in Eq. (5.1) are listed in Table 3.2. If the pressure term is not included, Eq. (5.1) is reduced to the stress equation in thermoelasticity to calculate thermal stresses [42].

Treat the tissue as the thermoporoelastic media, the equilibrium equation is [101]

$$G(u_{i,jj} + \frac{1}{1-2\nu}u_{j,ji}) - \frac{3(\nu_u - \nu)}{B(1+\nu_u)(1-2\nu)}p_{,i} - \frac{2G\alpha(1+\nu)}{1-2\nu}\Delta T_{,i} = 0, \quad (3.3)$$

where u_i is an average displacement vector of the porous matrix and is related to the strain tensor by the equation [101]

$$\varepsilon_{ij} = (u_{i,j} + u_{j,i})/2. \quad (3.4)$$

Symbol	Meaning	Symbol	Meaning
ϵ_{kk}	first partial derivative	G	shear modulus
σ_{ij}	2nd order total stress tensor	ν	Poisson's ratio for drained state
ϵ_{ij}	2nd order average strain tensor	ν_μ	Poisson's ratio for undrained state
p	fluid pressure inside the vasculature	B	Skempton's constant
ΔT	temperature difference	α	thermal expansion coefficient
δ_{ij}	Kronecker delta		

Table 3.2: Nomenclature for symbols used in Eq. (5.1).

The diffusion equation governing the fluid pressure changes in the tissue is

$$\frac{\partial p}{\partial t} = Cp_{,jj}, \quad (3.5)$$

where

$$C = \frac{2kGB^2(1 + \nu_u)^2(1 - \nu)}{9(1 - \nu_n)(\nu_u - \nu)}. \quad (3.6)$$

Eqs. (3.1), (5.1), (5.3), and (3.5) constitute the basic equations to describe the thermomechanical behavior of the soft tissues at high temperature, which is relative to the normal body temperature. In soft tissue, a temperature above 44 °C may be considered high, since that may cause burn injury [46]. If the soft tissue is treated as an isotropic elastic medium, the thermal deformation of the soft tissue can be described by thermoelasticity and Eq. (5.3) becomes [96]

$$G(u_{i,jj} + \frac{1}{1 - 2\nu}u_{j,ji}) - \frac{2G\alpha(1 + \nu)}{1 - 2\nu}\Delta T_{,i} = 0. \quad (3.7)$$

Thus the model is simplified to a quasi-steady state thermoelasticity problem. Together with boundary conditions, the response of biological bodies to high temperature and the corresponding deformation and stress and strain variations can be determined, from which the location of the thermomechanical damage due to temperature and stresses can be revealed. This will provide us with the necessary information on the approaches to protecting biological bodies at high temperature [101].

It needs to be made clear that after the finite difference discretization of Eq. (3.7), which will be introduced in the next section, the term ΔT goes to the right-hand side

and becomes a source term. The material properties and parameter related to the above equations are summarized in Table 3.1.

3.3 Numerical Techniques

3.3.1 Finite difference discretization

The thermomechanical interactions due to high temperature can be found by solving Eqs. (3.1) and (3.7). It is clear that in the proposed model, Eqs. (3.1) and (3.7) are not coupled. The strategy is to solve temperature from Eq. (3.1) first, then solve displacement from Eq. (3.7). Eq. (3.1) is time-dependent, and its solution has already been obtained in our previous work [54] using a Crank-Nicolson scheme based on the standard 7 point central difference discretization. In this chapter, we will stress on the solution of Eq. (3.7) using a finite difference scheme. Eq. (3.7) differs from Eq. (3.1) by [101]:

- (1) In Eq. (3.7) the unknown variables are a vector consisting of three components, i.e., displacements in the x , y , and z space directions, while in Eq. (3.1) there is only one unknown variable.
- (2) Unlike Eq. (3.1), there are some mixed derivatives in Eq. (3.7).
- (3) Eq. (3.1) is time-dependent, while Eq. (3.7) is not.

Therefore, it may not be very convenient to discretize Eq. (3.7) using the standard 7 point central difference scheme, instead, a 19 point finite difference scheme is employed in the discretization of Eq. (3.7), as

$$\sum_{i=1}^7 a_{i-1} u_{i-1} + \sum_{i=1}^4 a_{i+6} v_{i+6} + \sum_{i=1}^4 a_{9+2i} w_{9+2i} = F_x, \quad (3.8)$$

$$\sum_{i=1}^7 b_{i-1} v_{i-1} + \sum_{i=1}^4 b_{i+6} u_{i+6} + \sum_{i=1}^4 b_{10+2i} w_{10+2i} = F_y, \quad (3.9)$$

$$\sum_{i=1}^7 c_{i-1} w_{i-1} + \sum_{i=1}^4 c_{9+2i} u_{9+2i} + \sum_{i=1}^4 c_{10+2i} v_{10+2i} = F_z, \quad (3.10)$$

where a , b , and c are coefficients determined by the grid step size as well as the material properties of the medium, u , v , and w are displacements in the x , y , and z directions respectively, and F_x , F_y , and F_z are the body forces in the three spatial directions respectively. The three displacement components in Eq. (3.7) are expressed explicitly using u , v , and w , as can be seen in Eqs. (3.8), (3.9), and (3.10). The labeling of the grid points is shown in Fig. 3.2. Even though it is a 19 point finite difference scheme, only 15 points are used in each of the above 3 equations. For example, points 12, 14, 16, and 18 are not used in Eq. (3.8), points 11, 13, 15, and 17 not used in Eq. (3.9), and points 7, 8, 9, and 10 not used in Eq. (3.10) [101]. Without loss of generality,

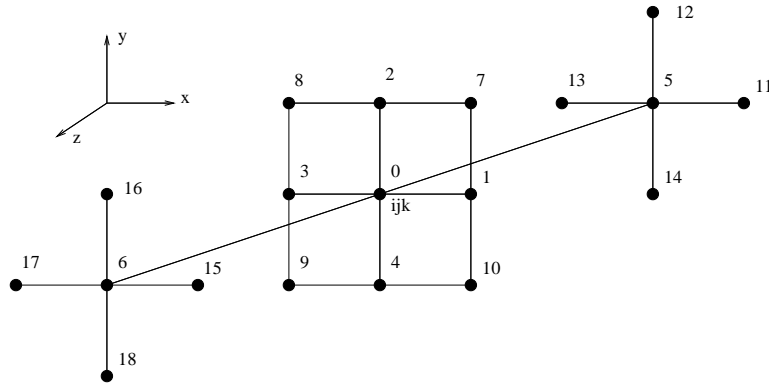


Figure 3.2: The 19 point finite difference stencil defined in a unit cube.

Eqs. (3.8), (3.9), and (3.10) may be expressed in the form of $Ax = b$, where A is the coefficient matrix, x is the unknown vector, and b is the right hand side. It is worth noticing that the number of rows and the number of columns in the resultant matrix A are triple of the number of internal grid points in a mesh, because of the fact that there are three unknowns at each of the grid point [101].

3.3.2 Iterative solver

The sparse linear system arising from the discretized equilibrium equation needs to be solved efficiently. Direct solution methods based on Gaussian elimination are prohibitively expensive for such large scale 3D problems in terms of memory cost

and CPU time. Thus iterative methods are generally believed to be a more viable means in such situations. In this chapter, one of the fastest iterative methods, a Krylov subspace method, is employed to solve the resulting linear systems. In order to reduce the number of iterations, a robust preconditioner is used as well. In particular, a linear system solver GMRES, a generalized minimal residual algorithm based on Arnoldi process and implemented with reverse communication, is chosen to do the computation [92].

The convergence rate of GMRES can be improved by a suitable preconditioning technique. For a linear system $Ax = b$, the preconditioned system may be written as [101]

$$(M_L^{-1}AM_R^{-1})(M_Rx) = M_L^{-1}b, \quad (3.11)$$

where M_L and M_R are left and right preconditioners respectively, and should be inexpensive to compute and easy to invert. The preconditioned linear system (3.11) itself should be easier to solve iteratively than the original one. If $M_R = I$, left preconditioning results. In contrast, if $M_L = I$, right preconditioning results.

As one of the best known preconditioning techniques, incomplete LU factorization is often applied to accelerate the convergence of GMRES, and widely used in solving linear systems arising from engineering and medical investigations. By neglecting most, or even all, the fill-in terms during the elimination process, the sparsity of the L and U factors is preserved in the ILU factorization. The product matrix LU is then only an approximation of the coefficient matrix. Here, a generic ILU algorithm with thresholding (ILUT) is used to construct the preconditioner for GMRES. More details about Krylov subspace methods and ILU factorization preconditioning techniques are introduced in Chapter 2 and can be found in [94].

3.4 Numerical Experiments and Discussion

Two numerical examples, hyperthermia and sinusoidal surface heating, are used to exhibit the thermomechanical interaction by the proposed model. The efficiency of ILUT in improving the computational performance is also investigated. In the computation, the geometry size related to Fig. 3.1 is selected as: $H = 0.03$ m, $L = W = 0.08$ m. The reason for such values is for the consideration of actual applications and the implementation of boundary conditions. In real situations, the interior tissue temperature usually tends to be constant within a short distance such as $2 \sim 3$ cm (x direction) starting from the skin surface [129, 54, 66]. The computational domain size in the y and z directions are chosen to be fairly large so that the symmetric boundary condition, i.e., no heat flux goes in or out of the interested domain in the y and z directions, can be implemented. The material properties and parameters in Eq. (3.1) are $\rho = \rho_b = 1000$ kg/m³, $C = C_b = 4000$ J/(kg°C), $T_a = T_c = 37$ °C, $k = 0.5$ W/(m°C), $w_b = 0.5$ kg/(m³s), $Q_m = 33800$ W/m³, as listed in Table 3.1. For simplicity, the surrounding fluid temperature is chosen as constant room temperature $T_f = 25$ °C [54, 25]. The material properties related to Eq. (3.7) are $G = 3.0 \times 10^6$ Pa, $\nu = 0.25$, $\nu_u = 0.31$, $\alpha = 1.0 \times 10^{-4}$ K⁻¹ [101].

3.4.1 Case study: hyperthermia model

Hyperthermia is a heat treatment to biological body, a tool fairly often used in clinical applications such as tumor control by artificially elevating the tissue temperature to gain therapeutic benefits. The treatment of hyperthermia may be local, regional, or whole body, and the corresponding heating style varies, such as microwave heating, ultrasound heating, electrode heating, or thermal dose [117]. Even though hyperthermia is difficult to implement technically, its medical value has been shown in greatly improving the therapy performance by combining with radiation treatment [91]. A typical clinical application of hyperthermia is the treatment of cancer by selectively

attacking deep-seated tumors with high temperature [58]. Due to the difference of heating sources, hyperthermia can be done either externally or internally. For example, the goal of standard hyperthermia treatments in internal heating is to raise the temperature in the target area to a higher degree, approximately 43 °C, than ordinary body temperature (37 °C) for up to one hour without excessively heating the adjacent tissues [6]. Patients usually do not feel comfortable with such a long time treatment. One drawback of the standard procedure is the difficulty in accurately providing the desired thermal dose because of the possible changes of blood flow rates and thermal properties and hence the change of heat transfer mechanism between tissues and blood flow due to temperature variation. An alternative way is the short duration high temperature thermal treatments, known as high-temperature thermal therapy [101].

For simplicity, only point heating is considered here to investigate the temperature response of tissue near tumor sites as did in some other research works [54, 25]. Practical examples of point heating can be found in clinical treatments where heat is deposited through inserting a conducting heating probe in the deep tumor site or delivering thermal dose to it. The point heating source to be studied is of the form [54]

$$Q_r(x, y, z, t) = P(t)\delta(x - x_0)\delta(y - y_0)\delta(z - z_0), \quad (3.12)$$

where $P(t)$ is the strength of the point heating source, which may vary with time, δ the Dirac function, and (x_0, y_0, z_0) the location of point heating. In the present example, we investigate the tissue thermal response of three point heating, and the consequent effect of temperature change on the stress and displacement of the tissue concerned. The locations of the heating sources are all chosen in the same cross section at $x = 0.009\text{m}$, and the coordinates of the three points are $(0.009, 0.032, 0.04)\text{m}$, $(0.009, 0.04, 0.028)\text{m}$, and $(0.009, 0.04, 0.028)\text{m}$, the same as in the work demonstrated by Deng and Liu [25]. Among the three point heating sources, the heating strength

is taken the same as $P(t) = 1.0 \times 10^7 \text{ W/m}^3$. It is assumed that the tissue is cooled by convection at the skin surface. The convection coefficient is $h_f = 100 \text{ W/m}^2$ and the temperature of the cooling medium is $T_f = 15 \text{ }^\circ\text{C}$ [101].

The determination of heating style, heating location, and heat transfer parameters in the simulation is for the purpose of convenience in presenting computational results, and to be consistent with those in some references [21, 66]. Of course they can be chosen as different values suitable for some applications consistent with the model [101].

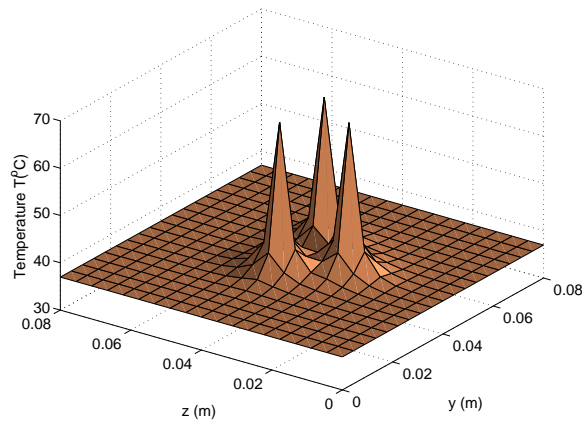


Figure 3.3: Temperature distribution at $x = 0.09 \text{ m}$ and $t = 200 \text{ s}$ (hyperthermia).

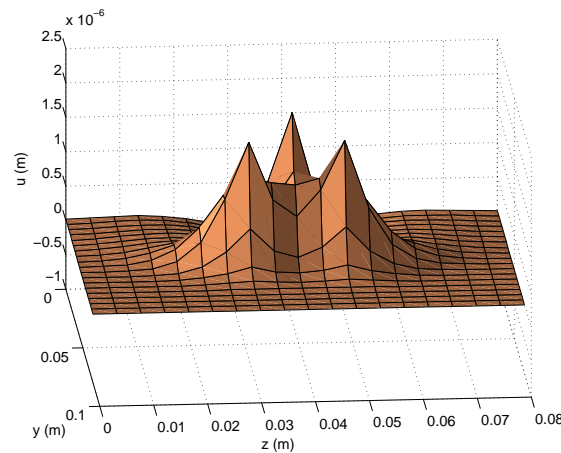


Figure 3.4: u displacement at $x = 0.009 \text{ m}$ and $t = 200 \text{ s}$ (hyperthermia).

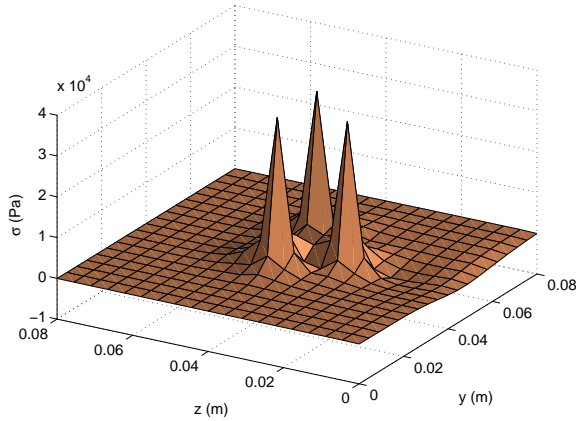


Figure 3.5: Average normal stress \tilde{P} at $x = 0.009$ m and $t = 200$ s (hyperthermia).

In the quasi-steady state model, the time dependent thermomechanical responses can be achieved by solving the heat equation to get transient temperature distribution, and then solving the equilibrium equation to get displacement distribution based on the temperature at each time step. For brevity, only results in the $(y-z)$ plane at $x = 0.009$ m, where the three point heating sources locate, are displayed. Fig. 3.3 shows the temperature distribution at $t = 200$ s, Fig. 3.4 is the corresponding displacement distribution in the x space direction. The stress distribution is presented in Fig. 3.5 in the form of pressure \tilde{P} , calculated as [101]

$$\tilde{P} = -\frac{\sigma_{xx} + \sigma_{yy} + \sigma_{zz}}{3}. \quad (3.13)$$

As shown in Fig. 3.3, the highest temperature is in the position where the heating source is placed. The same is true for the displacement (Fig. 3.4) and stress (Fig. 3.5). It can be deduced without much difficulty that the tissue in the heated position is more likely to be damaged than that in locations that are not heated. This is what we expected in heat therapy by heating the target to a certain temperature to damage it and eventually kill it without major injury to the neighboring healthy tissues.

The thermomechanical interaction has been presented at a fixed time $t = 200$ s and different locations, as shown in Figs. 3.3 - 3.5. In the following space, we will

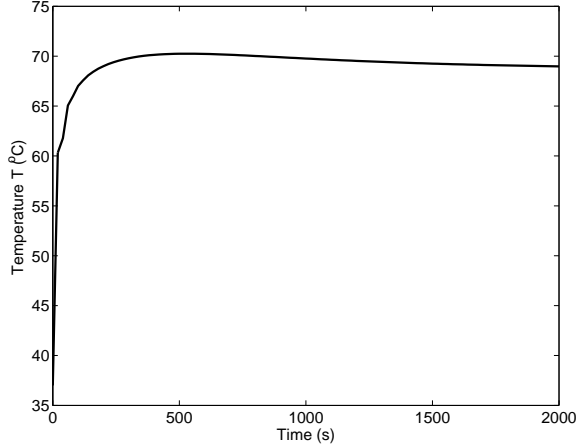


Figure 3.6: Transient temperature distribution at $(0.009, 0.032, 0.04)\text{m}$ (hyperthermia).

show the thermal and mechanical responses at a fixed location but different time. For brevity, only the result at one of the three positions where heating sources are located, i.e., $(x_0, y_0, z_0) = (0.009, 0.032, 0.04)\text{m}$, is plotted, as displayed in Figs. 3.6 - 3.8. The variation of temperature with time is exhibited in Fig. 3.6, and that of stress is shown in Fig. 3.8. It can easily be seen that both temperature and stress have similar trend. That is probably because the thermal stress overwhelms mechanical stress in this particular case. The temperature increases rapidly in the early time of heating, reaches a peak value, then decreases gradually towards steady-state. That is because of the convection between the skin surface and the surrounding media with a lower temperature of $T_f = 15\text{ }^\circ\text{C}$. Fig. 3.7 is the change of displacement with time due to temperature difference. All three components of displacement increase with time first fast and then gradually[101].

3.4.2 Case study: sinusoidal surface heating model

Oscillating heating is a common technique in thermal analysis, such as the application of modulated temperature programming to the investigation of thermomechanical interaction [87]. One example is the recent usage in thermogravimetry of modulated

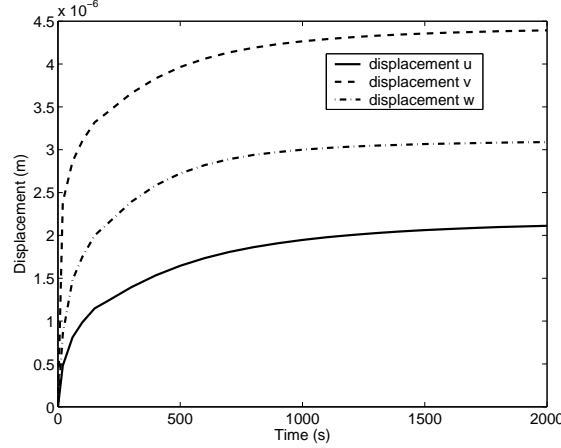


Figure 3.7: Transient displacement distribution at (0.009, 0.032, 0.04)m (hyperthermia).

temperature programs to determine the degradation kinetics of materials. A sinusoidal temperature profile is the most common one among the various oscillating heating modulations. Sinusoidal surface heating can be generated by an instrument with repeated irradiation from regulated laser, and is used to estimate the blood perfusion [82]. The sinusoidal heating is taken in the form of [25]

$$f(t) = q_0 + q_w \cos \omega t, \quad (3.14)$$

where, $f(t)$ is heat flux (W/m^2), q_0 a constant, q_w the constant oscillation amplitude of sinusoidal heating, ω the heating frequency. Eq. (3.14) is actually the flux on the skin surface provided by some external devices. In computation, the sinusoidal heating is implemented by specifying a given heat flux boundary condition on the skin surface. The actual form of Eq. (3.14) is taken as [100]

$$f(t) = 1000 + 500 \cos(0.02t). \quad (3.15)$$

The transient thermomechanical response in the case of surface heating are presented in Figs. 3.9 - 3.11. The temperature changes with time at the skin surface corresponding to Eq. (3.15) can be seen in Fig. 3.9. Because of continuous heating, the temperature on the skin surface increases gradually. It is clear, there are about six

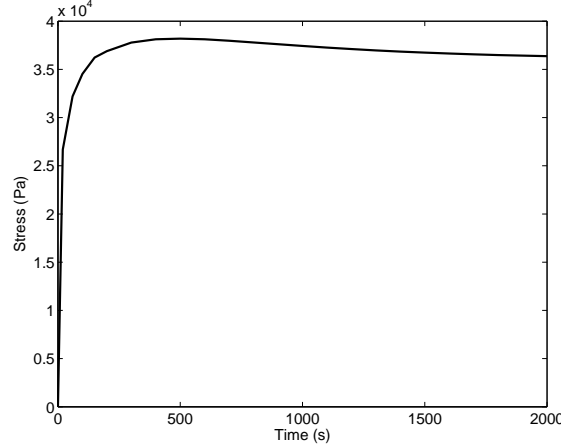


Figure 3.8: Transient average stress distribution \tilde{P} at (0.009, 0.032, 0.04)m (hyperthermia).

cycles in the history of temperature variation, which is due to the value of ω in Eqs. (3.14) and (3.15). In the case of $\omega = 0.02$, the period of cosine function is 100π seconds, and there are approximately six cycles in 2000 seconds. The thermal-induced displacement is shown in Fig. 3.10. Similar periodical changes can be observed. As expected, the magnitude of displacement variation is greatest for component u , since the temperature changes only in the x direction by the specified boundary conditions: symmetric in both the y and x directions. The thermal-induced stress also changes oscillatorily as displayed in Fig. 3.11 [101].

3.4.3 Computational Performance

Uniform grids are used in all the three space directions in numerical computation, also the same number of grid intervals are assigned in each of them. In the numerical examples done in both Sections 3.4.1 and 3.4.2, twenty equally spaced grid intervals are used, i.e., $19 \times 19 \times 19$ internal grid points. The consequent number of unknowns are $57 \times 57 \times 57$, as shown in Table 3.3. The information of the coefficient matrix A for the mesh size of $39 \times 39 \times 39$ is included in Table 3.3 as well. The computation was done on a Sun-Blade-100 machine with a single 500 MHz SPARC processor and

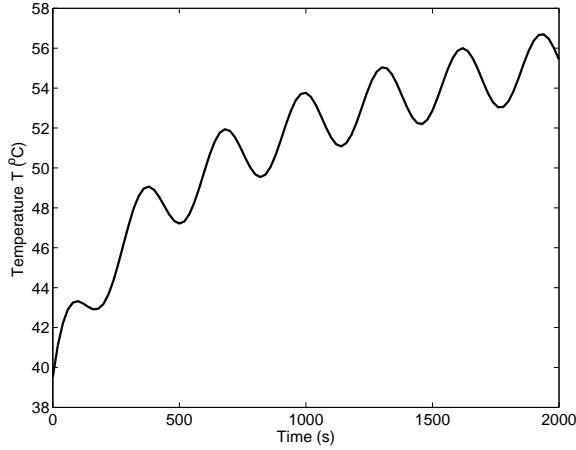


Figure 3.9: Transient temperature at skin surface (sinusoidal heating).

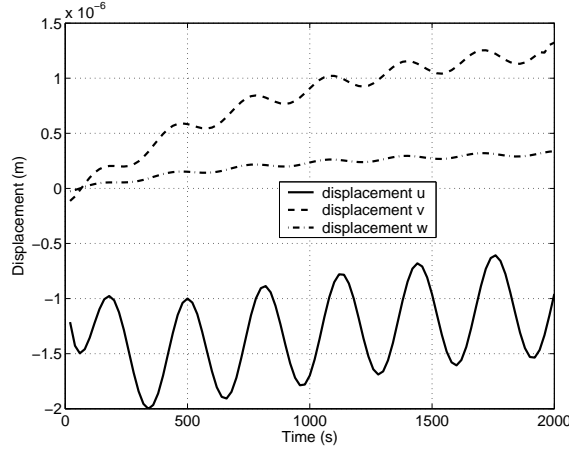


Figure 3.10: Transient displacement at skin surface (sinusoidal heating).

2 GB memory [101].

Tables 3.4 and 3.5 present the computational performance with and without the ILUT preconditioner for two kinds of mesh sizes, i.e., $n = 6859$ and $n = 59319$, for the hyperthermia case study. In both cases, the parameters in the ILUT preconditioner are the same, i.e., drop tolerance $\tau = 10^{-4}$, number of fill-ins $p = 40$, and the size of the Krylov subspace is 50. It can be seen that the use of the ILUT preconditioner has greatly improved the computational performance. In the case of $n = 6859$ (coarser grid), the number of iterations with the ILUT preconditioner is about eight times

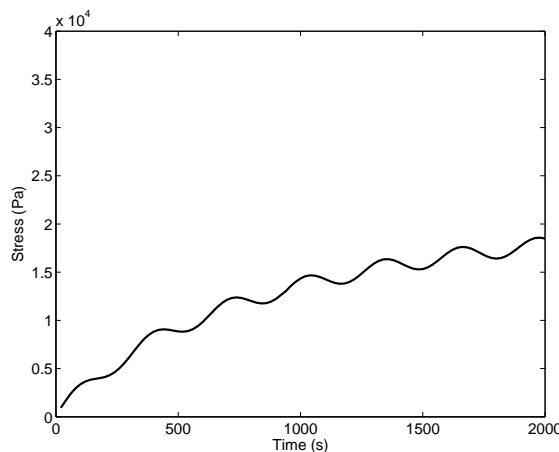


Figure 3.11: Transient average normal stress at skin surface (sinusoidal heating).

Mesh size	No. of unknowns	No. of nonzeros
6859	20577	285285
59319	177957	2569905

Table 3.3: Information on the coefficient matrix A for various mesh sizes (hyperthermia).

less than that without the preconditioner. In the case of $n = 59319$ (finer grid), the number of iterations with the ILUT preconditioner is about fifty times less than that without the preconditioner. The total CPU time when using the ILUT preconditioner is less than a half of that without using the preconditioner in the coarser grid case, and about one fifth in the finer grid case [101]. So the advantages of using the ILUT preconditioner are more remarkable when a finer grid discretization is used [103].

The influence of stop criterion on the computational cost is also studied in terms of number of iterations and CPU time. As shown in Tables 3.4 and 3.5, both the number of iterations and the total CPU time increase when the stop tolerance is changed from 10^{-9} to 10^{-12} [101].

$n = 6859$	$\delta = 10^{-9}$		$\delta = 10^{-12}$	
	with ILUT	without ILUT	with ILUT	without ILUT
Computational cost	8	201	10	258
No. of iterations	8	201	10	258
Factorization time	7.85	-	7.71	-
Total CPU time	9.48	20.59	9.73	27.20
Number of fill-ins	40	-	40	-
Krylov subspace size	50	50	50	50

Table 3.4: Computational performance with/without ILUT at $n = 6859$ (hyperthermia).

$n = 59319$	$\delta = 10^{-9}$		$\delta = 10^{-12}$	
	with ILUT	without ILUT	with ILUT	without ILUT
Computational cost	9	452	11	542
No. of iterations	9	452	11	542
Factorization time	90.20	-	90.65	-
Total CPU time	106.08	498.13	111.15	590.76
Number of fill-ins	40	-	40	-
Krylov subspace size	50	50	50	50

Table 3.5: Computational performance with/without ILUT at $n = 59319$ (hyperthermia).

3.5 Summary

Thermomechanical interactions were investigated in a three dimensional Cartesian coordinates. Pennes bioheat equation and the modified Duhamel-Neuman equations were proposed to model the thermal-induced mechanical behavior. We used the quasi-steady state thermoelasticity, where temperature and mechanical properties are not coupled and they are solved independently. The temperature is considered time-dependent, which is solved using a Crank-Nicolson numerical scheme. The mechanical properties themselves are not time-dependent, but they are related to temperature variations, so the transient mechanical properties such as displacement and stress can also be attained by solving them for various temperature distributions at each time step.

The heat equation was discretized using the standard 7 point central difference scheme, while the mechanical equilibrium equations were done by a 19 point finite difference scheme. Both of the schemes are second-order in accuracy. The resulting

sparse linear systems from the discretization of both the heat transfer equation and the mechanical equilibrium equations are solved iteratively using GMRES solvers accompanied with the ILUT preconditioners. Both the number of iterations and the total CPU time are reduced in a great margin when the ILUT preconditioners are used.

Two numerical experiments were conducted, hyperthermia and sinusoidal heating, which represent typical heat transfer processes involved in soft tissues in biological bodies, such as heat therapy and skin burn. As expected, we obtained the time-dependent temperature distribution as well as the corresponding thermal-induced mechanical responses.

4 Thermal Response of Skin Subject to Laser Heating

4.1 Introduction

Since the advent of the first working laser in 1960, there have been many laser-related applications [2, 5, 70, 44, 127]. Among them, laser medicine is probably one of the most popular applications, e.g., the use of lasers in dermatology, such as skin resurfacing, removal of vascular lesions, laser-assisted hair removal, tattoo removal, and so on. Due to many innovations in technology, different lasers have been developed to perform specific tasks, which has dramatically increased the use of laser in dermatology.

The use of lasers in dermatology can be traced back to 1963 by Leon for a test in human skin [118]. The first medical lasers were continuous beam lasers such as CO₂ laser, argon laser, and Nd:YAG laser. Even though these lasers are fairly effective, their applications are limited by the fact that the results are operator dependent, and may be affected by the speed of surgeon's hand, and may lead to undesirable risks such as scarring due to excessive thermal injury of normal skin [74]. This problem was solved by the theory of selective photothermolysis introduced by Anderson and Parrish in 1983 [4]. The selective photothermolysis can be accomplished by properly choosing a wavelength, pulse duration, and pulse energy that can be best absorbed by a specific target with a particular chromophore. That technique requires that the wavelength of the laser light be absorbed by the target in order to have an effective treatment and the laser energy be confined to the intended target [52]. Newly developed flashlamp-pumped, pulsed-dye, copper-vapor, and Q-switch lasers pertain such properties.

In the use of pulsed laser emission, the intended target experiences thermal cooling during the intervals between any two adjacent pulses. For better description of laser operation, the thermal relaxation time (TRT) is introduced and defined as the time during which 50% of the incident heat has transferred out of the target vessel to

adjacent tissues [5, 52]. If the pulse width is equal to or less than the TRT of the chromophores, the resultant thermal damage will be confined to the chromophore. Ideally, in clinical applications, the energy of laser is high enough to damage the chromophore, while the pulse duration of laser is shorter than the thermal relaxation time of the target. The depth that laser light penetrates into the skin is determined by the wavelength of the laser light as well as the absorption spectrum of the encountered chromophores.

In the treatment of dermatologic laser surgery, the laser light may be reflected from, transmitted through, or absorbed by the skin. For the purpose of clinical effect, it is desirable that the emitted laser light can be absorbed by the intended targets and converted to thermal energy to heat the target to an appropriate temperature. Unavoidably, the temperature of normal tissue surrounding the intended targets is increased to certain extent.

The skin is sensitive to temperature change. The effect may not be significant when the temperature at the skin surface is below 44°C. However, if the surface temperature is above 44°C, irreversible damage may happen. An investigation of the heating intensity and the duration of the exposure suggested that when the surface temperature is greater than 51°C, the exposure time required to destroy the epidermis is so short that the deeper layers of cells are brought to a state of thermal equilibrium with the surface and the trans-epidermal necrosis may occur [73]. When the exposure temperature is raised as high as 100°C, steam may be formed and intensive vaporization will cause acute disruption to the skin. Higher temperatures will further incur tissue burning and carbonization.

We propose to investigate the tissue thermal response to laser heating before a dermatological surgery is operated to minimize the possible adverse effects and complications associated with the surgery. A multilayer model based on the physical structure of human skin is employed to predict the temperature distribution of living

tissues when they are treated by lasers. The objective of this work is trying to provide a quantitative connection between a dermatological surgery laser and the corresponding tissue thermal response. The resulting quantitative description is very important for choosing an appropriate laser, using suitable laser pulse duration, deciding proper laser output power, and determining accurate total exposure time.

Very often the related mass transfer such as water evaporation and diffusion is not considered in modeling the tissue response of high temperature exposure [2, 44, 124]. However, water transport may play an important role in this process [70], and the heat loss due to the surface evaporation of water may become a dominant term in the heat transfer equation [119].

We develop a 3D numerical model to predict the transient temperature distribution in skin tissues with the consideration of water evaporation on the skin surface and water diffusion in the tissue. The standard 7 point finite difference scheme which is second order in accuracy is used to discretize the 3D partial differential equations. We apply an iterative method to obtain the solution of the resultant linear systems.

4.2 The Multilayer Model

The transient temperature variation in living tissue due to internal or external heating can be described by Pennes bioheat equation [85], which expresses the energy conservation in biological body where the thermal energy is assumed to be transferred by diffusion only, i.e., Fourier heat conduction, and is widely used in modeling the thermal response of biological tissue [30, 66, 67]. In the case that human skin is subject to laser heating, the modified bioheat transfer equation including the heat losses due to water evaporation and diffusion, may be written as [30, 70, 44]

$$\rho C \frac{\partial T}{\partial t} = k \frac{\partial^2 T}{\partial x^2} + k \frac{\partial^2 T}{\partial y^2} + k \frac{\partial^2 T}{\partial z^2} + w_b C_b (T_a - T) + Q_m + Q_r + Q_e + Q_d. \quad (4.1)$$

Eq. (4.1) is similar to Eq. (3.1), with two additional terms, Q_e and Q_d , where Q_e is the volumetric heat loss from water evaporation on the surface of the skin (W/m^3),

Q_d the volumetric heat loss due to water diffusion in the tissue (W/m^3), and Q_r the regional heat sources (W/m^3), which can be interpreted as

$$Q_r = \mu_a \phi(x, y, z) f(t), \quad (4.2)$$

where μ_a is the tissue absorption coefficient ($1/\text{m}$), $\phi(x, y, z)$ the local fluence rate of the laser light (W/m^2), and $f(t)$ the time function related to the laser pulse duration and the intervals between each duration. The local fluence rate of laser light is expressed as a product of irradiation, Gaussian shaped laser beam, and Beer's law of axial attenuation [44]

$$\phi(x, y, z) = E \exp(-2(y^2 + z^2)/W^2) \exp(-\mu_a x), \quad (4.3)$$

where E is the incident irradiance (W/m^2), defined as $E = 2P/(\pi W^2)$, P the laser power (W). W is the $1/e^2$ waist (m). The time function $f(t)$ is supposed to be periodic and may be expressed as [100]

$$f(t) = \begin{cases} 1 & (i-1)P_e < t < [(i-1) + \kappa]P_e, \\ 0 & [(i-1) + \kappa]P_e < t < iP_e, \end{cases} \quad i = 1, 2, 3, \dots, \quad (4.4)$$

in which i is the number of periods, P_e the period s, κ the fraction of period in which the skin is exposed to laser source.

We develop a 3D multilayer model to predict the skin temperature distribution when the skin surface is exposed to laser heating. The multilayer model is based on the actual skin structure. The human skin may be divided into three layers. Starting from the top of the skin surface toward the body core, they are the epidermis, the dermis, and the subcutaneous [120], as shown in Fig. 4.1. The boundary conditions with respect to Eq. (4.1) corresponding to the computational domain shown in Fig. 4.1, where the space in the x direction starts from the body core ($x = 0$) and ends at the skin surface ($x = H$), can be described as [101, 104]:

- (1) At $x = 0$, $T = T_c$, and at $x = H$, $-k \frac{\partial T}{\partial x} = h_f(T - T_f)$. Usually the skin is intentionally cooled externally, e.g., using cryogen spray cooling in laser surgery

[1, 23, 115], and the heat transfer rate due to convection is much higher than that from the skin surface radiation, so the effect of radiation from the skin surface may be neglected.

(2) At $y = 0$, $-k \frac{\partial T}{\partial y} = 0$, and at $y = L$, $-k \frac{\partial T}{\partial y} = 0$.

(3) At $z = 0$, $-k \frac{\partial T}{\partial z} = 0$, and at $z = W$, $-k \frac{\partial T}{\partial z} = 0$.

Since the heating source is assumed to be in the center of the skin surface under investigation, and the computational domain is selected as 1/4 of the entire domain under investigation, it is convenient to use symmetrical boundary conditions at $y = 0$ and $z = 0$. The specification of symmetrical boundary conditions at $y = L$ and $z = W$ can be justified by the reality that the corresponding two borders parallel to the x axis are far away from the heating source, hence the temperature near the borders may not be affected by the heating source. The actual dimensions of the computational domain and locations of the heating sources are given in Section 4.6. In the case of symmetrical heating source, a 2D modeling in the cylindrical coordinates may be used. However, the present method can cope with complex 3D heating patterns such as that by an array of laser beams.

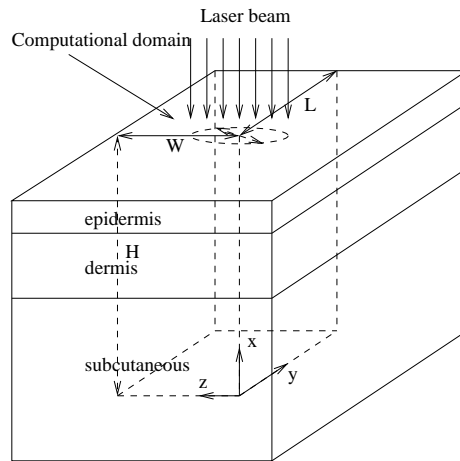


Figure 4.1: The computational domain of a soft tissue (a three layer skin).

4.3 Water Evaporation and Diffusion

The evaporation of water is the diffusion of water molecules from the water surface to the atmosphere through the boundary layer covering the water surface. So, the rate of water evaporation equals the rate of diffusion of water molecules [47]. The heat loss due to evaporation Q_e in Eq. (4.1) can then be expressed as [70]:

$$Q_e = \dot{m}\Delta H_{vap}, \quad (4.5)$$

where \dot{m} is the rate of water vaporization from the skin surface (kg/(m²s)), ΔH_{vap} the enthalpy of vaporization of water, a function of temperature as tabulated in [63]. For the convenience of computation, the tabulated data is fitted to a 4th degree polynomial using the least-squares fitting over the temperature range of 0 ~ 300°C, which is

$$\Delta H_{vap} = 45.0445 - 0.0411T_w - 2.8664 \times 10^{-5}T_w^2 + 9.2581 \times 10^{-8}T_w^3 - 9.0013 \times 10^{-10}T_w^4, \quad (4.6)$$

in which T_w is the water temperature that is assumed to be equal to the tissue temperature (°C), and standard derivation of the data fitting is 0.01358. The concentration of water vapor near the skin surface is higher than that in the dry air, so there exists a force that drives the vapor flowing away from the skin surface to the dry air. The rate of water vaporization can be expressed as a function of the gradient of water vapor concentration [47, 70], i.e.,

$$\dot{m} = D_a \frac{\partial c_w}{\partial x} = D_a \frac{\partial}{\partial x} \left(\frac{M_w P_w}{RT_w} \right), \quad (4.7)$$

where D_a is the water vapor diffusion coefficient in air (m²/s), M_w the molecular weight of water, a constant value (g/mol), R the universal gas constant (J/mol°K), P_w the vapor pressure of water (Pa), and T_w the temperature of the water vapor (°K). Assume that the air flow on the skin surface is laminar and there exists a steady-state

boundary layer, we then rewrite Eq. (4.7) in the following form [70]

$$\dot{m} = \bar{D}_a \frac{M_w}{R} \frac{\left(\frac{P_w}{T_w}\right)_s - \left(\frac{P_w}{T_w}\right)_a \times H_r}{\bar{\delta}_c}. \quad (4.8)$$

Here \bar{D}_a is the average water vapor diffusivity in the boundary layer covering the water surface, and H_r the relative humidity of the air. The subscript $()_s$ or $()_a$ denotes the properties on the skin surface and in the air respectively. $\bar{\delta}_c$ is the average thickness of the boundary layer over which a water vapor concentration gradient occurs. The boundary layer of water vapor transfer can be determined by the exact analysis of the laminar flow as [131]

$$\frac{\delta}{\bar{\delta}_c} = Sc^{1/3} = \left(\frac{\nu}{D_a}\right)^{1/3}, \quad (4.9)$$

where δ is the thickness of the hydrodynamic boundary layer (m), $\bar{\delta}_c$ the thickness of the concentration boundary layer (m), ν the kinetic viscosity of air (m^2/s), and Sc is the Schmidt number, which is defined as the ratio of the momentum diffusivity to the mass diffusivity. In the case of a laminar flow over a flat plate, the thickness of the hydrodynamic boundary layer can be found by the Blasius's solution as

$$\delta_x = 5 \sqrt{\frac{\nu x}{v_\infty}}, \quad (4.10)$$

where v_∞ is the air velocity far away from the skin surface (m/s), x is the location on the skin surface (m), and δ_x is the thickness of momentum boundary layer at the location of x (m). Hence the average thickness of momentum boundary layer over the distance of L is found to be

$$\delta = \frac{10}{3} \sqrt{\frac{\nu L}{v_\infty}}. \quad (4.11)$$

In the simulation, the dynamic viscosity of air ν and the diffusivity of water vapor in air D at the temperature of 25°C are taken to be $1.57 \times 10^{-5} \text{ m}^2/\text{s}$ and $2.6 \times 10^{-5} \text{ m}^2/\text{s}$ [131] respectively. The free-stream velocity of air v_∞ is assumed to be 0.5 m/s, and the distance L to be 0.03 m. The resulting average thickness of the water vapor concentration boundary is 0.0038 m.

In Eq. (4.8), the vapor pressure P_w is a function of temperature and is obtained by an 8th degree polynomial according to the table of vapor pressure of water in [64]. The following polynomial shows the dependence of vapor pressure on the temperature in the range of $0 \sim 250^\circ C$, from a least-squares data fitting,

$$P_w = 0.6027 + 0.04761T_w + 1.158 \times 10^{-3}T_w^2 + 3.5959 \times 10^{-5}T_w^3 + 1.3926 \times 10^{-7}T_w^4 + 3.4857 \times 10^{-9}T_w^5 + 2.0523 \times 10^{-12}T_w^6 - 2.8046 \times 10^{-14}T_w^7 + 3.8649 \times 10^{-17}T_w^8, \quad (4.12)$$

in which T_w is the temperature of tissue surface ($^\circ C$). The standard derivation of the above least-squares data fitting is 0.02954. The diffusivity of water vapor in air is also temperature dependent. Again the temperature dependency of the diffusivity of water vapor in air is expressed by a 2nd degree polynomial for the temperature range of 293.15 $^\circ K$ to 673.15 $^\circ K$ under the atmosphere pressure, which is

$$D_a = 8.8187 \times 10^{-7}T^2 + 0.001506T - 0.2784, \quad (4.13)$$

where D_a is in the unit of (cm^2/s) and T is the absolute temperature of air in the vapor boundary-layer covering skin surface, which is approximated as the average of the skin surface temperature and the surrounding environment temperature ($^\circ K$). Eq. (4.13) is based on the tabulated data in [65], and the standard derivation of the least-squares data fitting is 0.007315.

Due to the evaporation of water from the skin surface, there exists a gradient of water density in the tissue with lower density near the skin surface and higher density inside the skin, that causes possible water transport from the sub-surface toward the surface. The water transport in skin may be expressed by Fick's law of diffusion, which in rectangular coordinates is written as [131]

$$\frac{\partial \rho_w}{\partial t} = D \left[\frac{\partial^2 \rho_w}{\partial x^2} + \frac{\partial^2 \rho_w}{\partial y^2} + \frac{\partial^2 \rho_w}{\partial z^2} \right], \quad (4.14)$$

where D is the coefficient of water diffusion in tissue (m^2/s) and ρ_w the corresponding water density (g/m^3). The coefficient of water diffusion in the skin is taken as $D =$

$5 \times 10^{-10} \text{ m}^2/\text{s}$, as used in [27, 70]. The distribution of water density in the tissue can be obtained from Eq. (4.14), and the flow rate of water diffusion may be estimated as [27]

$$W = -D \frac{d\rho}{dx} \approx -D \frac{\Delta\rho}{\Delta x}, \quad (4.15)$$

where $\Delta\rho$ is the difference of water content between the skin surface and the inner tissue, and Δx the thickness of tissue investigated. The volumetric heat transfer rate due to water diffusion is then calculated as

$$Q_d = \frac{Dc_p(\rho_s - \rho_c)(T - T_c)}{(\Delta x)^2}, \quad (4.16)$$

where c_p is the specific heat of water ($\text{J}/\text{Kg}^\circ\text{C}$), ρ_s the water content on the skin surface, ρ_c the water content in body core, T the tissue temperature, T_c the temperature in body core. Eq. (4.16) can be further simplified as a convection-like term,

$$Q_d = h_w(T - T_c), \quad (4.17)$$

where h_w is the volumetric heat transfer coefficient ($\text{W}/(\text{m}^3\text{C})$), given by $h_w = Dc_p(\rho_s - \rho_c)/(\Delta x)^2$.

4.4 Numerical Scheme and Solution Strategy

The inclusion of two extra terms, the volumetric rate of heat loss due to evaporation Q_e and due to water diffusion Q_d , causes more complexity in the computation. Since evaporation happens only on the skin surface, the evaporation term Q_e is handled by considering it as a part of the boundary condition on skin surface. As a result of using an 8th degree polynomial to describe the temperature dependency of water vapor pressure and using a 4th degree one for the temperature dependency of the enthalpy of water vaporization, Q_e is approximated by a highly nonlinear 12th degree polynomial. If the Newton's method is used for linearization, a high computation cost must be paid. Instead, a simple way of linearization is preferred in our computation.

The 12th degree polynomial of Q_e may be written as

$$Q_e = c_0 + c_1T + c_2T^2 + \cdots + c_{12}T^{12}, \quad (4.18)$$

which can be further approximated as

$$Q_e = c_0 + (c_1 + c_2T_0 + c_3T_0^2 + \cdots + c_{12}T_0^{11})T, \quad (4.19)$$

where c_0, c_1, \dots , and c_{12} are constant values obtained from Eqs. (4.5), (4.6), (4.8), and (4.12), and T_0 is the temperature obtained from the previous time step. Thereafter the nonlinearity is solved by using a linear expression of the temperature dependency. As shown before, the term due to water diffusion Q_d may be dealt with an addition of a convection-like term. Eq. (4.1) can then be expressed in the following form

$$\rho C \frac{\partial T}{\partial t} = k \frac{\partial^2 T}{\partial x^2} + k \frac{\partial^2 T}{\partial y^2} + k \frac{\partial^2 T}{\partial z^2} + w_b C_b (T_a - T) + h_w (T_c - T) + Q_m + Q_r. \quad (4.20)$$

For the brevity of expression, Let \mathcal{L} be the elliptic operator defined by [54]

$$\mathcal{L}T = k \frac{\partial^2 T}{\partial x^2} + k \frac{\partial^2 T}{\partial y^2} + k \frac{\partial^2 T}{\partial z^2} - w_b C_b T - h_w T, \quad (4.21)$$

then Eq. (4.20) can be written as,

$$\rho C \frac{\partial T}{\partial t} = \mathcal{L}T + w_b C_b T_a + h_w T_c + Q_m + Q_r. \quad (4.22)$$

Let \mathcal{A} be the finite difference approximation of \mathcal{L} with the p -th order of accuracy and rewrite Eq. (4.22), we have the following expression,

$$\frac{\partial T}{\partial t} = \alpha \mathcal{A}T + S, \quad (4.23)$$

where $\alpha = k/(\rho C)$, $\mathcal{A}T \approx \mathcal{L}T + \mathcal{O}(h^p)$, h the maximum of the step sizes in the x , y , and z space directions, and $S = (w_b C_b T_a + Q_m + Q_r)/(\rho C)$. Using the Crank-Nicolson scheme and the standard 7 point central finite difference approximation, the following expression can be derived from Eq. (4.23),

$$\frac{T^{n+1} - T^n}{\Delta t} = \frac{1}{2} \alpha \mathcal{A}T^{n+1} + \frac{1}{2} \alpha \mathcal{A}T^n + S^{n+1/2}. \quad (4.24)$$

Here Δt is the time step. The truncation error of the scheme is $E = \mathcal{O}(\Delta t^2 + h^2)$. Eq. (5.8) may be written in a matrix form as,

$$\left(I - \frac{\alpha\Delta t}{2}\mathcal{A}\right)T^{n+1} = \left(I + \frac{\alpha\Delta t}{2}\mathcal{A}\right)T^n + \alpha\Delta tS^{n+1/2}. \quad (4.25)$$

The reason that we use the Crank-Nicolson scheme is that the scheme is easy to implement, theoretically highly stable, and second-order accurate in both space and time. In some applications, the physics of the investigated problems needs to be considered, and additional limitations may be required for the usage of the scheme. That will be discussed in the next section.

We need to solve the sparse linear system, Eq. (4.25). Large sparse linear systems arising from 3D problems are usually solved by iterative methods. Stationary iterative methods such as Jacobi method and Gauss-Seidel method are simple to derive and implement, however, their rate of convergence is slow and the convergence is only guaranteed for certain classes of matrices. The successive overrelaxation method, converging an order of magnitude faster than Gauss-Seidel method, is still considerably slow compared with modern projection based methods. We use GMRES to solve the linear system. If the m -th approximation to the solution is used, the subspace would be a span of the set of vectors $\{r^{(0)}, Ar^{(0)}, A^2r^{(0)}, \dots, A^{m-1}r^{(0)}\}$, where $r^{(0)}$ is the residual corresponding to the initial guess. In GMRES, the modified Gram-Schmidt method is used to construct orthogonal bases of the Krylov subspace [92].

The above-described procedure is for solving the bioheat equation. The water transport equation, Eq. (4.14), is also a Poisson's equation, which can be solved by the same procedure as used for the heat equation. Moreover, Eqs. (4.1) and (4.14) are coupled by boundary conditions. The rate of water loss on the skin surface is a function of temperature. They are decoupled by solving Eq. (4.1) to get the temperature distribution and then using the temperature on the skin surface to calculate the rate of water transport.

4.5 Stability Analysis

The Crank-Nicolson scheme takes the average of the right-hand side between the beginning and the end of each time step for the discretization in time domain and is known unconditionally stable. But if the time step is too large, solutions could be locally oscillatory and eventually become nonphysical. In some computations, where density, absolute temperature, and any other non-negative properties are involved, the dependent variables can never become negative physically, the actual time-step we can use should be limited. Using the bioheat equation as an example, we can rewrite Eq. (5.8) in full as the following,

$$\begin{aligned}
& \frac{T_{i,j,k}^{n+1} - T_{i,j,k}^n}{\Delta t} = \\
& \frac{1}{2}\alpha \left(\frac{T_{i+1,j,k}^n - 2T_{i,j,k}^n + T_{i-1,j,k}^n}{\Delta x^2} + \frac{T_{i,j+1,k}^n - 2T_{i,j,k}^n + T_{i,j-1,k}^n}{\Delta y^2} + \frac{T_{i,j,k+1}^n - 2T_{i,j,k}^n + T_{i,j,k-1}^n}{\Delta z^2} \right) \\
& + \frac{1}{2}\alpha \left(\frac{T_{i+1,j,k}^{n+1} - 2T_{i,j,k}^{n+1} + T_{i-1,j,k}^{n+1}}{\Delta x^2} + \frac{T_{i,j+1,k}^{n+1} - 2T_{i,j,k}^{n+1} + T_{i,j-1,k}^{n+1}}{\Delta y^2} + \frac{T_{i,j,k+1}^{n+1} - 2T_{i,j,k}^{n+1} + T_{i,j,k-1}^{n+1}}{\Delta z^2} \right) \\
& - \frac{1}{2} \frac{w_b C_b T_{i,j,k}^n}{\rho C} - \frac{1}{2} \frac{w_b C_b T_{i,j,k}^{n+1}}{\rho C} - \frac{1}{2} \frac{h_w T_{i,j,k}^n}{\rho C} - \frac{1}{2} \frac{h_w T_{i,j,k}^{n+1}}{\rho C} + S^{n+1/2},
\end{aligned} \tag{4.26}$$

where, Δx , Δy , and Δz are the step sizes in x , y , and z directions respectively. We rewrite Eq. (4.26) as follows so that only the term containing $T_{i,j,k}^{n+1}$ is kept at the left hand side,

$$\begin{aligned}
& T_{i,j,k}^{n+1} \left(1 + \frac{1}{2}\Delta t \frac{w_b C_b}{\rho C} + \frac{1}{2}\Delta t \frac{h_w}{\rho C} + \frac{\Delta t \alpha}{\Delta x^2} + \frac{\Delta t \alpha}{\Delta y^2} + \frac{\Delta t \alpha}{\Delta z^2} \right) = \\
& \frac{1}{2}\Delta t \alpha \left(\frac{T_{i+1,j,k}^{n+1} + T_{i-1,j,k}^{n+1}}{\Delta x^2} + \frac{T_{i,j+1,k}^{n+1} + T_{i,j-1,k}^{n+1}}{\Delta y^2} + \frac{T_{i,j,k+1}^{n+1} + T_{i,j,k-1}^{n+1}}{\Delta z^2} \right) \\
& + T_{i,j,k}^n \left(1 - \frac{1}{2}\Delta t \frac{w_b C_b}{\rho C} - \frac{1}{2}\Delta t \frac{h_w}{\rho C} - \frac{\Delta t \alpha}{\Delta x^2} - \frac{\Delta t \alpha}{\Delta y^2} - \frac{\Delta t \alpha}{\Delta z^2} \right) \\
& + \frac{1}{2}\Delta t \alpha \left(\frac{T_{i+1,j,k}^n + T_{i-1,j,k}^n}{\Delta x^2} + \frac{T_{i,j+1,k}^n + T_{i,j-1,k}^n}{\Delta y^2} + \frac{T_{i,j,k+1}^n + T_{i,j,k-1}^n}{\Delta z^2} \right) + S_{i,j,k}^{n+1/2} \Delta t,
\end{aligned} \tag{4.27}$$

where, $T_{i,j,k}^{n+1}$ is the unknown temperature at each grid point at the time level of $n + 1$. In Eq. (4.27), it is clear that the value inside the parentheses at the left hand side

is positive, and the first and third terms at the right hand side are also positive. Physically, the absolute temperature can not be negative, i.e., it is always required that $T_{i,j,k}^{n+1} \geq 0$. This condition can always be satisfied if the second term at the right hand side in Eq. (4.27) is not negative, which gives,

$$1 - \frac{1}{2}\Delta t \frac{w_b C_b}{\rho C} - \frac{1}{2}\Delta t \frac{h_w}{\rho C} - \frac{\Delta t \alpha}{\Delta x^2} - \frac{\Delta t \alpha}{\Delta y^2} - \frac{\Delta t \alpha}{\Delta z^2} \geq 0. \quad (4.28)$$

The desired time step size can be derived from Eq. (4.28) as

$$\Delta t \leq \frac{1}{\frac{1}{2} \frac{w_b C_b}{\rho C} + \frac{1}{2} \frac{h_w}{\rho C} + \frac{\alpha}{\Delta x^2} + \frac{\alpha}{\Delta y^2} + \frac{\alpha}{\Delta z^2}}. \quad (4.29)$$

The Crank-Nicolson scheme is second-order in accuracy spatially and temporally. However, in solving the transient bioheat transfer equation described in this chapter, the time step size cannot be chosen much larger than the criterion described by Eq. (4.29), otherwise unexpected numerical oscillation may be encountered.

4.6 Numerical Experiments and Discussions

In the 3-dimensional model, the thickness of each of the skin sub-layer is epidermis 8.0×10^{-5} m, dermis 0.002 m, and subcutaneous 0.01 m [120], as listed in Table 4.1. For the convenience of simulation, the area of interest on the skin surface is assumed to be a square, and the center of the square is exposed to a laser beam with an diameter of $\Phi = 5$ mm [1, 2]. The selected domain is symmetrical with regard to the planes at $y = 0$ and $z = 0$. So, actual computation is performed in only one fourth of the total volume, as shown in Fig. 4.1 [104] by computational domain, and the sizes of the computational domain in the y and z directions are $L = W = 0.015$ m. The material properties and parameters in Eq. (4.20) are shown in Table 4.1 [1, 120, 44]. The surrounding fluid temperature is chosen as the constant room temperature $T_f = 25^\circ\text{C}$ [54].

A total of $90 \times 50 \times 50$ grid intervals are used in the computation, where a uniform grid is used in each of the y and z directions with a mesh size of $\Delta y = \Delta z = 0.0003$

Table 4.1: Skin thickness and thermal physical properties used in this model.

Properties	Epidermis	Dermis	Subcutaneous	Blood
Thickness H (m)	8.0×10^{-5}	0.0020	0.010	
Thermal conductivity k (W/(mK))	0.25	0.50	0.20	
Density ρ (W/(mk))	1200	1200	1000	1060
Specific heat C (J/(kgK))	3600	3400	3000	3770
Blood perfusion rate w_b ($\text{m}^3/\text{s}/\text{m}^3\text{tissue}$)	0	0.00125	0.00125	
Absorption coefficient μ_a (mm^{-1})	80	2.4	1.0	
Initial water content W_0 (Kg/m^3)	780	780	780	

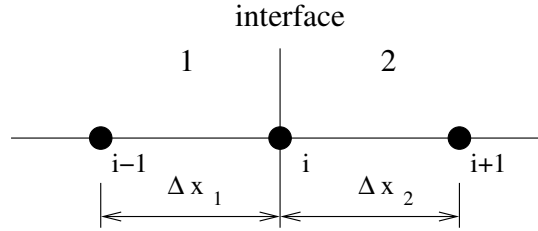


Figure 4.2: The interface between two different materials.

m. A non-uniform grid is used in the x direction. Specifically, the epidermis layer is uniformly divided into 10 intervals, the dermis and subcutaneous layers are uniformly divided into 40 intervals each. The resulting mesh size in the x direction is $\Delta x = 8 \times 10^{-6}$ m in epidermis layer, 5×10^{-5} m in dermis layer, and 2.5×10^{-4} m in subcutaneous layer. Because of the difference of material properties, two interfaces are formed among the three layers of the skin. On the interfaces, both the heat flux and temperature should be continuous. Without loss of generality, assuming there exists an interface between any two materials, i.e., material 1 and material 2, as shown in Fig. 4.2, the heat flux in materials 1 and 2 can be expressed by

$$q_1 = -k_1 \frac{dT}{dx} = -k_1 \frac{T_i - T_{i-1}}{\Delta x_1}, \quad (4.30)$$

and

$$q_2 = -k_2 \frac{dT}{dx} = -k_2 \frac{T_{i+1} - T_i}{\Delta x_2}, \quad (4.31)$$

respectively, where q_1 is the heat flux in material 1, k_1 the thermal conductivity of

material 1, q_2 the heat flux in material 2, k_2 the thermal conductivity of material 2. The heat flux through the interface can also be expressed by a second-order centralized finite difference as

$$q_i = -k_i \frac{dT}{dx} = -k_i \frac{T_{i+1} - T_{i-1}}{\Delta x_1 + \Delta x_2}, \quad (4.32)$$

where q_i is the heat flux through interface, k_i the thermal conductivity on the interface. Physically, the heat fluxes must satisfy $q_1 = q_2 = q_i$, and the thermal conductivity on the interface is consequently found as

$$k_i = \frac{k_1 k_2 (\Delta x_1 + \Delta x_2)}{k_1 \Delta x_2 + k_2 \Delta x_1}. \quad (4.33)$$

Other properties on the interface may be calculated as $C_i = (C_1 \Delta x_1 + C_2 \Delta x_2) / (\Delta x_1 + \Delta x_2)$, $\rho_i = (\rho_1 \Delta x_1 + \rho_2 \Delta x_2) / (\Delta x_1 + \Delta x_2)$, and $w_{bi} = (w_{b1} \Delta x_1 + w_{b2} \Delta x_2) / (\Delta x_1 + \Delta x_2)$. Eq. (5.9) is complete after we find the properties on the interfaces. The number of unknowns is 213,689 in the resulting linear system, and the corresponding number of nonzeros in the coefficient matrix is 1,473,577.

It is assumed that the skin under investigation is subject to laser heating every 0.1 s with a duration of 0.005 s for 2 s, which corresponds to $i = 20$, $P = 0.1$ s, and $\kappa = 5$ % in Eq. (4.4). The time step is chosen as $\Delta t = 0.001$ s, so that the laser heating is complete in 5 time steps in each period. The selection of Δt is contingent on Eq. (4.29). In this particular case, the dominant term is $\alpha / \Delta x^2$ due to the small mesh size in the x direction. So, the time step size may be approximated as $\Delta t \approx \Delta x^2 / \alpha \approx 0.0011$ s.

3D temperature distribution of skin subject to a pulsed laser-heating under the consideration of water evaporation and diffusion is presented in the form of contour plot and shown in Fig. 4.3, where the blue color indicates the interface between epidermis and dermis layers, and the green color indicates the interface between dermis and subcutaneous layers [104]. Note, in order to display the results in a better way, only part of them, i.e., $0 \leq y \leq 0.005$ m and $0 \leq z \leq 0.005$ m is shown in Fig. 4.3.

Figure 4.3(a) shows the mesh arrangement. A uniform mesh is used in the y and z space directions, while a non-uniform one is applied in the x direction, with coarse grid near the body core and fine grid near the skin surface. Figure 4.3(b) shows the contour plot of temperature distribution in the computational domain when the skin surface is exposed to the pulsed laser-heating for 2 s. The parameters of the Gaussian shaped laser beam corresponding to Eq. (4.2) are $P = 12$ W, $W = 0.0025$ m, and $\mu_a = 80, 2.4,$ and 1 mm^{-1} in the epidermis, dermis and subcutaneous regions respectively. As expected, an axisymmetrical temperature profile is obtained due to the laser source in Gaussian distribution and the highest temperature is near the center of the region where it is heated. Figures 4.3(c) and 4.3(d) use the same data as Figure 4.3(b) but are viewed from different angles. Figure 4.3(c) is the side view from which how deep the skin is affected by laser-heating can be seen clearly. Figure 4.3(d) is an anatomical view of the temperature variation from which the temperature distribution on the three adjacent orthogonal planes is clearly shown. These three figures together give good general presentation of the skin tissue thermal response to which part, how large the area, and what extent the skin is affected by the specific heating [104].

The 3D plot in Fig. 4.3 only shows temperature value at the fixed time $t = 2$ s with water evaporation and diffusion. However, the effect of water transport on and the temperature history with time are not shown. These aspects are exhibited in the next three figures. Figure 4.4 shows the temperature variation along the center line ($y = z = 0$) of the computational domain at $t = 2$ s. It is obvious that the temperature near the skin surface is reduced in a big margin by considering the cooling effect of water evaporation and diffusion. It is interesting to note that the predicted highest temperature is not on the skin surface but somewhere near the interface between the epidermis and dermis after considering the cooling effect of water transport. Even though the laser irradiance is axially attenuated by Beer's

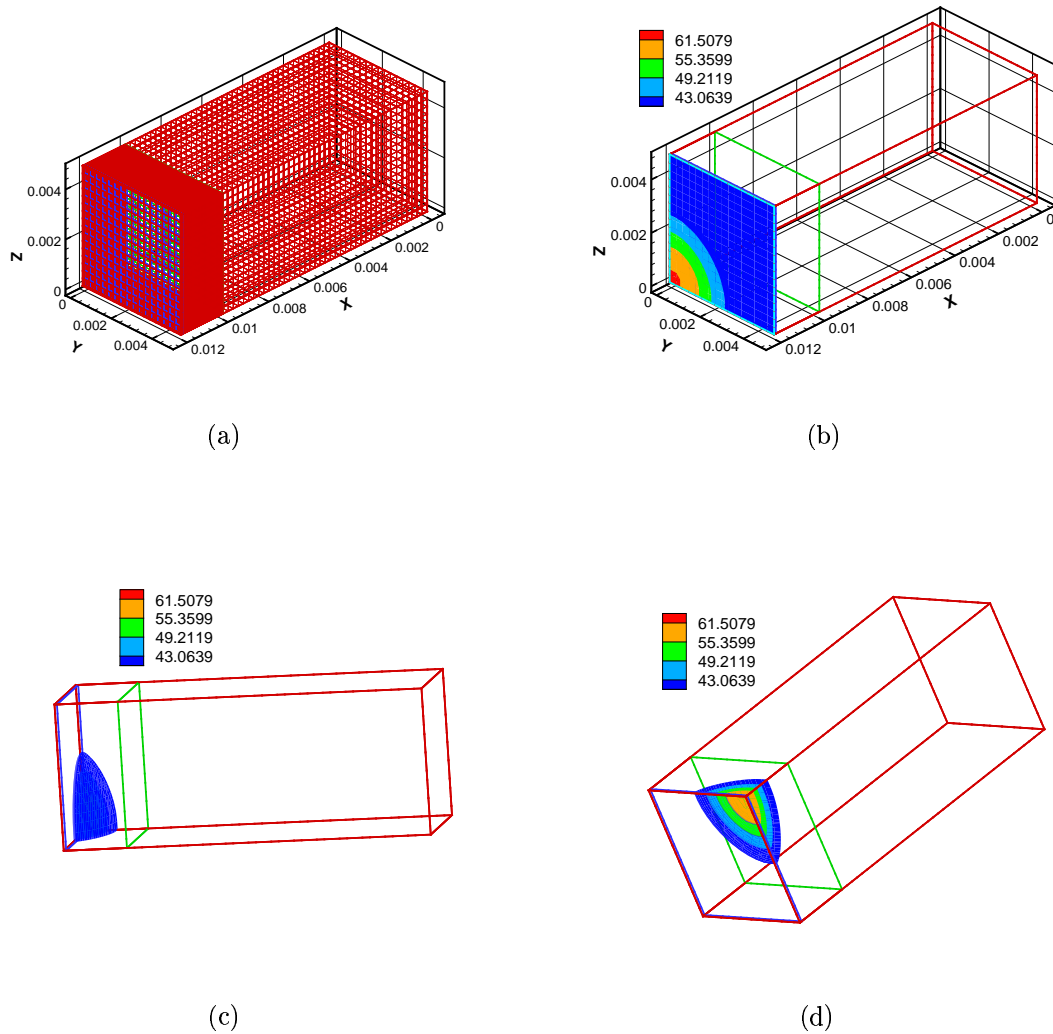


Figure 4.3: 3D temperature distribution of the skin subject to laser-heating with Gaussian profile at $t = 2$ s. (a) The mesh of the computational domain, uniform in the y and z directions, non-uniform in the x direction. (b) Contour plot of temperature viewed from the skin surface ($y - z$ plane at $x = 0.01208$ m). (c) Contour plot of temperature viewed from one side ($x - z$ plane at $y = 0.005$ m) of the computational domain. (d) Contour plot of temperature viewed anatomically (starting from the point $x = 0.01208$ m, $y = 0$ m, and $z = 0$ m to view the temperature distribution on the three adjacent orthogonal planes). The grids and scales are on in (a) and (b) but off in (c) and (d). The boundaries of computational domain are plotted in red. The blue color indicates the interface between epidermis and dermis, and the green color indicates the interface between dermis and subcutaneous. The parameters of the Gaussian shaped laser beam corresponding to Eq. (4.2) are $P = 12$ W, $W = 0.0025$ m, and $\mu_a = 80, 2.4,$ and 1 mm^{-1} in the epidermis, dermis and subcutaneous layers respectively.

law [44], a large portion of the heat is removed by water evaporation on the skin surface, consequently temperature near the skin surface is lower than that of its inner neighbors. Also the location where the highest temperature appears is changing with time [104].

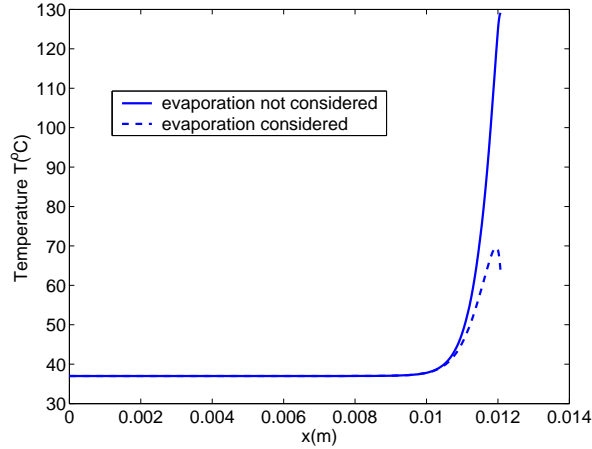


Figure 4.4: The temperature change as a function of skin depth with/without evaporation.

The change of temperature with time on the skin surface is studied for both cases considering and not considering water transport to demonstrate the influence of water evaporation and diffusion on the skin thermal response in another way. In particular, the temperature history at the center point of the heated region ($x = 0.01208$ m, $y = z = 0$ m) is plotted in Fig. 4.5. As expected, twenty periods are shown in the figure, with a beginning of sharp temperature increase and an ending of gradual temperature decrease. In Fig. 4.5(a) the temperature decrease is caused by the convective boundary condition, which is specified as $h_f = 20$ W/(m²°C) and $T_f = 25$ °C, while in Fig. 4.5(b) the decrease is made by both the same convective boundary condition as that in Fig. 4.5(a) and water evaporation and diffusion. When water transport is not considered, skin temperature increases continuously with periodic laser-heating and the peak temperature can go as high as about 160°C. On the other hand, when water transport is considered, skin temperature increases gradually in the

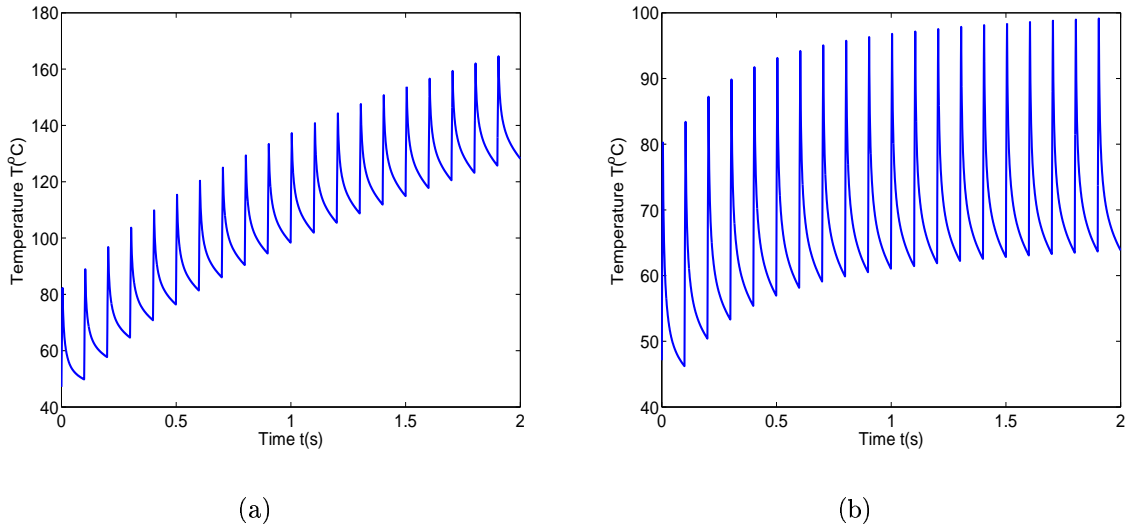


Figure 4.5: The temperature history in the center of the heated region on the skin surface which is subject to periodic pulsed laser-heating for the time duration from 0 to 2 s. (a) Water evaporation and diffusion are not considered. (b) Water evaporation and diffusion are considered.

first a few heating periods, then the rate of temperature increase slows down after the temperature reaches a certain value, and the peak temperature is only about 100°C.

Temperature on the skin surface rises due to laser-heating, so the vapor pressure near the skin surface is higher than that in the surrounding air. Due to the difference of water vapor pressure, molecular water evaporates from the skin surface to atmosphere. Consequently water content, sometimes called water density in this thesis, near the skin surface is lower than that in the deep layers, thereafter liquid water starts diffusing from inner layers toward skin surface. In the simulation, the initial water content is assumed to be uniform in all the three layers of skin as $780,000 \text{ g/m}^3$. Figure 4.6 presents the variation of water content in skin which is exposed to laser-heating. As already shown is Fig. 4.3 that the resulting temperature distribution on the skin surface is axisymmetric, the resulting water content distribution on the skin surface is axisymmetric too, see Fig. 4.6(a). It is clear that the higher the temperature the faster the rate of water evaporation on skin surface. This can also be observed in Fig. 4.6(b), where the evolution of water content in the center point of the heated

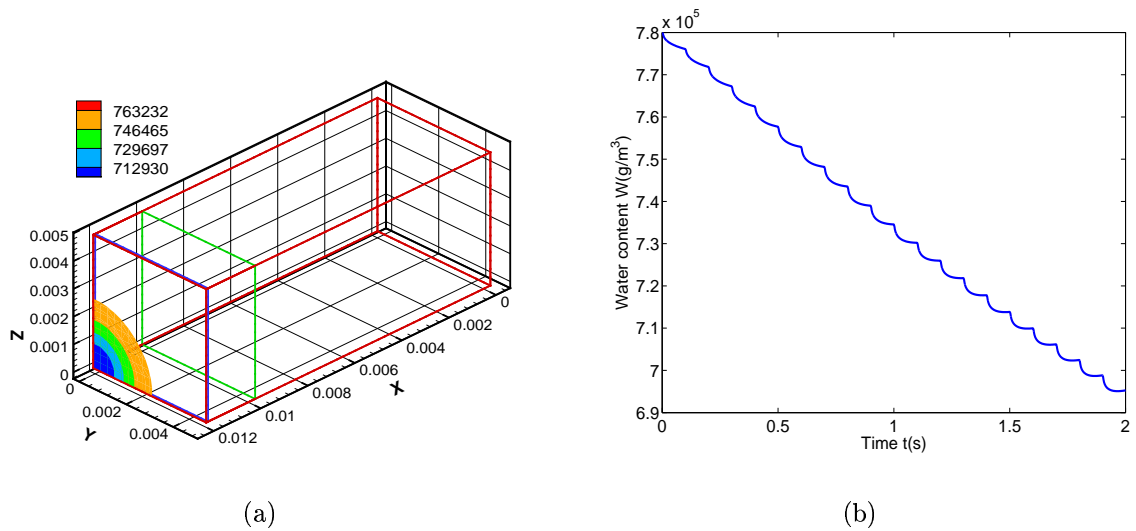


Figure 4.6: Water transport in skin due to temperature rise caused by periodic pulsed laser-heating for the time duration from 0 to 2 s. (a) The distribution of water content in skin in three-dimension. (b) Water content as a function of time at the point of $x = 0.01208$ m, $y = z = 0$ m.

region on skin surface is exhibited. Considering the slope to the curve expressing water content as a function of time, larger ones are seen at the beginning phase and smaller ones at the ending phase in each of the twenty periods of laser-heating [104].

Another observation is that temperature increase and water content decrease in skin tissue are not symmetric, as shown in Fig. 4.7. To be clear, the heat diffuses faster than the water in skin. For the same duration of 2 s, as deep as 0.003 m of skin has witnessed temperature change, as can be seen in Fig. 4.7(a). On the contrary, only as thin as 0.0001 m of skin is affected with water content, shown in Fig. 4.7(b). This may be explained by some of the skin physical properties. According to some references [2, 115, 120], the thermal diffusivity in skin can be calculated as ($\alpha \approx 10^{-8} \sim 10^{-7}$ m²/s), which is about two to three orders of magnitude larger than the water diffusion coefficient ($D = 5 \times 10^{-10}$ m²/s) [27, 70, 97].

Cryogen spray cooling (CSC) is an efficient tool to cool upper layers of skin during laser therapy [2]. However, we will not discuss the application of CSC to some

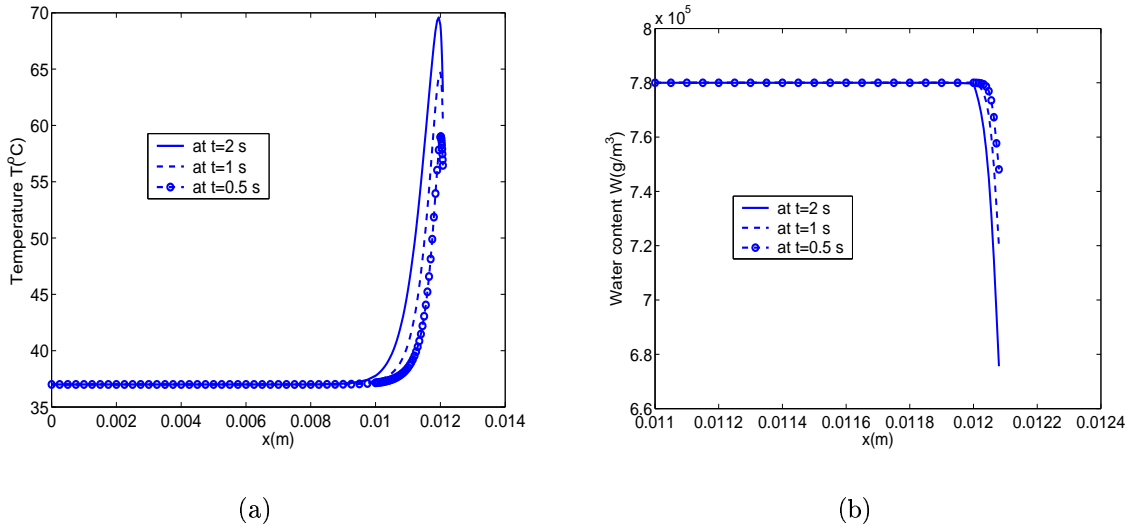
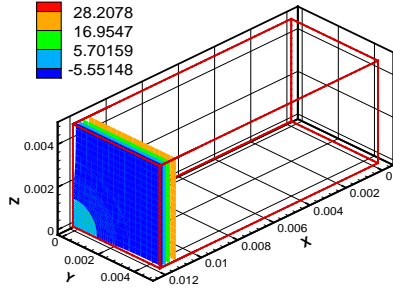
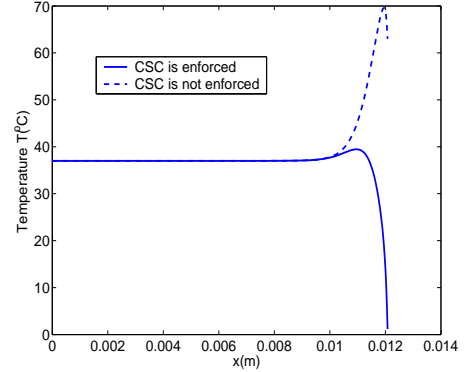


Figure 4.7: Temperature and water content as a function of x along the center line ($y = z = 0$ m) at different time. (a) Temperature distribution. (b) Water content distribution.

particular surgeries such as port wine stain laser therapy, but the general thermal response of skin when CSC is used in the case of laser-heating. The effect of CSC can be evaluated by regarding it as a form of convection with a large convective heat transfer coefficient h ($\text{W}/(\text{m}^2\text{C})$) and a coolant with low temperature T_f ($^{\circ}\text{C}$). According to published resources, the value of h is ranged from 1,000 to 100,000 $\text{W}/(\text{m}^2\text{C})$ [2, 126]. In our simulation, the convective heat transfer coefficient is chosen as $h = 2,000$ $\text{W}/(\text{m}^2\text{C})$, and the cooling temperature is chosen as $T_f = -26$ $^{\circ}\text{C}$, which is the boiling temperature of liquid cryogen tetrafluoroethane, R-134a [1]. The result is plotted in Fig. 4.8. Figure 4.8(a) shows 3D temperature distribution in skin, and Fig. 4.8(b) is about the temperature variation as a function of x . As expected the upper part of skin is deeply cooled, and the inner part is less affected. Results with and without CSC is compared. Without losing generality, temperature along the center line ($y = z = 0$ m) is plotted in Fig. 4.8(b), where the solid line indicates the case that CSC is enforced, and the dashed line indicates the case that CSC is not enforced but water evaporation and diffusion are considered. Since the temperature



(a)



(b)

Figure 4.8: The thermal response of skin due to laser-heating when cryogen spray cooling is considered. (a) 3D temperature distribution. (b) Temperature variation as a function of x .

on the skin surface is much lower than normal body temperature, water evaporation and diffusion may not need to be considered in modeling the thermal response of laser heating when CSC is enforced. In fact, in the case of CSC, the skin temperature may be even lower than the surrounding air temperature, thus possibly water may condense on the skin surface [104].

4.7 Summary

A 3D multilayer model is proposed to investigate the transient thermal response of skin subject to laser heating, and the impact of water evaporation and diffusion on skin temperature evolution is also included based on the laminar boundary-layer theory, which is used to determine the rate of water evaporation.

Both the time-dependent heat transfer equation and water transport equation are discretized using the Crank-Nicolson scheme by a 7 point standard centralized finite difference approximation. The stability of the numerical scheme is analyzed in terms of physical requirement and a desired time step which guarantees a physically mean-

ingful result is suggested. The resulting linear system is sparse and solved iteratively with one of the fastest linear system solvers GMRES.

Based on the simulation results, skin temperature is significantly reduced when water evaporation and diffusion are considered, especially in the upper part of the skin, and the temperature on the skin surface is even lower than some inner part of the skin. Thus, water transport moves a considerable amount of heat energy away from the skin, plays an important role in skin temperature evolution, and needs to be considered in modeling skin thermal response when external cooling is not used.

The cryogen spray cooling in laser surgery is modeled as well. It is found that if cryogen spray is used to cool the skin under laser surgery, the temperature near the skin surface is reduced much lower than normal due to the large convective heat transfer coefficient and the low temperature of cryogen, and the influence of water evaporation and diffusion may not be strong enough to be meaningfully considered.

The examples studied in the chapter are short-duration periodic high strength laser source. In fact, the model can be used for any type of heating by simply modifying the time function and using the actual form of heating source.

5 Thermal Injury Prediction with Strain Energy

5.1 Introduction

Skin performs a vital role in regulating the temperature of human body by serving as the medium of heat transfer between the body and the environment. To be specific, skin is composed of three layers: epidermis, dermis, and subcutaneous. Epidermis is the outermost layer consisting of dead cells on the outermost level and deratinocytes on the deepest level. Right beneath epidermis is the dermis layer, which consists of blood vessels, elastic fibers, connective tissues, sweat glands, and nerves [80]. The next layer is subcutaneous that contains larger blood vessels [73]. Blood flow is essential in providing nutrients to dermis and subcutaneous and maintaining energy exchange between skin and the inner parts. However, there are no blood vessels in epidermis layer, and the corresponding heat and mass transport processes are conducted by diffusion between dermis and epidermis.

Under normal conditions, thermal balance between human body and the environment can be maintained and skin is at a comfortable temperature suitable for its metabolic function [80]. Physiological abnormality or changes of environmental conditions could influence the temperature distribution in skin and may even disturb the existing thermal balance in human body. Skin burn is one of such cases in which human body is exposed to high temperature or high heat flux environmental condition for a certain period of time, hence local skin temperature is raised high enough to destroy the organic tissue and to cause injury.

Burn injury is one of the most common accidental injuries in human daily activities. According to some statistics, hundreds of thousands of people suffer from burn injuries in the United States every year [95]. In 1999, the occupational injuries of firefighters alone were as many as 88,500 in the United States [88]. The severity of burn injury varies from minor damage in skin superficial layer to severe damage in

deeper layers to even fatality. Skin burn injury may be classified based on skin physical structure as first degree with partial damage of epidermis, second degree with total damage of epidermis and partial damage of dermis, and third degree with total damage of epidermis, dermis, and partial damage of subcutaneous. It is important to provide a quantitative connection between the surrounding thermal environmental condition and the degree of burn injury. Conducting such experiments directly to collect data from human beings may not be feasible. On the contrary, computer simulation using data from other biological bodies such as animals may be practical.

Current skin thermal injury model proposed by Henriques and Moritz [46, 73] is based on the chemical process of protein denaturation. Skin endures thermal stress and deformation due to temperature variation. Consequently strain energy may play a role in further damage of skin. The aim of this work is to investigate the effect of strain energy on skin thermal injury. In particular, a three-dimensional (3D) numerical model is developed to predict the transient temperature distribution in skin tissues with the consideration of water evaporation on the skin surface and water diffusion in the tissue. Thermal stress and deformation of skin is modeled using Duhamel-Neuman equation, strain energy is then obtained by the stress-strain relation, and skin thermal injury is evaluated based on the proposed model including strain energy. Finite difference method is used to discretize the 3D PDEs, and the resulting linear systems are solved iteratively.

5.2 Thermal Stress and Deformation

One of the destructive mechanisms for thermal damage of soft tissue is thermal induced high mechanical stress. To study the thermal induced deformation in soft tissues at high temperature, the thermoporoelasticity model is used in which stress, strain, and temperature are related. The constitutive relation describing the elastic

deformation of the soft tissue may be expressed as [136]

$$\begin{bmatrix} \sigma_{xx} \\ \sigma_{yy} \\ \sigma_{zz} \\ \tau_{xy} \\ \tau_{xz} \\ \tau_{yz} \end{bmatrix} = \begin{bmatrix} c_{11} & c_{12} & c_{13} & 0 & 0 & 0 \\ c_{21} & c_{22} & c_{23} & 0 & 0 & 0 \\ c_{31} & c_{32} & c_{33} & 0 & 0 & 0 \\ 0 & 0 & 0 & c_{44} & 0 & 0 \\ 0 & 0 & 0 & 0 & c_{55} & 0 \\ 0 & 0 & 0 & 0 & 0 & c_{66} \end{bmatrix} \begin{bmatrix} \varepsilon_{xx} \\ \varepsilon_{yy} \\ \varepsilon_{zz} \\ \gamma_{xy} \\ \gamma_{xz} \\ \gamma_{yz} \end{bmatrix} - \begin{bmatrix} \beta \\ \beta \\ \beta \\ 0 \\ 0 \\ 0 \end{bmatrix} [\theta], \quad (5.1)$$

where σ is the normal stress, τ the shear stress, ε the normal strain, γ the shear strain, and θ the temperature difference. The coefficients in Eq. (5.1) are [14]

$$\begin{aligned} c_{11} = c_{22} = c_{33} &= \frac{1 - \nu}{(1 - 2\nu)(1 + \nu)}, \\ c_{12} = c_{21} = c_{13} = c_{31} = c_{23} = c_{32} &= \frac{\nu}{(1 - 2\nu)(1 + \nu)}, \\ c_{44} = c_{55} = c_{66} &= \frac{\nu}{2(1 + \nu)}, \end{aligned}$$

and

$$\beta = \frac{E\alpha}{1 - 2\nu}.$$

Other symbols in Eq. (5.1) are E Young's modulus, ν Poisson's ratio, and α thermal expansion coefficient. Strain is related to deformation by the following expression,

$$\begin{bmatrix} \varepsilon_{xx} \\ \varepsilon_{yy} \\ \varepsilon_{zz} \\ \gamma_{xy} \\ \gamma_{xz} \\ \gamma_{yz} \end{bmatrix} = \begin{bmatrix} \frac{\partial}{\partial x} & 0 & 0 \\ 0 & \frac{\partial}{\partial y} & 0 \\ 0 & 0 & \frac{\partial}{\partial z} \\ \frac{\partial}{\partial y} & \frac{\partial}{\partial x} & 0 \\ \frac{\partial}{\partial z} & 0 & \frac{\partial}{\partial x} \\ 0 & \frac{\partial}{\partial z} & \frac{\partial}{\partial y} \end{bmatrix} \begin{bmatrix} u_1 \\ u_2 \\ u_3 \end{bmatrix}, \quad (5.2)$$

where, u_1 , u_2 , and u_3 are displacements in x , y , and z directions respectively. From Eqs. (5.1) and (5.2), the following equilibrium equation is obtained,

$$G \sum_{j=1}^3 \left(\frac{\partial^2 u_i}{\partial x_j^2} + \frac{1}{1 - 2\nu} \frac{\partial^2 u_j}{\partial x_j \partial x_i} \right) + \beta \nabla \theta_i = 0, \quad (5.3)$$

where u is the displacement vector, and G is the shear modulus given by

$$G = \frac{E}{2(1 + \nu)}.$$

The thermal induced stress has been investigated and discussed in [101], here we focus on the deformation energy and its effect on skin thermal injury. After obtaining the stress and strain tensors, the unit strain energy can be computed according to the following expression,

$$E_{mech} = \frac{1}{2}V [\sigma_{xx} \ \sigma_{yy} \ \sigma_{zz} \ \tau_{xy} \ \tau_{xz} \ \tau_{yz}] \begin{bmatrix} \varepsilon_{xx} \\ \varepsilon_{yy} \\ \varepsilon_{zz} \\ \gamma_{xy} \\ \gamma_{xz} \\ \gamma_{yz} \end{bmatrix}, \quad (5.4)$$

in which V is the molar volume of skin tissue.

5.3 Thermal Injury Prediction

A quantitative description of skin thermal damage due to high temperature exposure, suggested by Henriques and Moritz [46, 73], is the following

$$\frac{\partial \Omega}{\partial t} = \zeta \exp \left(-\frac{\Delta E}{RT(x, t)} \right), \quad (5.5)$$

where ζ is the pre-exponential factor, ΔE is the activation energy for the reaction, and R is the gas constant. The temperature is determined by Eq. (3.1) and the environmental conditions. The constants and parameters used in this model are: at the epidermis layer, $\zeta = 3.1 \times 10^{98}$ (s⁻¹), $\Delta E = 627.9$ (kJ/mol); at the dermis layer, $\zeta = 4.32 \times 10^{64}$ (s⁻¹), $\Delta E = 418.6$ (kJ/mol) for temperature $44 \leq T \leq 55$ °C, and $\zeta = 9.39 \times 10^{104}$ (s⁻¹), $\Delta E = 669.8$ (kJ/mol) for temperature $T \geq 55$ °C [120, 130]. Integrating Eq. (5.5) over the period of burn, the total accrual of thermal injury as a function of position within the tissue is

$$\Omega = \zeta \int_0^t \exp \left(-\frac{\Delta E}{RT(x, t)} \right) dt. \quad (5.6)$$

In the case of skin burn, soft tissues are subject to thermal stress, which may cause possible tissue deformation. Intuitively, tissue may be more easily damaged under such a condition. That is, tissue protein denaturation may happen at relatively small

activation energy E in Eq. (5.6). Therefore we propose the following integral equation to estimate the local accrual of thermal injury

$$\Omega = \zeta \int_0^t \exp\left(-\frac{\Delta E - E_{mech}}{RT(x, t)}\right) dt, \quad (5.7)$$

where E_{mech} is the mechanical energy defined by Eq. (5.4).

5.4 Numerical Algorithm and Solution Procedure

According to the proposed model for predicting skin burn injury, Eqs. (3.1), (4.14), (5.3), and (5.7) have to be solved at the same time. The corresponding algorithm is listed below.

-
- 1: Set $t := 0, n := 0$
 - 2: Assign initial values to $T^{(0)}, w^{(0)}, u^{(0)}, \Omega^{(0)}$
 - 3: Initialize values at level n : $T^{(n)} \leftarrow T^{(0)}, w^{(n)} \leftarrow w^{(0)}, u^{(n)} \leftarrow u^{(0)}, \Omega^{(n)} \leftarrow \Omega^{(0)}$
 - 4: **while** $t < t_{end}$ **do**
 - 5: Solve Eq. (3.1) iteratively for $T^{(n+1)}$
 - 6: Solve Eq. (4.14) iteratively for $w^{(n+1)}$
 - 7: Solve Eq. (5.3) iteratively for $\vec{u}^{(n+1)}$
 - 8: Compute stress and strain tensors from Eqs. (5.1) and (5.2)
 - 9: Compute unit strain energy from Eq. (5.4)
 - 10: Compute the accrual of thermal injury from Eq. (5.7)
 - 11: Assign values as: $T^{(n)} \leftarrow T^{(n+1)}, w^{(n)} \leftarrow w^{(n+1)}, \vec{u}^{(n)} \leftarrow \vec{u}^{(n+1)}, \Omega^{(n)} \leftarrow \Omega^{(n+1)}$
 $t := t + \Delta t$
 - 12: **end while**
-

In the above algorithm both Eqs. (3.1) and (4.14) are discretized using Crank-Nicholson finite difference scheme. Eq. (5.3) is not time dependent and is discretized using a second order 19 point finite difference scheme. Using Eq. (3.1) as an example, the following expression can be derived,

$$\frac{T^{n+1} - T^n}{\Delta t} = \frac{1}{2}\alpha\mathcal{A}T^{n+1} + \frac{1}{2}\alpha\mathcal{A}T^n + S^{n+1/2}. \quad (5.8)$$

Here Δt is the time step, \mathcal{A} the finite difference approximation of the elliptic operator, and S the source term. The truncation error of the scheme is of order $\mathcal{O}(\Delta t^2 + h^2)$.

Eq. (5.8) may be written in a matrix form as,

$$\left(I - \frac{\alpha\Delta t}{2}\mathcal{A}\right)T^{n+1} = \left(I + \frac{\alpha\Delta t}{2}\mathcal{A}\right)T^n + \alpha\Delta tS^{n+1/2}. \quad (5.9)$$

For each of Eqs. (3.1), (4.14) and (5.3), a sparse linear system, denoted by $Ax = b$, can be obtained from the discretization. They are solved iteratively using the fast iterative solver GMRES, accompanied with an ILUT preconditioner [93]. Note, in the GMRES method, the required storage grows quadratically with the number of iterations. So the number of iterations should be confined to not a big one. Practically, A restarted version of GMRES is employed as GMRES(10), where 10 is the dimension of the Krylov subspace, so that GMRES is restarted after 10 iterations. An incomplete LU factorization with a dual dropping threshold (ILUT) is used to speed up the convergence rate of GMRES. The ILUT preconditioner makes use of a dual dropping strategy that is represented by two parameters p and τ , where p is the number of fill-in elements, and τ is the dropping tolerance. In our computation, we used $p = 40$ and $\tau = 10^{-4}$. Instead of the original linear system $Ax = b$, an equivalent one $M^{-1}Ax = M^{-1}b$ is solved in the preconditioned iterations, where M is the ILUT preconditioner. More information about the GMRES solver and the ILUT preconditioner can be found in [94].

5.5 Numerical Experiments and Discussions

A 3D view of the skin structure is depicted in Fig. 4.1, where from the top to the bottom, each layer is shown as the epidermis, the dermis, and the subcutaneous in order. As can be seen in Table 4.1, the thickness of each layer is epidermis 8.0×10^{-5} m, dermis 0.002 m, and subcutaneous 0.01 m [120]. For the convenience of simulation, the area of interest on the skin surface is assumed to be a square with a dimension of $L = W = 0.015$ m. One of our major interests for conducting this research is to investigate the instant thermal mechanical response in each of the three skin physical layers and evaluate the degree of burn injury. Due to the extreme thin thickness of

the epidermis layer, uniform grid may not be appropriate. The grid points are hence distributed as 10 intervals in the epidermis layer, 40 intervals in each of the dermis and subcutaneous layers, which gives a mesh size in the x direction as $\Delta x = 8 \times 10^{-6}$ m in the epidermis layer, $\Delta x = 5 \times 10^{-5}$ m in the dermis layer, and $\Delta x = 2.5 \times 10^{-4}$ m in the subcutaneous layer, as listed in Table 4.1. Along the y and z directions, equally spaced 50 intervals are assigned. That gives a mesh size of $\Delta y = \Delta z = 0.0003$ m. Such a small Δx puts a constraint on the determination of time step Δt , which is chosen as $\Delta t = 0.001$ s. The criterion for determining Δt is presented in the previous chapter. With this arrangement, a total of $90 \times 50 \times 50$ grid intervals are resulted. The number of unknowns resulting from discretizing Eqs. (3.1) and (4.14) is therefore 213,689 each, and the corresponding number of nonzeros in the coefficient matrix is 1,473,577. Since there are 3 components at each grid points, a discretization of Eq. (5.3) gives 641,067 unknowns.

This work differs from others [27, 75, 120, 130] in predicting skin thermal injury by including the effect of mechanical energy resulting from thermal induced stress and deformation, and interpreting the tissue damage as stages of mechanical response and chemical reaction. In the stage of mechanical response, soft tissue is under thermal stress and has deformation energy, which can further affect the ongoing chemical reaction process by possibly lowering the activation energy. The model is general in simulating various thermal burning processes of biological tissue by easily modifying the heat source term in Eq. (3.1). Using this skin burn model, a few numerical experiments have been conducted, including laser therapy, flash light, and steam burn, which are discussed below.

Laser Therapy As a means of treatment to dermatological patients, laser therapy has been widely used due to its apparent advantages over conventional surgeries [119]. As an example, dye lasers can be used to selectively damage some microvasculature in human skin [4]. Laser therapy, however, may cause possible side effects

and complications because of unintentional heating of the adjacent healthy tissues. This example studies the tissue damage of laser type heat source exposure. The heat transfer due to laser heating may be approximated by a Gaussian type heat source, as shown in Eqs. (4.2) and (4.3). It is assumed that skin under investigation is subject to laser heating every 0.1 s with a duration of 0.005 s, and the time step is chosen as $\Delta t = 0.001$ s. The parameters of the Gaussian shaped laser beam corresponding to Eq. (4.2) are $P = 12$ W, $W = 0.0025$ m, and $\mu_a = 80, 2.4,$ and 1 mm^{-1} in the epidermis, dermis and subcutaneous regions respectively.

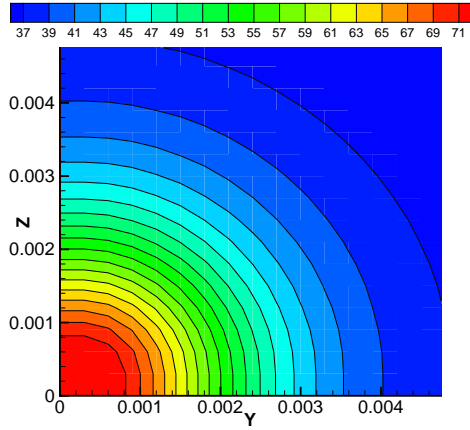
Skin damage occurs when the temperature at the base of the epidermis layer reaches above 44°C . The rate of burn injury is said to be second degree if the accumulated integral of Ω is greater than 1. A burn injury is third degree if the temperature at the base of the dermis layer reaches above 44°C and the accumulated integral of Ω is more than 1 [46, 120]. The thermal response of skin subject to laser exposure is shown in Fig. 5.1. Fig. 5.1(a) is the temperature distribution at the base of epidermis layer for a period of 50 s. Fig. 5.1(b) is the consequent strain energy due to tissue deformation. Figs. 5.1(c) and 5.1(d) are the corresponding results of the accrual damage without and with the consideration of the mechanical energy. It can be seen that after 50 s the damage contour of Ω with level 1 is at $r \leq 0.0021$ m when the mechanical energy is not considered and at $r \leq 0.0022$ m when the mechanical energy is considered. That is to say that for the same laser power and exposure time, more area is subject to the second degree burn when the mechanical energy is considered. In other words, less time is needed for the second degree burn. Fig. 5.2(a) is the contour plot of the accrual damage at the base of the dermis layer for an exposure time of 200 s. The threshold of the third degree burn, the damage contour with level 1, is at the location of $r_0 = 0.001$ m when the mechanical energy is not considered. It is at the location of $r_0 = 0.0012$ m when the mechanical energy is considered. Any place inside the circle of $r = r_0$ is considered to have a third degree

burn. It can be found by a comparison between Figs. 5.1 and 5.2 that an inclusion of the mechanical damage affects more for the third degree burn prediction than for the second degree one. This may be partially due to the relatively small value of the activation energy ΔE in Eq. (5.7) in calculating the accrual damage of the dermis layer for temperatures of $44 \leq T \leq 55$ °C.

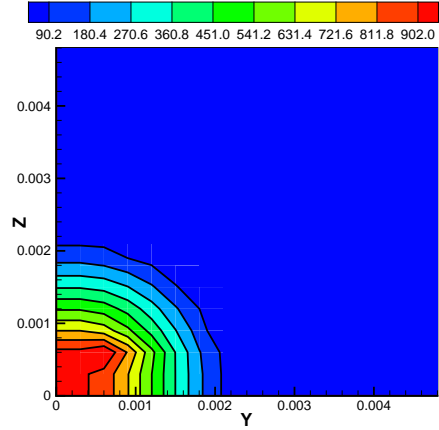
It can be seen from Fig 5.1(b) that in this particular case the calculated strain energy is less than $1,000\text{J}/\text{cm}^3$, which is small compared with the activation energy ΔE in Eq. (5.7). The strain energy can be large, however, in certain circumstances. It is observed from Eq. (3.1) that the tissue temperature is related to the parameters of $\alpha_1 = k/(\rho C)$, $\alpha_2 = w_b C_b (T_a - T)/(\rho C)$, and $\alpha_3 = Q/(\rho C)$, where α_1 , α_2 , and α_3 denote the effects of thermal properties, blood flow, and external heat source on temperature variation respectively. In most skin burn injury cases, the influence of α_2 may be negligible due to its relative small quantity compared with α_3 . Since the skin thermal properties are assumed to be constant, the temperature distribution is solely determined by the external heat flux. It is assumed that mechanical properties are constant as well, then tissue displacement is solely determined by the temperature derivatives, as shown in Eq. (5.3). Thus if the external heat source α_3 is extremely large, a large temperature derivative will result, which leads to large tissue displacement, stress and strain tensors, and mechanical energy. Consequently, the influence of mechanical deformation on tissue damage may be significant.

Note, in order to display the results more clearly, only part of them, i.e., $0 \leq y \leq 0.005$ m and $0 \leq z \leq 0.005$ m, is shown in Figs. 5.1 and 5.2(a), and the accumulated damage Ω is scaled to Ω' by $\Omega' = 1 + \lg \Omega$.

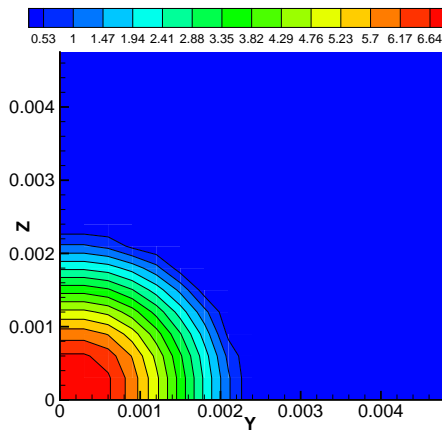
Flash Fire Flash fire can be simulated using the current model by modifying Eq. (3.1). The body exposure to flash fire is assumed to be uniformly distributed, so the problem can be treated as one-dimensional. This can be achieved by specifying symmetric boundary conditions along the border of the region under investigation, i.e., y and z



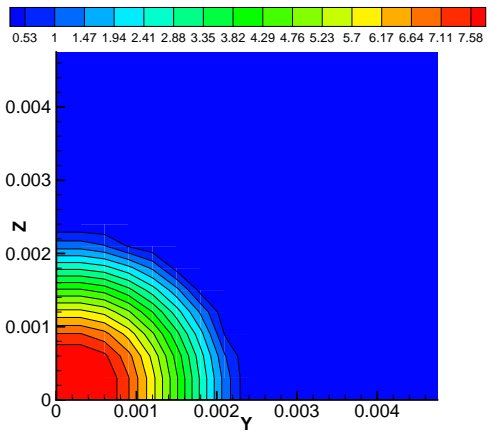
(a)



(b)



(c)



(d)

Figure 5.1: Two-dimensional temperature and accumulated damage plots for laser heating with a Gaussian profile. (a) Temperature ($^{\circ}\text{C}$) distribution at the base of the epidermis layer after 50 s. (b) The contour of mechanical energy (J/cm^3) at the base of the epidermis layer after 50 s. (c) The contour of accumulated damage at the base of the epidermis layer after 50 s without the consideration of mechanical energy. (d) The contour of accumulated damage at the base of the epidermis layer after 50 s with the consideration of mechanical energy. Note: in Figs. 5.1(c) and 5.1(d) the accumulated damage is scaled to $\Omega' = 1 + \lg \Omega$.

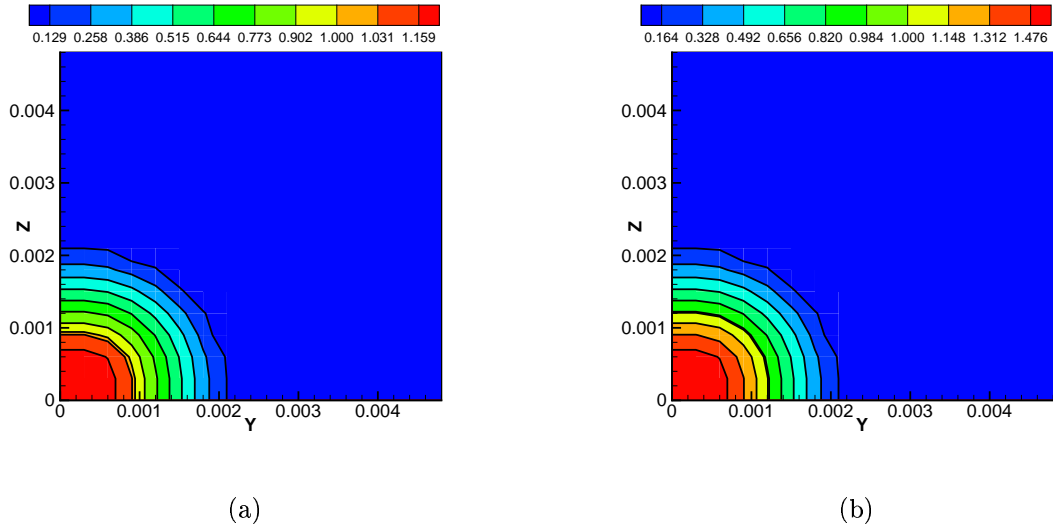


Figure 5.2: Contour plot of accumulated damage at the base of the dermis layer after 200 s. (a) Mechanical energy is not considered (b) Mechanical energy is considered. Note: the accumulated damage is scaled to $\Omega' = 1 + \lg \Omega$.

directions, and uniform heat flux on the skin surface. The current model is used to predict the time to second degree burn for a number of exposures with the intense heat flux ranging from 4.186kW/m^2 to 41.86kW/m^2 . This can be achieved easily by modifying the local heat source in Eq. (3.1) as $Q_r = C$, where C is a constant corresponding to the actual heat fluxes being tested. It can be seen from Fig. 5.3 that the present results agree well with the published ones [120]. The predicted time to the second degree burn falls between the experimental data given by Stoll and Greene [113] and the closed form solution provided in [45]. For the same exposure intensity, our results predict more time than the finite element model by Torvi and Dale [120]. This may be due to the fact that water transport is considered in our model, which removes some of the incoming thermal energy and tends to decrease the degree of thermal damage.

Steam Burn As an example, steam burn is also studied. The physical process differs for different type of burns. Laser burn and flash burn have the same nature of relatively high pressure on the skin surface and possible water evaporation and diffusion

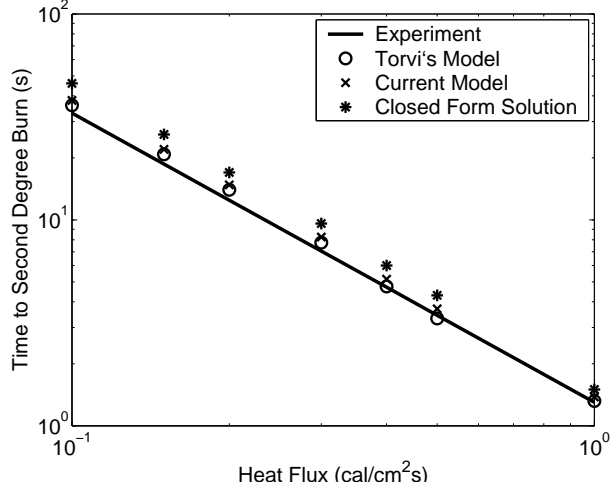


Figure 5.3: Time to second degree burn at the base of skin epidermis.

from skin surface to the environment, while steam burn is different. We model steam burn by adjusting the source term to include condensation. Since condensation is the reverse process of evaporation, we may implement this by changing the sign of Q_e and Q_d in Eq. (3.1). Due to the lower pressure at skin surface, water molecules moves from hot air toward it. The movement of vapor molecules slows down on skin surface, since temperature on skin is lower than the steam temperature. A thin layer of liquid film is formed on the skin surface. Heat transfer from steam to skin is via this thin film. Assume steam heat transfer to skin can be modeled as film condensation on a vertical plate, the heat transfer to skin surface may be written as [49]

$$Q = \bar{h}_L A (T_{sat} - T_s), \quad (5.10)$$

where Q is the heat transfer rate from steam to skin, T_{sat} is the temperature of saturated vapor, the convective heat transfer coefficient is

$$\bar{h}_L = C \left[\frac{g \rho_l (\rho_l - \rho_v) k_l^3 H}{\mu_l (T_{sat} - T_s) L} \right]^{1/4}.$$

in which C is a constant, g the gravitational acceleration (m/s^2), ρ_l the density of liquid water (kg/m^3), ρ_v the density of saturated water vapor, k_l the thermal conductivity of liquid water (W/(mK)), H the latent heat of vaporization (J/kg),

which is a function of temperature, μ_l the viscosity of liquid water (kg/(sm)), and L the characteristic length (m). In applying Eq. (5.10) to find the temperature distribution in skin, T_s is not known, which has to be solved iteratively with Eq. (3.1). The latent heat of water condensation is temperature dependent, which is expressed in a polynomial from least-squares data fitting based on the tabulated data from [63]. All liquid phase properties are evaluated at the film temperature $T_f = (T_{sat} + T_s)/2$. Part of the solution is shown in Fig. 5.4 as compared with that of Ng and Chua's [75] for the prediction of the third degree burn. For the same steam temperature, our model predicts that more time is needed for the third degree burn. It is worth noting that the threshold for a third degree burn in their model is at temperature above 44 °C at the base of the dermis layer, while in our model it is the accumulated damage of $\Omega = 1$ for temperatures over 44 °C.

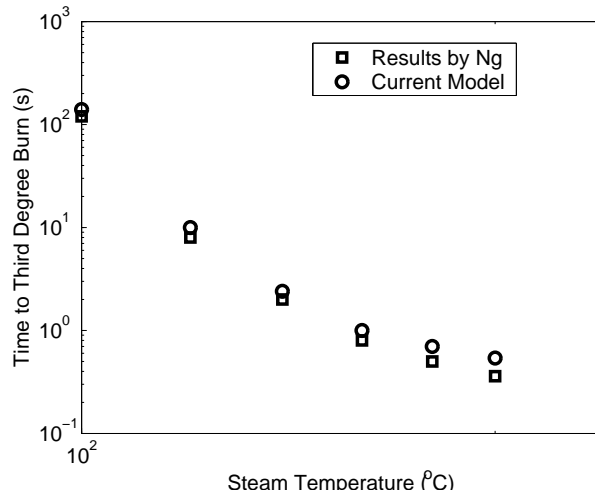


Figure 5.4: Predicted time to the third degree burn for various steam temperature.

5.6 Summary

A 3D model is developed to investigate the skin injury caused by thermal exposure with the consideration of deformation, which may introduce strain energy. The model is based on the consideration of Penne's bioheat equation for skin thermal response,

Duhamel-Neuman equation for thermal stress and strain calculation, and Henriques' suggestion of Arrhenius equation for the skin damage prediction. A numerical algorithm is presented to solve those equations in sequence. It is found that strain energy lowers the activation energy for protein denaturation, and thus tends to give a prediction of shorter time for both the second and the third degree skin burns. But the effect may not be significant in the tested cases, so skin burn prediction without the consideration of deformation energy is still a reasonable approach. However, if the external heating source is extremely large, mechanical energy may play an important role in predicting skin thermal injury.

This model can be easily adapted to simulate burns of various thermal exposure. In particular, a number of numerical experiments have been conducted including laser type heating source, flash fire, and steam exposure, which are typical thermal burns. Our model tends to predict longer time for skin thermal damage. This may be due to the fact that water evaporation is considered in modeling the skin heat transfer process. Water evaporation takes away some of the heat, which cools skin surface.

Finite difference method is used to discretize the PDEs involved in the model, which gives an accuracy of second order in space. For the time dependent problems, Crank-Nicholson scheme is used such that second order accuracy is achieved in time as well. Preconditioned iterative method is used for fast solution of the resulting sparse linear systems.

6 Steady and Unsteady Diffusion Flame Solver

6.1 Introduction

Diffusion flames are frequently encountered in practical combustion devices, such as jet turbines and commercial burners [110, 132, 133, 83]. A desired combustion device should be efficient in energy transfer and produces few pollutants. Studying the mechanism of diffusion flame is very helpful in achieving the goal of high efficiency and low pollution combustion. With the improved computing capability of computers, numerical simulation plays an increasingly important role in exploring the mysteries of physical world, such as multi-dimensional diffusion flame, which combines fluid flow and chemical reaction. The governing equations of diffusion flames are strongly coupled and characterized by the presence of stiff source terms and nonlinearities [28]. Previous studies have shown that Newton's method is extremely efficient in solving the coupled nonlinear system of equations arisen from combustion [110, 132, 133, 10, 11, 31]. This work also applies Newton's method for the simulation of steady and unsteady laminar diffusion flame. The unsteady laminar diffusion flame was solved by Mohammed and others [72] using the primitive form of the Navier-Stokes equations and one-sided difference to avoid staggered grid, and it was solved by Bennett and Smooke [11] using vorticity-velocity formulation of the Navier-Stokes and local rectangular refinement. This work also applies the vorticity-velocity formulation of the Navier-Stokes equations to the simulation of diffusion flames, but different from [11], the unsteady flame is solved on a single non-uniform mesh without local grid refinement. The efficiencies of obtaining the steady-state solution by solving the steady Navier-Stokes and obtaining one by solving the time-dependent Navier-Stokes are compared.

6.2 Laminar Diffusion Flame Model

The laminar diffusion flame model consists of two parts: the gas flow and chemical reaction. The gas flow is simulated using Navier-Stokes equations, and the chemical reaction is simulated by the one-step chemical reaction flame sheet model [110, 132, 133, 28]. These two mechanisms are introduced below.

6.2.1 Vorticity-Velocity Formulation

Assuming the gas is a Newtonian fluid that obeys Fick's law of diffusion, the compressible Navier-Stokes equations can be applied for the simulation of fluid flow in diffusion flames. In particular, the newly emerged vorticity-velocity formulation of the Navier-Stokes is used to avoid staggered grid discretization, which is normally required for solving the primitive variable form of the Navier-Stokes equations, due to the appearance of the first-order derivative terms of pressure. The transport equations for unsteady non-reacting flow can then be written in vorticity-velocity form in the axisymmetric coordinates as [31, 77]:

$$\begin{aligned} \frac{\partial}{\partial r} \left(\frac{1}{\rho} \frac{\partial \rho}{\partial t} \right) + \frac{\partial^2 u}{\partial r^2} + \frac{\partial^2 u}{\partial z^2} - \frac{\partial \omega}{\partial z} + \frac{1}{r} \frac{\partial u}{\partial r} - \frac{u}{r^2} \\ + \frac{\partial}{\partial r} \left(\frac{u}{\rho} \frac{\partial \rho}{\partial r} + \frac{v}{\rho} \frac{\partial \rho}{\partial z} \right) = 0, \end{aligned} \quad (6.1)$$

$$\begin{aligned} \frac{\partial}{\partial z} \left(\frac{1}{\rho} \frac{\partial \rho}{\partial t} \right) + \frac{\partial^2 v}{\partial r^2} + \frac{\partial^2 v}{\partial z^2} + \frac{\partial \omega}{\partial r} + \frac{1}{r} \frac{\partial u}{\partial z} \\ + \frac{\partial}{\partial z} \left(\frac{u}{\rho} \frac{\partial \rho}{\partial r} + \frac{v}{\rho} \frac{\partial \rho}{\partial z} \right) = 0, \end{aligned} \quad (6.2)$$

$$\begin{aligned} -\rho \frac{\partial \omega}{\partial t} + \omega \frac{\partial \rho}{\partial t} - \frac{\partial \rho}{\partial z} \frac{\partial u}{\partial t} + \frac{\partial \rho}{\partial r} \frac{\partial v}{\partial t} + \frac{\partial^2(\mu\omega)}{\partial r^2} + \frac{\partial^2(\mu\omega)}{\partial z^2} \\ + \frac{\partial}{\partial r} \left(\frac{\mu\omega}{r} \right) = \rho u \frac{\partial \omega}{\partial z} + \rho v \frac{\partial \omega}{\partial r} - \frac{\rho u \omega}{r} \\ + \frac{\partial \rho}{\partial z} \frac{\partial}{\partial r} \left(\frac{u^2 + v^2}{2} \right) + \frac{\partial \rho}{\partial r} \left(\mathbf{g} - \frac{\partial}{\partial z} \left(\frac{u^2 + v^2}{2} \right) \right) \\ + 2 \left(\frac{\partial \mu}{\partial r} \frac{\partial}{\partial z} (\nabla \cdot \mathbf{u}) - \frac{\partial \mu}{\partial z} \frac{\partial}{\partial r} (\nabla \cdot \mathbf{u}) - \frac{\partial^2 \mu}{\partial r \partial z} \frac{\partial u}{\partial r} \right) \\ + 2 \left(\frac{\partial^2 \mu}{\partial r^2} \frac{\partial u}{\partial z} - \frac{\partial^2 \mu}{\partial z^2} \frac{\partial v}{\partial r} + \frac{\partial^2 \mu}{\partial r \partial z} \frac{\partial v}{\partial z} \right). \end{aligned} \quad (6.3)$$

The above equations are respectively the equations of radial velocity, axial velocity, and vorticity, where u is the radial velocity, v is the axial velocity, ω is the vorticity, defined as $\omega = \frac{\partial u}{\partial z} - \frac{\partial v}{\partial r}$, ρ is the density, μ is the viscosity, $\nabla \cdot \vec{\mathbf{u}}$ is the divergence of the velocity vector $\vec{\mathbf{u}} = [u \ v]^T$, and $\vec{\mathbf{g}}$ is the gravity vector $\vec{\mathbf{g}} = [g_r \ g_z]^T$. The divergence of the velocity vector in the axisymmetric coordinates is,

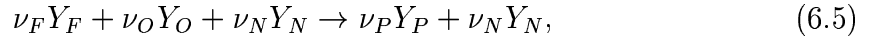
$$\nabla \cdot \vec{\mathbf{u}} = \frac{\partial u}{\partial r} + \frac{u}{r} + \frac{\partial v}{\partial z}. \quad (6.4)$$

The component of $\vec{\mathbf{g}}$ in r coordinate is ignored, and only the g_z component is considered. Note that the energy equation is not included in the above system of Navier-Stokes equations, as it is not solved explicitly. Instead, a conserved scalar equation is introduced and the temperature field is obtained from the conserved scalar, which will be discussed later. The density is computed using the perfect gas law as a function of the pressure. The flow's small Mach number allows the pressure to be approximated as a constant [31, 110, 132], and the density of the gas can then be approximated as $\rho \approx \frac{p_{atm}W}{RT}$, where p_{atm} is the atmospheric pressure, W is the average molecular weight of the gas, R is the idea gas constant, and T is the temperature of the gas. The pressure field is then eliminated from the governing equations as a dependent unknown, and it can be recovered once the numerical solution of the governing equations is obtained [31], by solving a Laplace equation derived by taking the divergence of the momentum equations.

6.2.2 Flame Sheet Model

We use the flame sheet model for simulating the chemistry in diffusion flame. The flame sheet idea was proposed by Burke and Schumann [15] and later used by many researchers [76, 110, 132]. The flame sheet model is a good benchmark problem for testing the performance of particular numerical methods, and also can be used as an initial guess for the computation of more detailed chemical reaction flows. In a diffusion flame, the reaction rate is determined by the rate at which the fuel and

oxidizer are brought together in proper proportions [110]. Under the flame sheet model, the chemical reaction in a diffusion flame can be described by a one-step global irreversible reaction, and the reaction is assumed to be infinitely fast and limited to a very thin exothermic reaction zone, in which the fuel and oxidizer react in stoichiometric proportion. Such a simplified model makes the simulation relatively easy by separating the fuel and oxidizer with no fuel on the oxidizer side and no oxidizer on the fuel side. Due to the existence of concentration gradients in the flow field, both the fuel and oxidizer diffuse toward the thin reaction zone. In the presence of an inert gas, the reaction of the fuel and oxidizer in the flame sheet model can be described in the form [133]



where Y_F , Y_O , Y_P , and Y_N are the mass fractions of fuel, oxidizer, product, and inert gas respectively, and ν_F , ν_O , ν_P , and ν_N are the stoichiometric coefficients of the reaction. To further simplify the model, we assume that thermal diffusion is negligible, the specific heat, c_p is constant, the mass diffusion obeys Fick's law, and the Lewis numbers of all the species, which are defined as, $\frac{\lambda}{\rho D_F c_p}$, $\frac{\lambda}{\rho D_O c_p}$, $\frac{\lambda}{\rho D_P c_p}$, and $\frac{\lambda}{\rho D_N c_p}$, where, λ is the thermal conductivity of the mixture, D_F , D_O , D_P , and D_N are the diffusion coefficients of the fuel, oxidizer, product, and inert gas, are equal to unity. The energy equation and the transport equations of species become mathematically similar by the above simplifications [132]. A scalar variable, conserved scalar, is introduced such that the temperature and the mass fraction of species are related to this variable. The solution of the energy equation and the species equations can be formulated from the conserved scalar, which is described by the following time-dependent convection-diffusion type of equation [110, 133]

$$\rho \frac{\partial S}{\partial t} + \rho v_r \frac{\partial S}{\partial r} + \rho v_z \frac{\partial S}{\partial z} = \frac{1}{r} \frac{\partial}{\partial r} \left(r \rho D \frac{\partial S}{\partial r} \right) + \frac{\partial}{\partial z} \left(\rho D \frac{\partial S}{\partial z} \right). \quad (6.6)$$

This source-free convection-diffusion equation expresses a balance between convection and diffusion of the conserved scalar, which has a desired feature that it is conserved exactly throughout the domain.

6.2.3 Boundary Conditions

To simulate the axisymmetric laminar diffusion flame, the Navier-Stokes equations and the conserved scalar equation are expressed in the axisymmetric coordinates, which include a radial direction and an axial direction, and they are set as horizontal and vertical directions respectively in this work. The boundary conditions for the Navier-Stokes equations and the conserved scalar equation can be summarized as [28]: at the axis of symmetry ($r = 0$): $u = 0$, $\frac{\partial v}{\partial r} = 0$, $\omega = 0$, and $\frac{\partial S}{\partial r} = 0$; at the outer zone ($r = R$): $\frac{\partial u}{\partial r} = 0$, $\frac{\partial v}{\partial r} = 0$, $\omega = \frac{\partial u}{\partial z}$, and $S = 0$; at the inlet ($z = 0$): $u = 0$, $v = v^0(r)$, $\omega = \frac{\partial u}{\partial z} - \frac{\partial v}{\partial r}$, and $S = S^0(r)$; at the exit ($z = L$): $u = 0$, $\frac{\partial v}{\partial z} = 0$, $\frac{\partial \omega}{\partial z} = 0$, and $\frac{\partial S}{\partial z} = 0$.

6.3 Newton's Method

Newton's method is used for the computation of non-reacting viscous and inviscid flows combining with finite difference discretization [24, 125]. It was used by Smooke's group [110, 133, 31, 11, 77] to successfully simulate the laminar diffusion flame. Newton's method is particularly robust in solving coupled nonlinear equations, such as those describing reacting flows. Theoretically, the Newton iteration converges quadratically under certain sufficient conditions, which means that the magnitude of the residual is squared with each Newton step so that it tends to zero very quickly. The disadvantage of Newton's method is that the size of the Jacobian matrix formed is extremely large and it is difficult to find a good initial guess. It has been reported [110, 132] that the formation and solution of the numerical Jacobian matrix constitute the major part of the computation. In order to stabilize the convergence at an early stage of the iteration and to save computing time, the damped Newton's method is

used. For convenience, the full and damped Newton iterations are briefly introduced below.

The Newton's method for a system of equations can be derived from multi-variable Taylor expansion. Let $F(\mathbf{u}) = 0$ be the system of equations in residual form, obtained by discretizing the governing differential equations, the Taylor expansion of the left-hand side, $F(\mathbf{u})$, about the current location \mathbf{u}^k is [57]

$$\mathbf{F}(\mathbf{u}^{k+1}) = \mathbf{F}(\mathbf{u}^k) + \mathbf{F}'(\mathbf{u}^k)(\mathbf{u}^{k+1} - \mathbf{u}^k) + O((\mathbf{u}^{k+1} - \mathbf{u}^k)^2), \quad (6.7)$$

where, \mathbf{F} is the nonlinear vector residual function and \mathbf{u} is the vector of unknown dependent variables. By using the condition of $F(\mathbf{u}) = 0$, i.e., Eq. (6.7), and neglecting the second-order terms, the standard Newton iteration can be constructed as

$$\mathbf{J}(\mathbf{u}^k)\delta\mathbf{u}^k = -\mathbf{F}(\mathbf{u}^k), \quad k = 0, 1, \dots, \quad (6.8)$$

or

$$\mathbf{u}^{k+1} = \mathbf{u}^k + \delta\mathbf{u}^k = \mathbf{u}^k + \mathbf{J}(\mathbf{u}^k)^{-1}\mathbf{F}(\mathbf{u}^k), \quad k = 0, 1, \dots, \quad (6.9)$$

where $\mathbf{J} \equiv \mathbf{F}'$ is the Jacobian matrix, and k indicates the k -th Newton iteration. The damped Newton's method is consequently written in the following form:

$$\mathbf{J}(\mathbf{u}^k)\delta\mathbf{u}^k = -\lambda^k\mathbf{F}(\mathbf{u}^k), \quad k = 0, 1, \dots, \quad (6.10)$$

or

$$\mathbf{u}^{k+1} = \mathbf{u}^k + \lambda^k\delta\mathbf{u}^k = \mathbf{u}^k - \lambda^k\mathbf{J}(\mathbf{u}^k)^{-1}\mathbf{F}(\mathbf{u}^k), \quad k = 0, 1, \dots, \quad (6.11)$$

where λ^k is the k -th damping parameter, taking as $0 < \lambda^k < 1$. The Jacobian matrix in Eqs. (6.8) \sim (6.11) is computed numerically through the following procedure [132]. For the flame sheet model and the vorticity-velocity formulation of the Navier-Stokes equations, the unknown vector consists of four components, i.e., $\mathbf{u} = [u_1 \ u_2 \ u_3 \ u_4]^T$ with $u_1 = u$, $u_2 = v$, $u_3 = \omega$, $u_4 = S$. We also denote the residual vector with four

components $\mathbf{F} = [F_1 \ F_2 \ F_3 \ F_4]^T$. At each point (i,j) , there is a corresponding dense square block with dimension of 4×4 ,

$$\frac{\partial \mathbf{F}}{\partial \mathbf{u}} = \begin{bmatrix} \frac{\partial F_1}{\partial u_1} & \frac{\partial F_1}{\partial u_2} & \frac{\partial F_1}{\partial u_3} & \frac{\partial F_1}{\partial u_4} \\ \frac{\partial F_2}{\partial u_1} & \frac{\partial F_2}{\partial u_2} & \frac{\partial F_2}{\partial u_3} & \frac{\partial F_2}{\partial u_4} \\ \frac{\partial F_3}{\partial u_1} & \frac{\partial F_3}{\partial u_2} & \frac{\partial F_3}{\partial u_3} & \frac{\partial F_3}{\partial u_4} \\ \frac{\partial F_4}{\partial u_1} & \frac{\partial F_4}{\partial u_2} & \frac{\partial F_4}{\partial u_3} & \frac{\partial F_4}{\partial u_4} \end{bmatrix}. \quad (6.12)$$

Each element in the above 4×4 block is evaluated by the finite difference approximation [132],

$$\frac{\partial F_i}{\partial u_j} = \frac{F_i(u_j + \delta u_j) - F_i(u_j)}{\delta u_j}, \quad (6.13)$$

where δu_j is a small perturbation of the j -th component of the unknown vector \mathbf{u} , which is calculated as $\delta u_j = \alpha u_j + \beta$, where α and β are typically taken to be the square root of the machine unit round-off error.

The Newton iteration is terminated when the 2-norm of the difference of the unknown vector between two consecutive iterations satisfies the pre-determined convergence tolerance. To be specific, following the procedure described in [31], we scale each of the four dependent variables such that each of them is of a size similar to the others of equal importance, and the 2-norm of the discrete vector $\delta \mathbf{u}^n$ can be written as [31]

$$\|\delta \mathbf{u}^n\| = \sqrt{\frac{1}{N} \sum_{i=1}^{n_1} \sum_{j=1}^{n_2} \sum_{k=1}^{n_3} \left(\frac{1}{\alpha_k} \delta \mathbf{u}^n \right)^2}, \quad (6.14)$$

where $N = n_1 n_2 n_3$, α_k is the scaling factor of the k -th component of the unknown vector, and n_1 , n_2 , and n_3 are the number of points in r -direction, the number of points in z -direction, and the number of elements of the unknown vector \mathbf{u} respectively. For the Newton iteration, the convergence is achieved when $\|\delta \mathbf{u}^n\| < 10^{-4}$. In each of the Newton iteration, the inner linear system is solved by a Krylov type linear solver with preconditioners.

6.4 Finite Difference Approximation and Linear Solver

The discretization method adopted in the present study is finite difference on a non-equispaced mesh. The Navier-Stokes equations in vorticity-velocity formulation and the conserved scalar equation include first-order linear and nonlinear derivatives, second-order derivatives, and second-order cross derivatives. Different discretization strategies are applied to ensure numerical accuracy and stability. Due to the existence of second-order cross derivatives, a nine-point finite difference stencil is employed for the two-dimensional axisymmetric laminar diffusion flame. For the time-dependent problem, we use an implicit finite difference technique, which earns a saving of 3 orders of magnitude fewer time steps to complete the transient process [11].

Both the first-order linear derivatives and the second-order derivative terms are discretized using central difference. Using non-uniform mesh, for example, the following finite difference formulations can be obtained,

$$\frac{\partial \omega}{\partial r} = \frac{\omega_{i+1,j} - \omega_{i-1,j}}{r_{i+1,j} - r_{i-1,j}}, \quad (6.15)$$

$$\frac{\partial^2 u}{\partial r^2} = \frac{2}{r_{i+1,j} - r_{i-1,j}} \left(\frac{u_{i+1,j} - u_{i,j}}{r_{i+1,j} - r_{i,j}} - \frac{u_{i,j} - u_{i-1,j}}{r_{i,j} - r_{i-1,j}} \right), \quad (6.16)$$

$$\begin{aligned} \frac{\partial}{\partial r} \left(\frac{u}{\rho} \frac{\partial \rho}{\partial r} \right) &= \frac{\left(\frac{u_{i+1,j}}{\rho_{i,j}} + \frac{u_{i,j}}{\rho_{i+1,j}} \right) (\rho_{i+1,j} - \rho_{i,j})}{(r_{i+1,j} - r_{i,j})(r_{i+1,j} - r_{i-1,j})} \\ &\quad - \frac{\left(\frac{u_{i-1,j}}{\rho_{i,j}} + \frac{u_{i,j}}{\rho_{i-1,j}} \right) (\rho_{i,j} - \rho_{i-1,j})}{(r_{i,j} - r_{i-1,j})(r_{i+1,j} - r_{i-1,j})}. \end{aligned} \quad (6.17)$$

The first-order nonlinear derivative terms, such as convective terms, are discretized using a monotonic upwind approximation [110, 111],

$$\begin{aligned} \rho v \frac{\partial u}{\partial r} &= \rho_{i,j} \left(\left\| \frac{v_{i,j} + v_{i-1,j}}{2} \right\|, 0 \right)_{\max} \frac{u_{i,j} - u_{i-1,j}}{r_{i,j} - r_{i-1,j}} \\ &\quad + \rho_{i,j} \left(\left\| \frac{v_{i,j} + v_{i+1,j}}{2} \right\|, 0 \right)_{\max} \frac{u_{i,j} - u_{i+1,j}}{r_{i+1,j} - r_{i,j}}, \end{aligned} \quad (6.18)$$

where $\|a, b\|_{max}$ is the operator of taking the maximum of a and b . The second-order cross derivatives are discretized using the corner points on the standard nine-point stencil,

$$\frac{\partial}{\partial r} \left(\frac{v}{\rho} \frac{\partial \rho}{\partial z} \right) = \frac{\frac{v_{i+1,j}}{\rho_{i+1,j}} (\rho_{i+1,j+1} - \rho_{i+1,j-1})}{(r_{i+1,j} - r_{i,j}) (z_{i+1,j} - z_{i,j})} - \frac{\frac{v_{i-1,j}}{\rho_{i-1,j}} (\rho_{i-1,j+1} - \rho_{i-1,j-1})}{(r_{i+1,j} - r_{i,j}) (z_{i+1,j} - z_{i,j})}. \quad (6.19)$$

For terms involving both the temporal and spatial derivatives, they are discretized using second order backward Euler scheme for temporal derivative and central difference for spatial derivative, as shown in Eq. (6.20). For the boundary part, at $x = 0$, second order three point forward difference is used, and at $x = R$, second order three point backward difference is used.

$$\frac{\partial}{\partial r} \left(\frac{1}{\rho} \frac{\partial \rho}{\partial t} \right) = \frac{\frac{\frac{3}{2}\rho_{i+1}^{n+1} - 2\rho_{i+1}^n + \frac{1}{2}\rho_{i+1}^{n-1}}{\rho_{i+1}^{n+1}} - \frac{\frac{3}{2}\rho_{i-1}^{n+1} - 2\rho_{i-1}^n + \frac{1}{2}\rho_{i-1}^{n-1}}{\rho_{i-1}^{n+1}}}{(r_{i+1} - r_{i-1})\Delta t}. \quad (6.20)$$

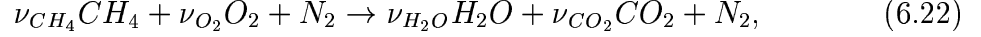
After writing the governing equations in discrete form, the partial differential equations are transformed into N coupled nonlinear algebraic equations, where N equals the product of the number of unknowns and the number of mesh points in the computational domain. The resulting system of equations, written in residual form, is solved by the damped Newton's method. The Newton Jacobian matrix is ill-conditioned, and a fast linear solver based on bi-conjugate gradient stabilized (Bi-CGSTAB) [123] method combined with a block Gauss-Seidel preconditioner [31] is used to solve the linear system. The Bi-CGSTAB is developed for non-symmetric matrix, and each iteration requires two matrix-vector products and four inner products.

6.5 Results and Discussion

Numerical solutions for the steady-state and unsteady-state methane/air diffusion jet flames are obtained and are presented in this section. The configuration of the jet flow is similar to those reported in [72]. The fuel jet and the coflowing oxidizer jet

nonzero elements in each row is $9 \times n_c$, and the maximum number of nonzeros in the Jacobian matrix is $9 \times n_c^2 \times n_r \times n_z$. For a 129×161 mesh and four components, the number of unknowns is 83,076, and the number of nonzeros is 2,990,736.

Following the flame sheet model, the one-step irreversible reaction for the methane/air diffusion flame can be written as [10, 133],



where the stoichiometric coefficients ν_{CH_4} , ν_{O_2} , ν_{H_2O} , and ν_{CO_2} , are taken as 1, 2, 2, and 1 respectively. We use this equation to recover the temperature and the mass fraction of major species. Under the assumption of infinite rate chemistry, the reaction zone becomes infinitely thin under the stoichiometric condition [76]. In three dimensions the infinitely thin reaction zone forms a surface called stoichiometric surface. The combustion domain has been separated into two parts: the fuel side where oxidizer is absent and the oxidizer side where fuel is absent. At the stoichiometric surface, the mass fractions of both fuel and oxidizer are zero, i.e., $Y_{CH_4} = Y_{O_2} = 0$, so the stoichiometric mixture fraction is constant there. The conserved scalar is also constant at the stoichiometric surface, which can be determined as [133]:

$$S_s = \frac{1}{1 + \frac{W_{CO_2}\nu_{CO_2}(Y_{CH_4})_f}{W_{CH_4}\nu_{CH_4}(Y_{CO_2})_o}}, \quad (6.23)$$

where the subscripts s , o , and f indicate the stoichiometric surface, oxidizer side, and fuel side respectively. We have to keep track of the location of the stoichiometric surface to determine the scopes of fuel side region and oxidizer side region, since different mechanisms are used in computing the temperature and the mass fraction of major species in different regions. For example, on the fuel side, we have

$$T = T_f S + \left(T_o + (Y_{CO_2})_o \frac{Q}{c_p} \frac{W_{CH_4}\nu_{CH_4}}{W_{O_2}\nu_{O_2}} \right) (1 - S), \quad (6.24)$$

$$Y_{CH_4} = (Y_{CH_4})_f S + (Y_{O_2})_o \frac{W_{CH_4}\nu_{CH_4}}{W_{O_2}\nu_{O_2}} (S - 1), \quad (6.25)$$

and on the oxidizer side, we have

$$T = T_o(1 - S) + \left(\frac{Q}{c_p} (Y_{CH_4})_f + T_f \right) S, \quad (6.26)$$

$$Y_{O_2} = (Y_{O_2})_o(1 - S) - (Y_{CH_4})_f \frac{W_{O_2} \nu_{O_2}}{W_{CH_4} \nu_{CH_4}} S. \quad (6.27)$$

The mass fraction of other species can be obtained in a similar way, as presented in [132, 133]. In Eqs. (6.24) ~ (6.27), Q is the heat release per unit mass of the fuel, c_p the specific heat of the mixture, W the molecular weight of each species. In the transport equations and the conserved scalar equation, fluid properties, such as the viscosity, the mixture density, the mixture diffusivity, are temperature dependent. After the temperature is obtained, the related properties can be found as follows. The temperature dependence of viscosity is approximated by the power law [133] $\mu = \mu_0 \left(\frac{T}{T_0} \right)^r$, where $T_0 = 298$ K, $r = 0.7$, and $\mu_0 = 1.857 \times 10^{-4}$ gm/cm. From the definition of the Prandtl number $Pr = \frac{\mu c_p}{\lambda}$, we obtain the relation of $\frac{c_p}{\lambda} = \frac{Pr}{\mu}$. The Lewis number is assumed to be one $Le = \frac{\lambda}{\rho D c_p} = 1$, and we further obtain $\rho D = \frac{\lambda}{c_p} = \frac{\mu}{Pr}$, where λ is the thermal conductivity of the mixture, and the Prandtl number is taken as $Pr = 0.75$.

The nonlinear coupled equations of the combustion problems are very difficult to solve. Special techniques are needed for the convergence of the numerical solution as well as the savings in computational cost. A good initial solution guess is absolutely necessary for the convergence of the Newton's method and very important for fast solution of the iterative process. In the studies reported in [28, 31], the initial solution guess for the axial velocity and conserved scalar is approximated according to the boundary conditions. Such approximation, however does not affect the final steady-state solution due to the applications of pseudo-time process adopted by [110, 133, 31] and relatively small time steps. Therefore, in the current investigation, for both steady-state and unsteady-state diffusion flames, the initial guess is set to zero for

u , v , and S , and 298 K for T . Newton's method is used to linearize the original equations, and the Newton iteration is considered to have converged if the 2-norm of the difference of the scaled dependent variable, defined in Eq. (6.14), is less than 1.0×10^{-4} , and Bi-CGSTAB is considered to have converged when the 2-norm of the scaled residual vector is less than or equal to $\frac{1}{10}$ of the Newton tolerance [31].

The steady-state solution is obtained using a three-level multigrid method [28, 31] with the finest mesh of 129×161 and coarsest mesh of 33×41 . In pseudo-time stepping, the steady-state solution can be achieved by first marching the unsteady process until the solution is within the convergence domain of the steady-state solution, then to start the full Newton process. The steady-state temperature distribution is shown in Figure 6.2, and the obtained maximum axial velocity and temperature are 2.63 m/s and 2050 K respectively, and the total CPU time on a Sun-Blade-100 machine with a single 500 MHz SPARC processor and 2 GB memory, is 11.8 minutes. The number of linear iterations is 559, 1097, and 1568 for levels 1, 2, and 3 respectively, where level 1 is the coarsest level and level 3 is the finest level.

The time-dependent solution is computed on a single non-uniform grid 129×161 . The evolution of the laminar diffusion flame with time is presented in Figure 6.3, which shows the development of flame temperature profile in the early stage of a flame. At $t = 0.125$ s, the obtained temperature profile of the flame is close to the steady-state solution, with the highest temperature of 2050 K and the highest axial velocity of 2.61 m/s. It is found that 50 times more CPU time is needed to get a steady-state solution using the unsteady-state equations than that using the steady-state equations with the pseudo-time approach. This is because, in the former case, we solve the unsteady-state equations on the finest mesh only and the new Jacobian matrix is computed in each time step.

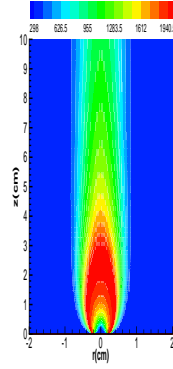


Figure 6.2: The temperature profile obtained from the steady-state equations for the diffusion flame.

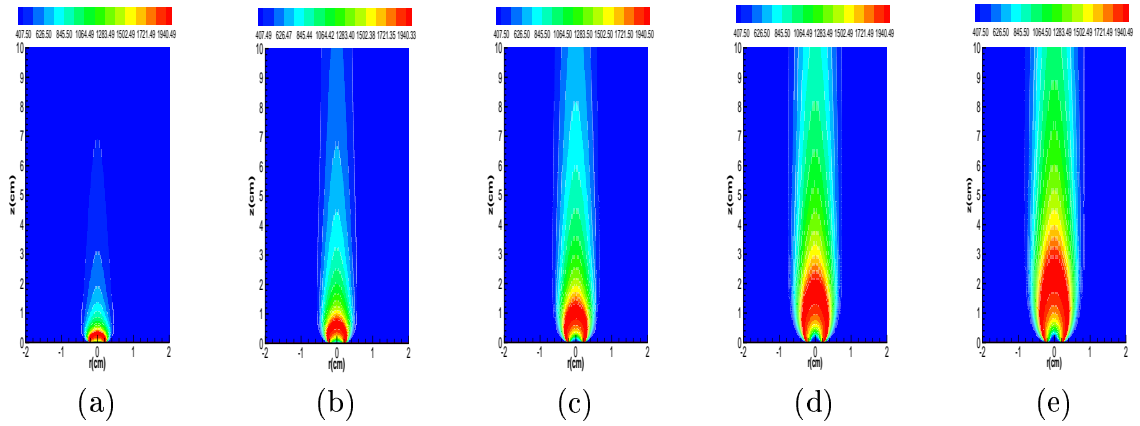


Figure 6.3: The dependency of flame temperature on time: (a) $t = 0.025$ s, (b) $t = 0.05$ s, (c) $t = 0.075$ s, (d) $t = 0.1$ s, and (e) $t = 0.125$ s.

6.6 Summary

We simulate laminar diffusion flame numerically by considering methane and air as the reaction input. For the flow part, we use the vorticity-velocity formulation of Navier-Stokes equations, and for the chemical part we use a simplified one equation flame sheet model with infinite rate of chemical reaction. The coupling between the fluid flow and chemical reaction is through a so-called conserved scalar equation. Even though the very simple one equation chemical reaction model is used for the flame problem, reasonable results are obtained. This indicates that the Newton's method is very efficient for the simulation of coupled highly nonlinear physical processes such as the complicated combustion problems. The steady-state solution is obtained by solving the steady-state Navier-Stokes equations using multigrid V-cycle algorithm with Bi-CGSTAB as the linear solver preconditioned with GS, or to run the time dependent Navier-Stokes equations until the solution between the consecutive time steps is small enough. It is found that it is more efficient to obtain a steady-state solution from the steady-state Navier-Stokes equations than to get one from the transient Navier-Stokes equations in terms of computational cost.

7 Protein Transport in Capillary with Competitive Binding and Signaling

7.1 Introduction

Angiogenesis, the physiological process in the growth of new blood vessels from pre-existing vessels, is required for proper development, normal physiology, as well as wound healing for all organs of the body. It is also critical for tumor growth. Tumors require a blood supply to grow from microscopic size to macroscopic size [37]. Cells are unable to be nourished properly beyond an oxygen diffusion distance of about 200 μm and therefore require blood vessels in their vicinity. This can be accomplished by the growth of capillaries. The process begins with the degradation of existing matrix and the migration of endothelial cells into the areas to be vascularized, followed by proliferation of endothelial cells and formation of capillaries. The formed capillaries are initially blind-ended, but eventually open themselves to become functional blood vessels, in a not well-understood process. The growth of endothelial cells and tumor cells can be stimulated or inhibited by certain molecules. Basic fibroblast growth factor (FGF-2), a soluble protein, is such a stimulator that acts from cell surface to affect the growth and differentiation of a wide range of cell types, such as endothelial, mesodermal, and ectodermal. It has been involved in processes ranging from wound healing to tumor growth [29]. The growth factor binds to its cell surface tyrosine kinase receptors, as well as heparan sulfate proteoglycans (HSPGs) on cell surfaces. The activity of FGF-2 binding to its receptors is significantly reduced in cells that do not express heparan sulfate [33]. Under normal conditions, the levels of FGF-2 in extracellular matrices and circulation are relatively low, which can be substantially elevated in cases of disease and cancer conditions. It has been found that FGF-2 is crucial for normal developmental processes such as limb bud formation [89], instrumental in blood vessel growth, and directive in creating new vessel sprouts [89, 32]. For example, in the congenital disease hemangioma, a vascular disease char-

acterized by uncontrolled overgrowth of blood capillaries, increased concentrations of FGF-2 have been detected in circulation. One of the most effective treatments for hemangioma is interferon alpha, an FGF-2 inhibitors [78]. The temporal and spatial distribution of FGF-2 in extracellular matrices and circulation is elemental to normal development as well as disease control. The concentration of FGF-2 can be regulated by some heparan binding proteins.

The role of heparan sulfate in modulating FGF-2 receptor binding has been the subject of many studies. Lovich and Edelman [68] performed computational simulations of heparin deposition and distribution in local vascular system. In their paper, the diffusion of heparin in tissue was considered, while the heparin binding kinetics was relatively simple. Lovich *et al.* [69] studied transvascular transport, investigated the role of diffusion and convection on arterial heparin deposition by administrating the perivascular and endovascular aspects of calf carotid artery *in vitro* and the rabbit iliac artery *in vivo*, and found that arterial thickness played a very important role in determining the balance between diffusive and convective forces. A quantitative model of diffusion and convection, however, has not been established in their paper. Dowd *et al.* [29] analyzed the transport of FGF-2 through Descemet's membrane (DM), the basement membrane of the corneal endothelium. In their study, the diffusion of FGF-2 through the interstices of the membrane was considered, coupled with fast, reversible association of FGF-2 to resident heparan sulfate chains. Forsten *et al.* [39] suggested an overall mechanism describing heparin-mediated activities. That mechanism includes heparin and growth factor binding, heparin and growth factor receptor binding, and their couplings with the number of heparin binding sites on a given cell type. Fannon *et al.* [33] used the same model as Forsten *et al.* [39] to predict the potentiation and inhibition of FGF-2 binding by heparin. They reported that FGF-2 binding as well as FGF-2-induced signaling and mitogenic response was sensitive to HSPG and heparin within a range of physiologically relevant concentrations.

They also found that the stimulation and inhibition of FGF-2 by heparin might result from differences in doses and time courses used in various studies. Recently, Forsten *et al.* [40] published a more complete model about the kinetics of FGF-2 binding to heparin sulfate proteoglycans and MAP (mitogen-activated protein) kinase signaling. Their model suggests that FGF-2, its receptor, and a heparan sulfate proteoglycan interact simultaneously to form a high-affinity complex. The heparan sulfate chain could act by binding both FGF-2 and its receptor, facilitating the FGF-2-receptor interaction. In this manner, the cell surface proteoglycan and receptor could each bind FGF-2 and then come together to form a stable complex, as well as some compound dimers. The growth factor binding models published by Forsten and Fannon [39, 33, 40] were developed to describe a static tissue culture dish type environment in which fluid flow and mass transport were not involved.

In many *in vivo* situations, the transport and binding of FGF-2 is closely related with circulation. This paper describes a general mathematical model and provides efficient numerical methods for simulating the binding of a ligand L (FGF-2) simultaneously and competitively to two different binding sites, FGFR and HSPG, located on the surface of a capillary, under flow condition *in vitro*. The basic model for surface reactions that we have used are works by Forsten [39, 40] and Fannon [33, 34], in which FGF-2 is the only ligand in the solution, binding sites FGFR and HSPG are assumed to locate only on the surface of capillaries. As illustrated in Fig. 7.1, FGF-2 binds to FGFR and HSPG to form complexes of FGF-2-FGFR and FGF-2-HSPG, the resulting complexes may continue binding to produce either their dimers or FGF-2-FGFR-HSPG complex, and the FGF-2-FGFR-HSPG may further bind each other to generate FGF-2-FGFR-HSPG dimers. Consequently, the concentration of FGF-2 in the solution is greatly affected due to molecular binding [134].

A coupled nonlinear convection-diffusion-reaction model for simulating heparan sulfate chain regulation over the growth factor binding under flow conditions is pro-

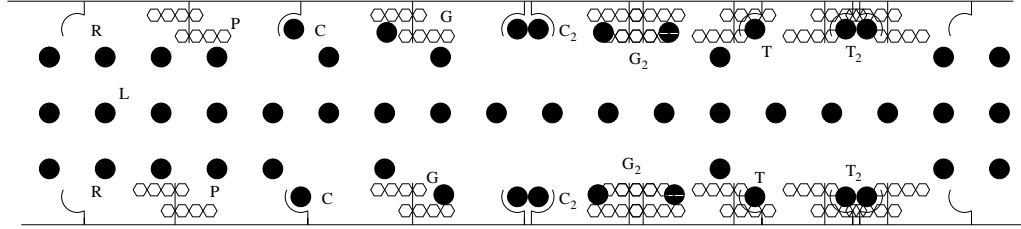


Figure 7.1: Sketch of growth factor binding to receptors and HSPG and the formation of various compounds on the surface of a capillary. The symbols in the sketch are as follows: L=FGF-2, R=FGFR, P=HSPG, C= FGF-2-FGFR complex, G=FGF-2-HSPG complex, C₂=FGF-2-FGFR dimer, G₂=FGF-2-HSPG dimer, T=FGF-2-FGFR-HSPG complex, and T₂=FGF-2-FGFR-HSPG dimer.

posed here. This model provides the computational infrastructure needed to study the effects of heparin and heparan sulfate on growth factor-binding within the bioreactor system, to simulate the media flow system in capillaries *in vitro*, and to evaluate the effect of competing growth factor-binding proteins on cell surface under flow conditions. The model could serve as a prototype for the more advanced simulation of growth factor-binding to receptors as well as heparan sulfate chains in circulation *in vivo*. In particular, the model is used to predict the time-dependent distribution of FGF-2 in a capillary with complicated binding kinetics on the tube surface.

Three types of physical processes are included in this coupled nonlinear model: the media flow, the transport of proteins in the flow, and the chemical kinetics of related proteins. These processes are simulated by incompressible Navier-Stokes equations for media flow, convection-diffusion transport equations for species conservation, and kinetic equations for molecular binding. The flow is considered independent of species transport and surface binding processes and is computed separately. After the flow field has been obtained, we solve the transport equation, where the velocity field is considered known. Since in the current basic model, the molecular binding of FGF-2 to binding sites is assumed to take place on the tube surface only, we may model the process as mass transport in a pipe with chemical reaction boundary conditions [134].

7.2 Incompressible Navier-Stokes Equations

The blood flow in human vascular system is frequently considered as incompressible [16, 26]. Thus in the current simulation *in vitro*, a bioreactor system, the flow of media, which is essentially water, is also regarded as incompressible. Due to the particular geometry of the vascular system, it is more convenient to write the governing equations in cylindrical coordinates. Assume the flow in the vascular system is axisymmetrical and laminar, a 3D problem can be reduced to a 2D equivalent one. In cylindrical coordinates, all derivatives with respect to the circumferential direction are zero and the three velocity components are functions of the axial and radial directions only. If circumferential flow is not considered, the governing equations can be further simplified. The 2D time-dependent equations for mass and momentum in conservation form for incompressible flow in an axisymmetric coordinate system can be written as:

The mass conservation equation

$$\frac{\partial u}{\partial r} + \frac{u}{r} + \frac{\partial v}{\partial x} = 0, \quad (7.1)$$

the radial momentum equation

$$\rho \frac{\partial u}{\partial t} + \rho u \frac{\partial u}{\partial r} + \rho v \frac{\partial u}{\partial x} = \rho g_r - \frac{\partial p}{\partial r} + \frac{1}{r} \frac{\partial}{\partial r} (r \tau_{rr}) + \frac{\partial \tau_{rx}}{\partial x}, \quad (7.2)$$

and the axial momentum equation

$$\rho \frac{\partial v}{\partial t} + \rho u \frac{\partial v}{\partial r} + \rho v \frac{\partial v}{\partial x} = \rho g_x - \frac{\partial p}{\partial x} + \frac{1}{r} \frac{\partial}{\partial r} (r \tau_{rx}) + \frac{\partial \tau_{xx}}{\partial x}. \quad (7.3)$$

In Eqs. (7.1) ~ (7.3), ρ is the density, u is the radial velocity, v the axial velocity, p the dynamic pressure, g_r and g_x the radial and axial components of gravity respectively. The stress tensors τ_{rr} , τ_{rx} , and τ_{xx} are $\tau_{rr} = 2\mu \frac{\partial u}{\partial r}$, $\tau_{rx} = \mu \left(\frac{\partial u}{\partial x} + \frac{\partial v}{\partial r} \right)$, and $\tau_{xx} = 2\mu \frac{\partial v}{\partial x}$. For a Newtonian incompressible flow, the viscosity μ is a constant. In general, however, the blood flow is considered non-Newtonian, and existing non-Newtonian

blood flow models can be found in open literatures, such as the Carreau model [19, 51] and the power law model [19]. Our current simulation is focused on the flow of media, endothelial cell culture, not blood in a bioreactor, and a constant viscosity is assumed.

Finite volume method [81, 62] has been widely used in solving both steady and unsteady fluid mechanics problems, for it is easy to implement and guarantees flux conservation. To be specific, cell-centered finite volume approach is applied to discretize the partial differential equations. The advantage of cell-centered arrangement is that second order accuracy is achieved, since the nodal value represents the mean over the control volume and the node is located at the centroid to the control volume. The Navier-Stokes consists of a set of coupled nonlinear partial differential equations, the solution of which is not a trivial task, and we adopt the SIMPLER algorithm [81, 35] in the current computation. To solve the Navier-Stokes equations, two loops are required, the inner iteration handles each of the individual equations of momentum and energy, and the outer iteration deals with the coupling and nonlinearity. For unsteady flow using implicit discretization, the discretized linear equations need not be solved very accurately at each outer iteration. Usually a few iterations of a linear solver is enough. More accurate solution will not reduce the number of outer iterations but may increase the computing time.

7.3 Transport Equation of FGF-2

The transport equation of FGF-2 consists of two mechanisms, convection and dissipation. The convection term describes transport of local components along the streamlines of the flow, co-moving with the particles of the fluid. The velocity field of the flow is solved for as described above and is assumed not to be affected by the protein transport. The dissipation term describes diffusive transport of components due to gradient. The local concentration of a component changes with pressure difference, gravitational forces, and viscous dissipation. The mass of each species must

be conserved. In the existence of chemical reaction, the coupling of mass transport and chemical kinetics in a circular pipe can be described by the following equations [134]:

$$\frac{\partial \phi_i}{\partial t} + \frac{1}{r} \frac{\partial (ru\phi_i)}{\partial r} + \frac{\partial (v\phi_i)}{\partial x} = \frac{1}{r} \frac{\partial}{\partial r} \left(K_r r \frac{\partial \phi_i}{\partial r} \right) + \frac{\partial}{\partial x} \left(K_x \frac{\partial \phi_i}{\partial x} \right) + F_i(\phi_1 \dots \phi_n), \quad 1 \leq i \leq n, \quad (7.4)$$

where ϕ_i is the concentration of species i , u and v are the radial and longitudinal components of velocity, K_r and K_z the molecular diffusion coefficients, and F_i the rate of change due to kinetic transformations for each species i . Since in the current basic model, only one species, FGF-2, is placed in the flow, so here ϕ_i is simply FGF-2. Molecular binding happens only on the tube surface, that is to say F_i is valid merely on the pipe surface. The reactants and products involved in the chemical kinetics include FGF-2, FGFR, HSPG, FGF-FGFR complex and its dimer, FGF-HSPG complex and its dimer, FGF-HSPG-FGFR complex and its dimer, with a total of nine species ($n = 9$). The detailed chemical kinetics of these species will be discussed in the Section 7.4. The boundary conditions of Eq. (7.4) are

$$\frac{\partial \phi_i}{\partial r} = f_i(t, x, C_i) \quad \text{at} \quad r = R, \quad \frac{\partial \phi_i}{\partial r} = 0 \quad \text{at} \quad r = 0. \quad (7.5)$$

The first boundary condition accounts for interactions at the vessel wall (R is the radius of the capillary and f_i the rate of binding to cells), while the second boundary condition reflects the axial symmetry.

Transient solution is pursued in the current simulation. To achieve higher order time accuracy, we use a quadratic backward approximation for the time derivative term. Such arrangement gives us second order time accuracy. In the transport equation, the convective term needs special treatments for stability consideration. A frequently used technique is upwind differencing [62]. However, upwind discretization provides only first order spatial accuracy. For the sake of numerical stability as well as higher order spatial accuracy, a deferred correction numerical strategy is used here

[35], which is a combination of the first order upwind differencing and the second order central differencing. The diffusive terms are discretized by central difference. Due to implicit discretization of the governing equations, a linear system is formed and needs to be solved efficiently at each time step. The finite volume expression of Eq. (7.4) may be written as:

$$\frac{3(\rho\phi)_P^{n+1} - 4(\rho\phi)_P^n + (\rho\phi)_P^{n-1}}{\Delta t} + (J_e - J_w) + (J_n - J_s) = S_C + S_P\phi_P + S_{sym}. \quad (7.6)$$

where $J_{e,w,n,s}$ is the convection-diffusion flux at each of the four interfaces of the control volume P , with $J_{e,w} = F_{e,w} - D_{e,w}$, $J_{n,s} = F_{n,s} - D_{n,s}$, S_C and S_P are the results of source term linearization. Using deferred correction [35], the convective flux is written as a mixture of upwind and central differences $F_{e,w} = F_{e,w}^u + \lambda(F_{e,w}^c - F_{e,w}^u)^o$, where $F_e^u = \max((\rho v)_e \Delta r_j, 0.)\phi_P + \min((\rho v)_e \Delta r_j, 0.)\phi_E$, $F_w^u = \max((\rho v)_w \Delta r_j, 0.)\phi_W + \min((\rho v)_w \Delta r_j, 0.)\phi_P$, $F_e^c = (\rho v)_e \Delta r_j(1 - \alpha_e)\phi_P + (\rho v)_e \Delta r_j \alpha_e \phi_E$, $F_w^c = (\rho v)_w \Delta r_j(1 - \alpha_w)\phi_W + (\rho v)_w \Delta r_j \alpha_w \phi_P$, λ is a parameter setting as $\lambda = 0 \sim 1$, and the superscript (o) indicates taking the value from the previous iteration, which will be taken to the right hand side and treated as a part of the source term. The same can be applied to convective flux in radial direction $F_{n,s} = F_{n,s}^u + \lambda(F_{n,s}^c - F_{n,s}^u)$, where $F_n^u = \max((\rho u)_n \Delta x_i, 0.)\phi_P + \min((\rho u)_n \Delta x_i, 0.)\phi_N$, $F_s^u = \max((\rho u)_s \Delta x_i, 0.)\phi_S + \min((\rho u)_s \Delta x_i, 0.)\phi_P$, $F_n^c = (\rho u)_n \Delta x_i(1 - \alpha_n)\phi_P + (\rho u)_n \Delta x_i \alpha_n \phi_N$, $F_s^c = (\rho u)_s \Delta x_i(1 - \alpha_s)\phi_S + (\rho u)_s \Delta x_i \alpha_s \phi_P$. The interpolation factors are defined as $\alpha_e = \frac{x_e - x_P}{x_E - x_P}$, $\alpha_w = \frac{x_P - x_w}{x_P - x_W}$, $\alpha_n = \frac{r_n - r_P}{r_N - r_P}$, and $\alpha_s = \frac{r_P - r_s}{r_P - r_S}$. The diffusion fluxes are $D_e = \frac{K_x r_j (\phi_E - \phi_P)}{x_E - x_P}$, $D_w = \frac{K_x r_j (\phi_P - \phi_W)}{x_P - x_W}$, $D_n = \frac{K_r x_i (\phi_N - \phi_P)}{r_N - r_P}$, and $D_s = \frac{K_r x_i (\phi_P - \phi_S)}{r_P - r_S}$. The notations of spatial discretization in Eq. (7.6) is illustrated in Fig. 7.2, where the uppercase letters indicate the center of the control volumes, and the lowercase letters indicate the interfaces between neighboring control volumes.

Substituting everything into Eq. (7.6) and collecting terms, a set of algebraic

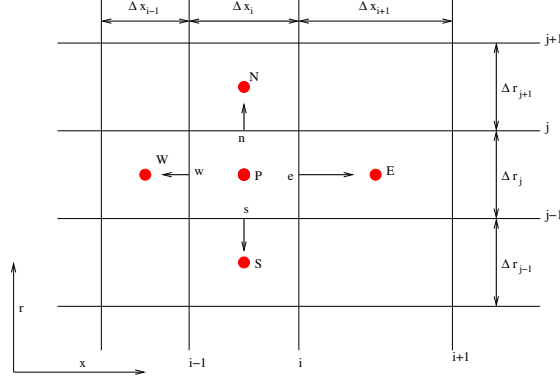


Figure 7.2: Finite volume notation of control volumes in axisymmetrical coordinates.

equations are obtained, which is in the following form

$$A_S\phi_S + A_W\phi_W + A_P\phi_P + A_E\phi_E + A_N\phi_N = b. \quad (7.7)$$

The coefficients of Eq. (7.7) consist of a pentadiagonal matrix, and they are given by $A_S = -\max((\rho u)_s \Delta x_i, 0.) - \frac{K_r \Delta x_i r_s}{r_P - r_S}$, $A_W = -\max((\rho v)_w \Delta r_j, 0.) - \frac{K_x \Delta r_j r_P}{x_P - x_W}$, $A_N = \min((\rho u)_n \Delta x_i, 0.) - \frac{K_r \Delta x_i r_n}{r_N - r_P}$, $A_E = \min((\rho v)_e \Delta r_j, 0.) - \frac{K_x \Delta r_j r_P}{x_E - x_P}$, and $A_P = \frac{3\rho r_P \Delta x_i \Delta r_j}{2\Delta t} - (A_W + A_S + A_E + A_N)$. The right hand side vector is given by $b = (S_C + S_P)r_P \Delta x_i \Delta r_j + \left(\frac{4.0\rho\phi_P^n}{2.0\Delta t} - \frac{\rho\phi_P^{n-1}}{2.0\Delta t}\right)r_P \Delta x_i \Delta r_j - \lambda(F_e^c - F_e^u - F_w^c + F_w^u + F_n^c - F_n^u - F_s^c + F_s^u)$. The banded matrix is solved by Stone's strong implicit procedure (SIP) [114], a special kind of incomplete LU factorization.

7.4 Competitive Binding Kinetics

The change of concentration with respect to time for various species may be described by a set of ordinary differential equations (ODEs) in terms of mole or mass fraction. FGF-2 binding involves a series of molecular activities, including binding to receptors, HSPG, and some intermediate complexes. Some models have been proposed to reveal the related chemical kinetics [32, 39, 40] by examining the role of low-affinity receptors on high-affinity receptor binding. It is usually assumed that each cell has a homogeneous distribution of FGF receptors (R) and heparan sulfate proteoglycan binding

sites [39]. Synthesis of receptors and surface HSPG as well as internalization of unbound receptors, surface HSPG, and FGF-2 complexes are considered as well. The internalization process is modeled by a first-order chemical kinetics, and the internalization rates are based on experimental measurements obtained previously using Balbc/3T3 [32] and vascular smooth muscle cells [112]. Synthesis of receptors and HSPG is considered constitutive and based on steady-state levels of surface molecules and the turnover rate for unbound receptors/HSPG. Available binding sites are based on data from the literature for cultured endothelial cells and indicate a difference of two orders of magnitude in binding sites (1.6×10^4 high affinity sites vs. 1.6×10^6 low affinity sites) [34, 40].

In the current work, only the base model is considered. The base model assumes a single signaling species of HSPG, which is written as HSPG in the model, as described in an early work by Forsten et al. [40]. There are eight chemical reactions in the model and nine species are involved. A directed graph is used to represent the reaction network of molecular binding in the base model, as shown in Fig. 7.3. In the directed graph, the species involved in the reactions are represented by vertices, and the reactions are represented by directed edges. The number of edges, however, does not necessarily equal to the number of reactions, since there may be more than one reactants and/or products in a single reaction. The internalization of FGFR, HSPG, FGF-2-FGFR, FGF-2-HSPG, FGF-2-FGFR dimer, FGF-2-HSPG, FGF-2-FGFR-HSPG, and FGF-2-FGFR-HSPG dimer is included in the directed graph as well [134].

The model is based on mass-action kinetics describing binding interactions between FGF-2 and FGFR and HSPG. The detailed chemical kinetics is based on the work done by Forsten et al. [40] and is re-illustrated in Table 7.1 for convenience. There are eight reactions and three of them are reversible. These reaction equations show the synthesis of FGFR and HSPG and surface coupling between FGF-2

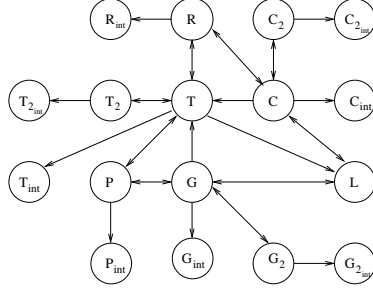


Figure 7.3: The reaction network for the base model. The same symbolic representation of the species as in Fig. 7.1 is used here. Only single signaling HSPG is considered in this model. Single arrowheads indicate an irreversible reaction and double arrowhead indicate a reversible reaction. Both FGFR and HSPG can mediated signaling through T_2 [40].

bound complexes. The remaining eight reaction equations exhibit the internalization of bound and unbound FGFR and HSPG. To minimize the complexity of this preliminary model, we assume that each binding site is independent, and no clustering of sites are involved. Taking mass balance of each of the nine components in the reaction network, a system composed of a set of nine nonlinear ordinary differential equation is obtained, shown in the Appendix. Using FGF-2-HSPG as an example, the change of FGF-2-HSPG concentration with time in the base model can be described as

$$\frac{dG}{dt} = k_f^P LP - k_r^P G - k_c RG - k_c G^2 + 2k_{uc} G_2 - k_{int} G, \quad (7.8)$$

where $k_f^R LP$ is the production of FGF-2-HSPG due to the binding of FGF-2 to unbound HSPG, $-k_r^P G$ is the dissociation of FGF-2-HSPG to FGF-2 and HSPG, $-k_c RG$ is the loss due to surface coupling of an FGF-2-HSPG complex with unbound FGFR, $-k_c G^2$ is the loss due to the formation of FGF-2-HSPG dimers, $2k_{uc} G_2$ is the increase due to the dissociation of FGF-2-HSPG dimers, and $-k_{int} G$ is the loss due to internalization. The remaining eight nonlinear ordinary differential equations can be found in the Appendix.

The set of nine equations shown in the Appendix are obtained from the reactions in Table 7.1, and they indicate the local rate of protein concentration change due

Table 7.1: Chemical reactions included in the base model using mass-action kinetics and their relevant parameters.

Chemical reaction	Reaction rate	Parameters
$L + R \xrightleftharpoons[k_r^R]{k_f^R} C$	$k_f^R[R][L], k_r^R[C]$	$k_f^R = 2.5 \times 10^8 \text{M}^{-1} \text{min}^{-1}, k_r^R = 0.048 \text{min}^{-1}$
$L + P \xrightleftharpoons[k_r^P]{k_f^P} G$	$k_f^P[P][L], k_r^P[C]$	$k_f^P = 0.9 \times 10^8 \text{M}^{-1} \text{min}^{-1}, k_r^P = 0.068 \text{min}^{-1}$
$R + G \xrightarrow{k_c} T$	$k_c[R][G]$	$k_c = 0.001 \text{min}^{-1} (\#/ \text{cell})^{-1}$
$C + P \xrightarrow{k_c} T$	$k_c[C][P]$	$k_c = 0.001 \text{min}^{-1} (\#/ \text{cell})^{-1}$
$T \xrightarrow{k_r^T} L + R + P$	$k_r^T[T]$	$k_r^T = 0.001 \text{min}^{-1}$
$C + C \xrightleftharpoons[k_{uc}]{k_c} C_2$	$k_c[C]^2, k_{uc}[C_2]$	$k_c = 0.001 \text{min}^{-1} (\#/ \text{cell})^{-1}, k_{uc} = 1 \text{min}^{-1}$
$G + G \xrightleftharpoons[k_{uc}]{k_c} G_2$	$k_c[G]^2, k_{uc}[G_2]$	$k_c = 0.001 \text{min}^{-1} (\#/ \text{cell})^{-1}, k_{uc} = 1 \text{min}^{-1}$
$T + T \xrightleftharpoons[k_{uc}]{k_c} T_2$	$k_c[T]^2, k_{uc}[T_2]$	$k_c = 0.001 \text{min}^{-1} (\#/ \text{cell})^{-1}, k_{uc} = 1 \text{min}^{-1}$
$R \xrightarrow{k_{int}} R_{int}; P \xrightarrow{k_{int}} P_{int}$	$k_{int}[R]; k_{int}[P]$	$k_{int} = 0.005 \text{min}^{-1}$
$C \xrightarrow{k_{int}} C_{int}; G \xrightarrow{k_{int}} G_{int}$	$k_{int}[C]; k_{int}[G]$	$k_{int} = 0.005 \text{min}^{-1}$
$T \xrightarrow{k_{int}} T_{int}; C_2 \xrightarrow{k_{int}^D} C_{2_{int}}$	$k_{int}[T]; k_{int}^D[C_2]$	$k_{int} = 0.005 \text{min}^{-1}; k_{int}^D = 0.078 \text{min}^{-1}$
$G_2 \xrightarrow{k_{int}^D} G_{2_{int}}; T_2 \xrightarrow{k_{int}^D} T_{2_{int}}$	$k_{int}^D[G_2]; k_{int}^D[T_2]$	$k_{int}^D = 0.078 \text{min}^{-1}$

to biochemical reactions. For the coupled nonlinear ODE system with time t as the sole independent variable, our initial try using a fourth-order standard Runge-Kutta method was not successful. The failure may due to the nonlinearity and stiffness of the ODE. We then turn to a stiff ordinary differential equation solver using the backward differentiation formulation [12].

7.5 Numerical Procedure

The problem involves the solution of a coupled PDE system, i.e., the incompressible Navier-Stokes equations and the convection-diffusion transport equation. The numerical procedure of solving the PDE system is illustrated in Algorithm 10, where the outmost loop is a time loop, followed by a while loop to control nonlinear iteration. We use second-order backward implicit scheme for time discretization, hence data need to be saved at time $t - 2$ and $t - 1$. We take the maximum residual of u , v , and p to determine the convergence of the coupled nonlinear system. Since the concentration of ligand is very low, about 10^{-10} M, we may assume that the transport of protein will not affect the media flow. As such, we first obtain the flow field by solving the coupled nonlinear Navier-Stokes equations, where the velocity and pressure are decoupled by a SIMPLE like algorithm [81], then seek the solution of the transport equation. For each of the four equations, u , v , p , and ϕ , a linear system of five diagonals needs to be solved. Several different fast sparse matrix solvers, including Stone's ILU, BICGSTAB, and GMRES have been tried.

7.6 Results

7.6.1 Media flow in artificial capillary

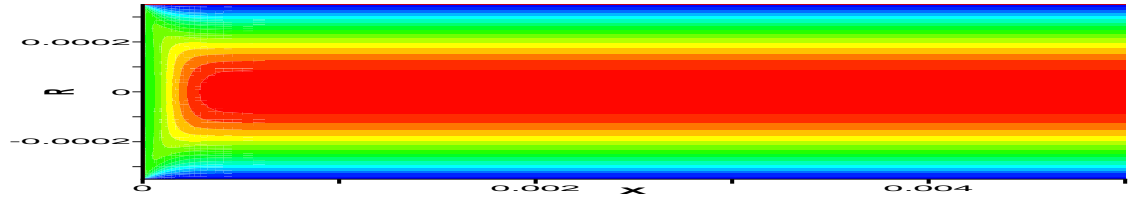
Endothelial cells cultured under chronic shear stress have been shown to form a monolayer, stop dividing, orient to the flow of medium, and form tight junctions [13]. The FiberCellTM bioreactor is especially designed for the long-term culture and study of endothelial cells under flow. The heart of the bioreactor system is a hollow fiber car-

Algorithm 10 Algorithm for Incompressible Flow and Mass Transfer

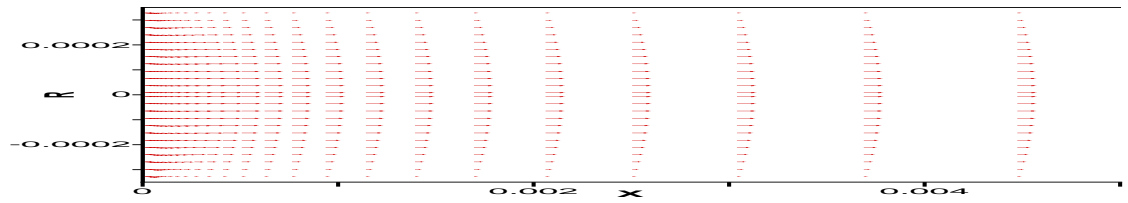
```
while  $t < t_{stop}$  do
  Save data at time  $t - 2$ ,  $(u, v, \phi)^{t-2} \leftarrow (u, v, \phi)^{t-1}$ 
  Save data at time  $t - 1$ ,  $(u, v, \phi)^{t-1} \leftarrow (u, v, \phi)^t$ 
  while  $outerIter < outerIter_{max}$  do
    solve for  $u$ 
    solve for  $v$ 
    solve for  $p$ 
     $residual = \text{Max}(residual_u, residual_v, residual_p)$ 
    if  $residual > largeNumber$  then
      exit "Diverge"
    else if  $residual > convergenceCriteria$  then
      Continue
    else
      Break
    end if
  end while
  solve for  $\phi$ 
end while
```

tridge containing coated fibers on which cells can be cultured [79]. The microprocessor controlled pump can be programmed to produce consistent and defined amounts of shear stress by regulating the flow of medium over the cells allowing a more physiologic environment for cell growth. Both arterial and capillary flow patterns can be simulated by regulating the pump system to generate steady and pulsatile flows. Current study is more interested in the capillary flow in each of the coated fibers. The parameters of the FiberCell bioreactor are as follows, the radius of an individual fiber $R = 0.35$ mm, the fiber length $L = 10$ cm, the number of tubes or fibers per cartridge $N = 20$, the flow rate $r = 80$ ml/min, which corresponds to an average velocity of 0.1732 mm/s. The viscosity is taken as $\mu = 0.04$ dyne \cdot s/cm², and the density of the fluid is taken as $\rho = 1060$ kg/m³ [71].

The numerical solution of medium flow is obtained by the 2D incompressible Navier-Stokes equations, discussed in Section 7.2, and presented in Fig. 7.4. Given the velocity, dimension and medium properties, the Reynold number is less than 1, and the flow in capillary is essentially laminar. Fig. 7.4(a) is the contour plot of



(a)



(b)

Figure 7.4: Visualization of laminar flow in part of the artificial capillary within $x = 0 \sim 0.005$ m. (a) Flood plot of velocity u . (b) Vector plot of velocities u and v .

steady-state axial velocity inside the tube. In order to reveal the flow development in the tube entrance, only a small part of the flow is visualized, i.e., $x = 0 \sim 0.005$ m. Fig. 7.4(b) is the corresponding vector plot of the axial and radial velocities. The velocity distribution in the artificial capillary is very well predicted by the current incompressible code. This claim is supported by a comparison of u velocity profile in the fully-developed region between the numerical and analytical solutions. For a fully-developed laminar flow in a circular pipe, the velocity profile can be found analytically as $u = u_{max} \left(1.0 - \frac{r^2}{R^2} \right)$, where $u_{max} = 2.0 \times u_{inlet}$. The numerical and analytical solutions agree very well with each other, as shown in Fig. 7.5. The numerical solution presented in Figs. 7.4 and 7.5 is obtained by the following boundary conditions: a uniform flow velocity of $u = 0.0001732$ m/s at the tube entrance, non-slip boundary condition on tube surface $u = v = 0$, symmetric boundary condition along the tube centerline $v = 0$ and $\frac{\partial u}{\partial r} = 0$, and extrapolation of velocity by zero gradient at flow

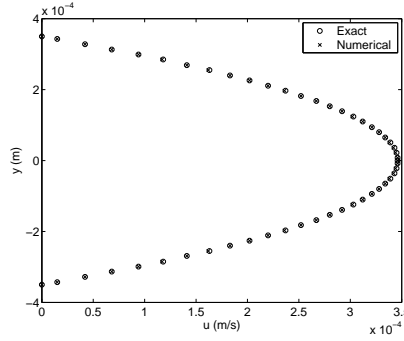
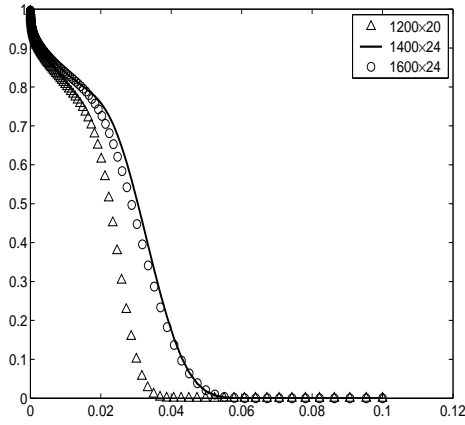


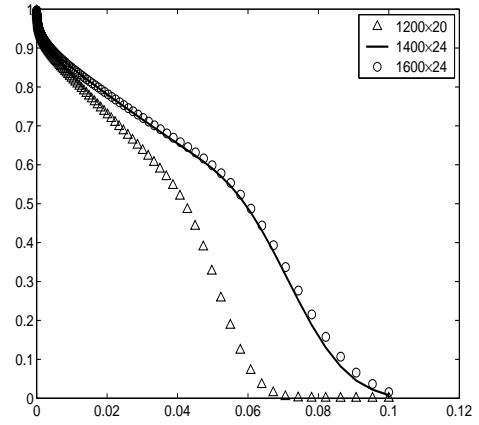
Figure 7.5: Comparison of velocity profile of fully-developed laminar flow in a circular pipe between numerical and exact solutions

exit $u_E = u_P$.

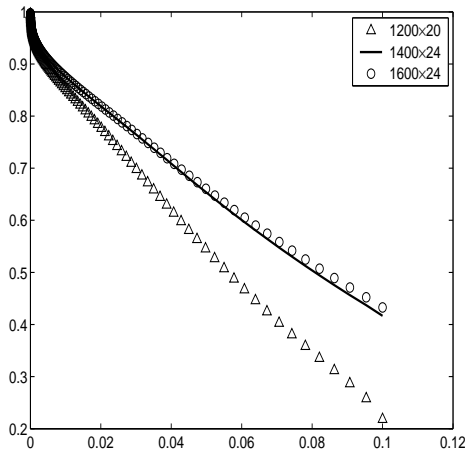
The accuracy of the numerical solution depends very much on the mesh size. Ideally, the numerical solution should be very close to the exact solution of the PDEs in a very fine mesh. However, due to the limited computing resources and the fact that a too small grid spacing may cause unexpected numerical difficulties, using an extremely fine mesh may not be a good strategy. A practical way of achieving enough numerical accuracy is to find a so-called grid-independent solution by the method of try and error, in which we fine the mesh continually until the results between the two consecutive tries are very close. Fig. 7.6 shows the dependency of numerical solution on mesh size. To be specific, three types of mesh size are used, 1200×20 , 1400×24 , and 1600×24 , where the number of control volumes in the axial direction is taken as 1200, 1400, and 1600, and the number of control volumes in the radial direction is taken as 20 and 24, respectively. Figs. 7.6(a) to 7.6(e) are the concentration distribution of FGF-2 along the capillary surface at the time of 5, 10, 20, 40, and 60 minutes, where triangles represent the results of mesh size 1200×20 , solid line represents the results of mesh size 1400×24 , and circles represent those of mesh size 1600×24 . It is clear that the numerical solutions for the two cases of 1400×24 and 1600×24 are close enough to be considered as grid-independent. Therefore, in the rest of the chapter, all numerical results are obtained on the mesh size of 1400×24 .



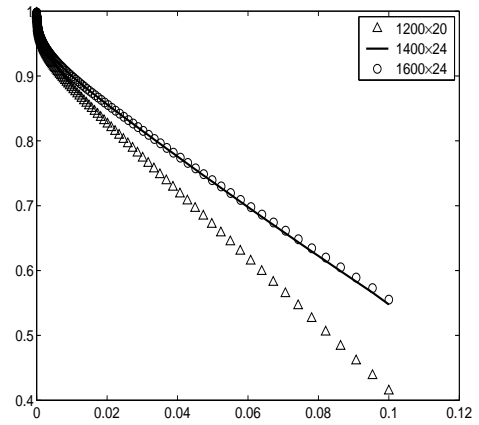
(a)



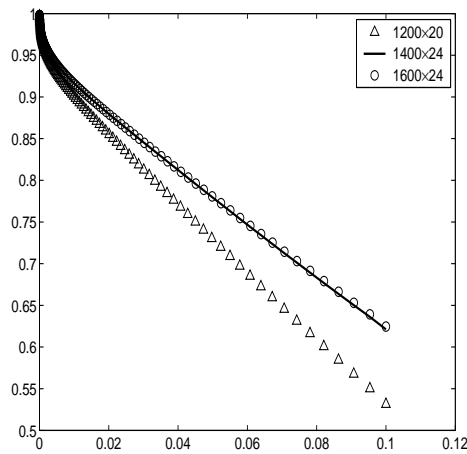
(b)



(c)



(d)



(e)

Figure 7.6: The dependency of numerical solution on mesh size, (a) at $t = 5$ minutes, (b) at $t = 10$ minutes, (c) at $t = 20$ minutes, (d) at $t = 40$ minutes, and (e) at $t = 60$ minutes, where triangles, solid line, and circles represent numerical results of mesh size 1200×20 , 1400×24 , and 1600×24 respectively.

7.6.2 Ligand transport and binding at 4 °C

The transport equation is solved after the velocity in it has been obtained by solving the Navier-Stokes equations. The boundary conditions applied to the convection-diffusion equation are as follows. At the tube entrance, a uniform concentration of $\phi = 5.556 \times 10^{-11}$ mol is prescribed. At the centerline of the capillary, symmetric boundary condition $\frac{\partial \phi}{\partial r} = 0$ is used. At the outlet, we extrapolate the concentration of ligand by zero gradient $\frac{\partial \phi}{\partial x} = 0$, i.e., $\phi_E = \phi_P$. At the tube wall, a reaction boundary condition is implemented to reflect the growth factor binding. On the tube surface, the conservation equation for the growth factor FGF-2 can be written as

$$\frac{\partial \phi}{\partial t} + \mathbf{n} \cdot \|\mathbf{F}\| = G \quad (7.9)$$

where ϕ is the concentration of FGF-2, $\|\mathbf{F}\|$ denotes the diffusion flux through tube surface, \mathbf{n} is the unit vector normal to the surface and pointing from liquid to tube surface, and G is the surface differentiation rate due to biochemical reaction.

On the tube surface, a system of simultaneous ordinary differential equations is obtained from the set of biochemical reaction equations, in the form of mass action kinetics. Let vector \mathbf{y} be the species populations in the chemical reaction networks, $\mathbf{y} = [y_1 \ y_2 \ \cdots \ y_n]^T$, the vector notation of the system of ordinary differential equations may be written as

$$\frac{d\mathbf{y}}{dt} = \mathbf{f}(\mathbf{y}, t). \quad (7.10)$$

Using backward differencing formulation (BDF), Eq. (7.10) is solved by finite difference as

$$\mathbf{y}^n = \mathbf{y}^{n-1} + \Delta t \mathbf{f}(\mathbf{y}^n). \quad (7.11)$$

If all equations are linear, we may replace $\mathbf{f}(\mathbf{y})$ with $\mathbf{f}(\mathbf{y}) = A\mathbf{y}$, where A is the coefficient matrix, and we can use a matrix vector product to find the rate of change of the concentration of relevant species due to a series of reactions, and the ordinary

differential equations can be solved directly. The solution of the linear system is then found to be

$$\mathbf{y}^n = (I - \Delta t A)^{-1} \mathbf{y}^{n-1}. \quad (7.12)$$

where I is the identity matrix.

For a nonlinear system of equations, the solution of Eq. (7.11) is more complicated. Newton's method is frequently used to solve nonlinear system, and the solution of the nonlinear system is

$$\mathbf{y}^n = \mathbf{y}^{n-1} + \Delta t (I - \Delta t J)^{-1} \mathbf{y}^{n-1}. \quad (7.13)$$

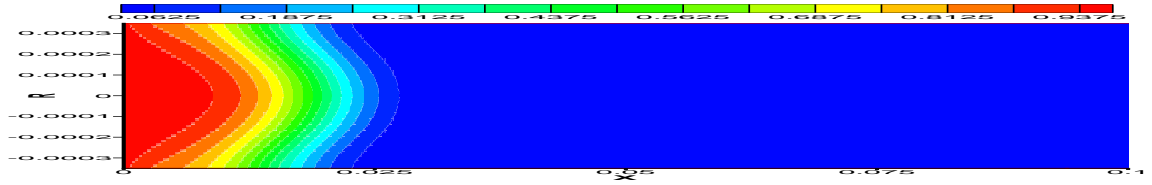
where J is the Jacobian matrix, which is calculated as $J = \frac{\partial \mathbf{f}}{\partial \mathbf{y}}$ to linearize the system. Since the Jacobian matrix J is generally not constant, at each time step, we need to evaluate matrix J and compute the inverse of the matrix $I - \Delta t J$. The Jacobian matrix can be evaluated either analytically or numerically. Analytical Jacobian is always preferred, since the computation of analytical Jacobian matrix is both numerically more accurate and computational more efficient. For the nonlinear nine species base model, Eqs. (8.1)~(8.9), the corresponding Jacobian matrix is,

$$J = \begin{bmatrix} a_{11} & k_r^R & k_r^T & 0 & 0 & -k_c R & -k_f^R R \\ k_f^R L & a_{22} & 2k_{uc} & 0 & 0 & -k_c R & 0 & 0 & k_f^R R \\ 0 & k_c C & a_{33} & 0 & 0 & 0 & 0 & 0 & 0 \\ k_c G & k_c P & 0 & a_{44} & 2k_{uc} & k_c C & k_c R & 0 & 0 \\ 0 & 0 & 0 & k_c T & a_{55} & 0 & 0 & 0 & 0 \\ 0 & -k_c P & 0 & k_r^T & 0 & a_{66} & 0 & -k_f^P P & \\ -k_c G & 0 & 0 & 0 & 0 & k_f^P L & a_{77} & 2k_{uc} & k_f^P \\ 0 & 0 & 0 & 0 & 0 & 0 & k_c G & a_{88} & 0 \\ -k_f^P L/K & k_r^R/K & 0 & k_r^T/K & 0 & -k_f^P L/K & k_r^P/K & 0 & a_{99} \end{bmatrix} \quad (7.14)$$

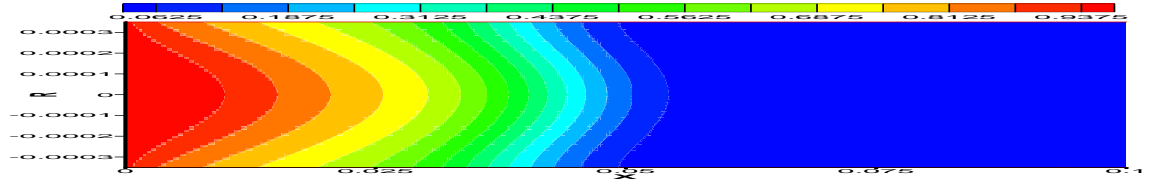
where $a_{11} = -k_f^R L - k_c G - k_{int}$, $a_{22} = -k_r^R - k_c P - 2k_c C - k_{int}$, $a_{33} = -k_{uc} - k_{int}$, $a_{44} = -k_r^T - 2k_c T - k_{int}$, $a_{55} = -k_{uc} - k_{int}$, $a_{66} = -k_f^P L - k_c C - k_{int} P$, $a_{77} = -k_r^P - k_c R - 2k_c G - k_{int}$, $a_{88} = -k_{uc} - k_{int}$, $a_{99} = -(k_f^R L + k_f^P P)/K$, $K = NV$, $N = 6.02 \times 10^{23}$, and $V = 10^{-9}$.

The nonlinear system of ordinary differential equations is solved by the VODE solver [12], which can handle both stiff and nonstiff systems. VODE uses a variable-coefficient form of BDF method. In the stiff case, the Newton iteration is relaxed by a scalar factor. VODE provides a flexible application programming interface (API) through two external subroutines, FEX and JEX, where FEX allows users to provide a set of rate equations from chemical kinetics, the right-hand side vector $\mathbf{f}(\mathbf{y}, \mathbf{t})$, and JEX allows users to calculate analytical Jacobian matrix. Users also have to specify initial values of the system, as well as some parameters, such as relative and absolute tolerances, the lengths of real work array and integer work array. In the current computation, the relative tolerance is set as 10^{-4} , and the absolute tolerance is species dependent, i.e., each species may have its own absolute tolerance. We use BDF method with user-supplied full Jacobian, so the size of the work array is calculated as $LRW = 22 + 9 \times NEQ + 2 \times NEQ^2$, and the size of the integer work array is specified as $LIW = 30 + NEQ$, where NEQ is the number of equations to be solved. To start with, *ISTATE* must be set to 1 in the VODE solver.

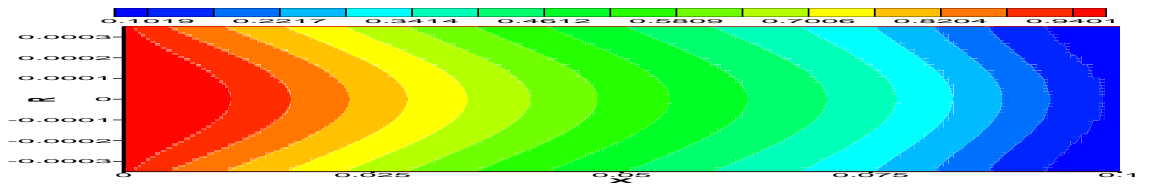
Let us first simulate FGF-2 binding and signaling in media flow at 4°C, and it is experimentally assumed that there is no internalization at 4°C. To satisfy this condition, some parameters in the 9-equation base model have been set to 0, $k_{int} = k_{int}^D = 0$. The computational results of FGF-2 concentration have been scaled with respect to the uniformly specified inlet boundary concentration, $L' = L/L_0$, where $L_0 = 5.5556 \times 10^{-11}$ and presented in Fig. 7.7. Initially, there is no ligand in the solution. To start with, at $t = 0$, we enforce the boundary condition of $L = L_0$ at the tube entrance. The time-dependent solution of FGF-2 concentration corresponding to flow inlet velocity of $u = 0.0000866$ m/s at $t = 5, 10, 20, 40,$ and 60 minutes is shown in Figs. 7.7(a) ~ 7.7(e) in the form of color-filled contour plot. Ligand has been transported into the flow by convection and diffusion. At $t = 5$ minutes, ligand is observed in only a small portion of the tube. At $t = 10$ minutes, ligand occupies



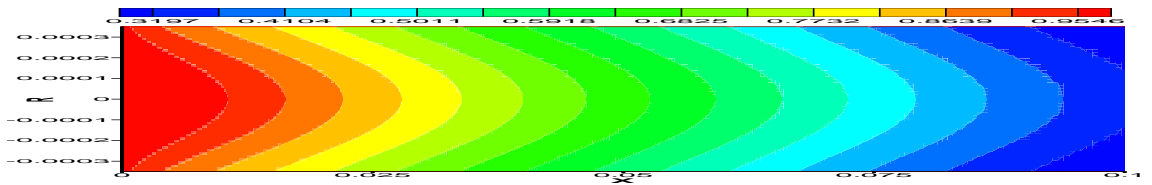
(a)



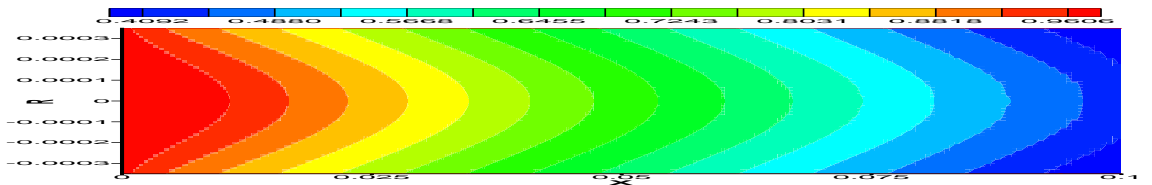
(b)



(c)



(d)



(e)

Figure 7.7: Visualization of ligand transport in the capillary at the condition of 4°C and inlet velocity $u = 0.0000866$ m/s, (a) at $t = 5$ minutes, (b) at $t = 10$ minutes, (c) at $t = 20$ minutes, (d) at $t = 40$ minutes, and (e) at $t = 60$ minutes.

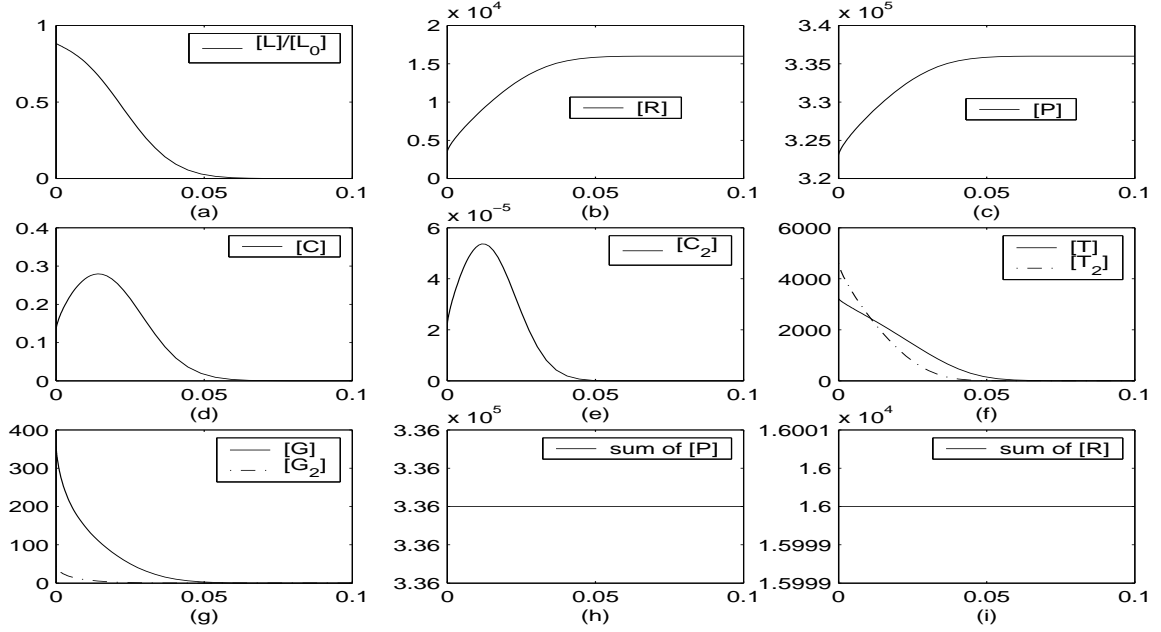


Figure 7.8: The dependency of species concentration at capillary wall on axial axis (x) at $t = 5$ minutes, (a) ligand $[L]/[L_0]$, (b) FGFR, (c) HSPG, (d) FGF-2-FGFR complex, (e) FGF-2-FGFR dimer, (f) FGF-2-FGFR-HSPG complex and its dimer, (g) FGF-2-HSPG complex and its dimer, (h) summation of $[P] + [G] + [T] + 2[G_2] + 2[T_2]$, and (i) summation of $[R] + [C] + [T] + 2[C_2] + 2[T_2]$.

almost a half volume of the tube. At $t = 20$ minutes, ligand can be seen at tube exit. Due to biochemical reactions on the tube surface, more ligand is observed in the tube center than near tube surface.

Biochemical reaction takes place on the tube surface. For the initial value problem, the initial conditions of FGF-2 receptor (R) and signaling heparan sulfate proteoglycan (P) has been set as $R_0 = 1.6 \times 10^4 \#/\text{cell}$ and $P_0 = 3.36 \times 10^5 \#/\text{cell}$ respectively. The concentrations of the nine species in the model under investigation are exhibited in Figs. 7.8 ~ 7.12 for their dependency on time t and location x corresponding to $u = 0.0001732$ m/s. Fig. 7.8 is the solution at $t = 5$ minutes, where $[L]$ decreases down the tube and almost no L has been detected in the region of $x > 0.05\text{m}$. This is due to the fact that ligand has not yet been transported to that part of the tube. The concentration of R and P has been reduced in the region of $x \leq 0.05\text{m}$ because of the bindings of FGF-2 to FGFR and HSPG. In the region where L exists, molecular

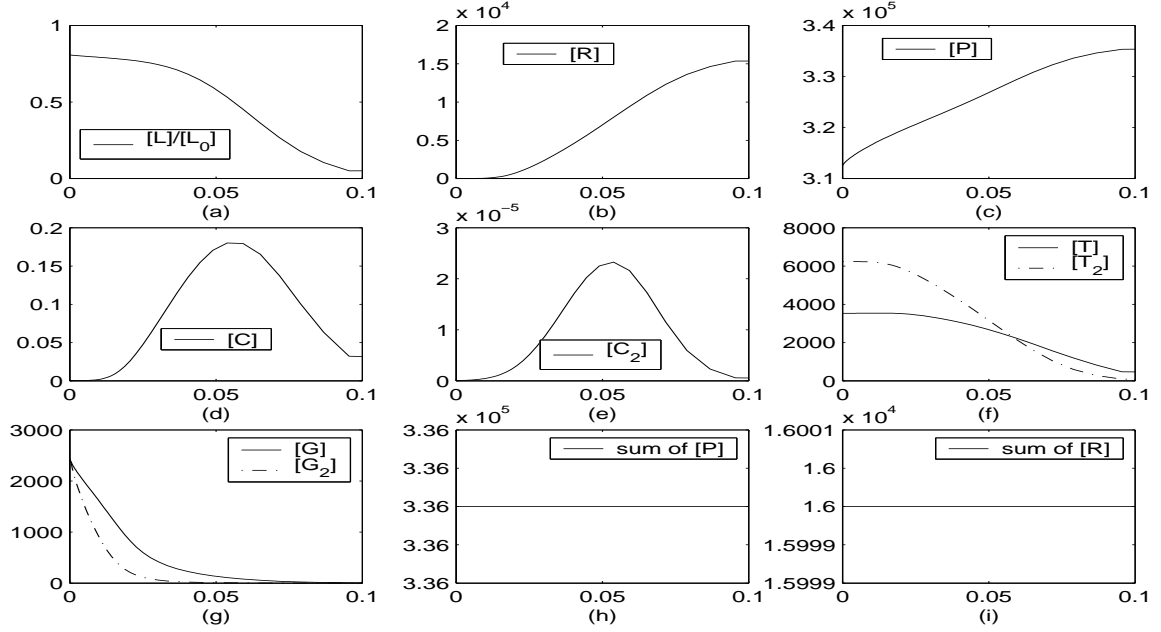


Figure 7.9: The dependency of species concentration at capillary wall on axial axis (x) at $t = 10$ minutes, (a) ligand $[L]/[L_0]$, (b) FGFR, (c) HSPG, (d) FGF-2-FGFR complex, (e) FGF-2-FGFR dimer, (f) FGF-2-FGFR-HSPG complex and its dimer, (g) FGF-2-HSPG complex and its dimer, (h) summation of $[P] + [G] + [T] + 2[G_2] + 2[T_2]$, and (i) summation of $[R] + [C] + [T] + 2[C_2] + 2[T_2]$.

complexes of C , C_2 , T , T_2 , G , and G_2 are formed. The concentrations of T , T_2 , G , and G_2 decrease down the tube, while those of C and C_2 are more complicated, and they initially increase with respect to x to reach a maximum value and then decrease down the tube. At $t = 20$ minutes, L expands to the whole capillary, and its concentration decreases along the capillary. As a consequence of the molecular binding, $[R]$ and $[P]$ can be seen decreasing at the surface of the entire tube. The profiles of $[C]$ and $[C_2]$ are shown as first up and then down. As time goes from $t = 20$ minutes to $t = 40$ and $t = 60$ minutes, the concentrations of L , P , and R keep decreasing. The concentrations of C and C_2 also decrease, while those of $[T]$, $[T_2]$, $[G]$ and $[G_2]$ increase. For the condition of 4°C with no internalization, in all cases that have been studied, the total mass of P and R is conserved, i.e., $[R] + [C] + [T] + 2[C_2] + 2[T_2] = [R_0]$ and $[P] + [G] + [T] + 2[G_2] + 2[T_2] = [P_0]$ and maintained.

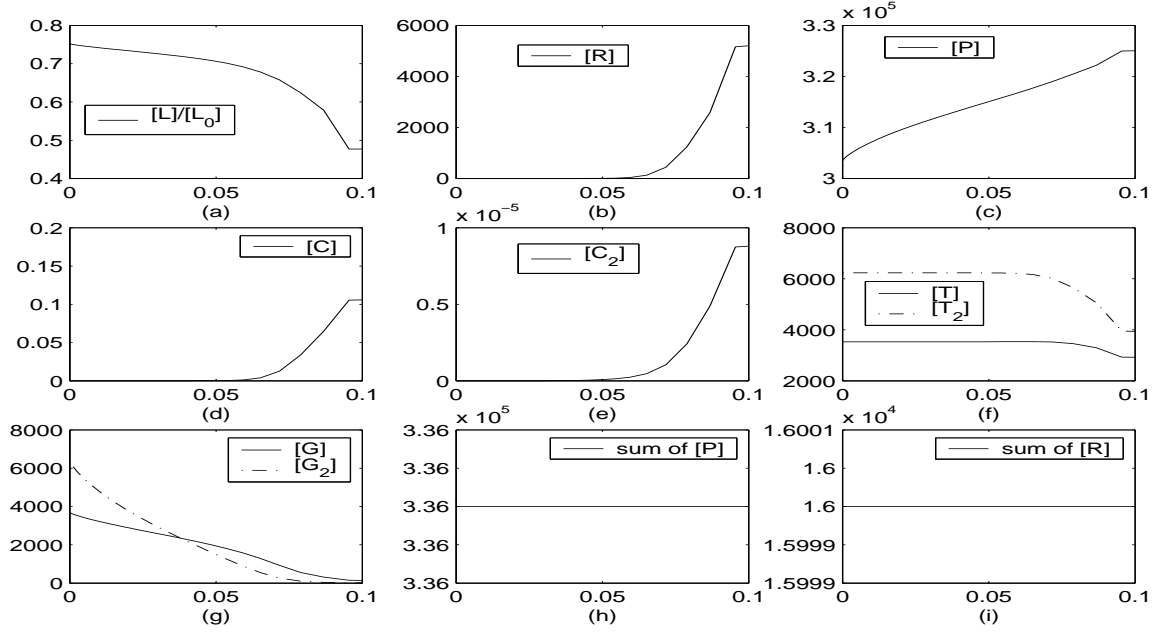


Figure 7.10: The dependency of species concentration at capillary wall on axial axis (x) at $t = 20$ minutes, (a) ligand $[L]/[L_0]$, (b) FGFR, (c) HSPG, (d) FGF-2-FGFR complex, (e) FGF-2-FGFR dimer, (f) FGF-2-FGFR-HSPG complex and its dimer, (g) FGF-2-HSPG complex and its dimer, (h) summation of $[P] + [G] + [T] + 2[G_2] + 2[T_2]$, and (i) summation of $[R] + [C] + [T] + 2[C_2] + 2[T_2]$.

7.6.3 Ligand transport and binding at 37 °C

Under a temperature condition of 37°C, the internalization of R , P , C , G , T , C_2 , G_2 , and T_2 has been considered with a dissociation rate of $k_{int} = 0.005\text{min}^{-1}$ and $k_{int}^D = 0.078\text{min}^{-1}$, as shown in Table 7.1. Exactly the same computation procedure as that in the case of 4°C has been conducted here, except the parameter changes due to internalization, as indicated in the above text. The internalization process of the eight components will cause their concentrations to become lower and consequently affect the distribution of ligand in the solution. The transport of FGF-2 in the capillary is visualized and displayed in Fig. 7.13 for inlet velocity of $u = 0.0000866$ m/s, where Figs. 7.13(a), 7.13(b), 7.13(c), 7.13(d), 7.13(e) corresponds to the results at $t = 5, 10, 20, 40,$ and 60 minutes respectively. The obtained contour plots are very similar to those in the case of 4°C. In the early stage of $t < 20$ minutes, the

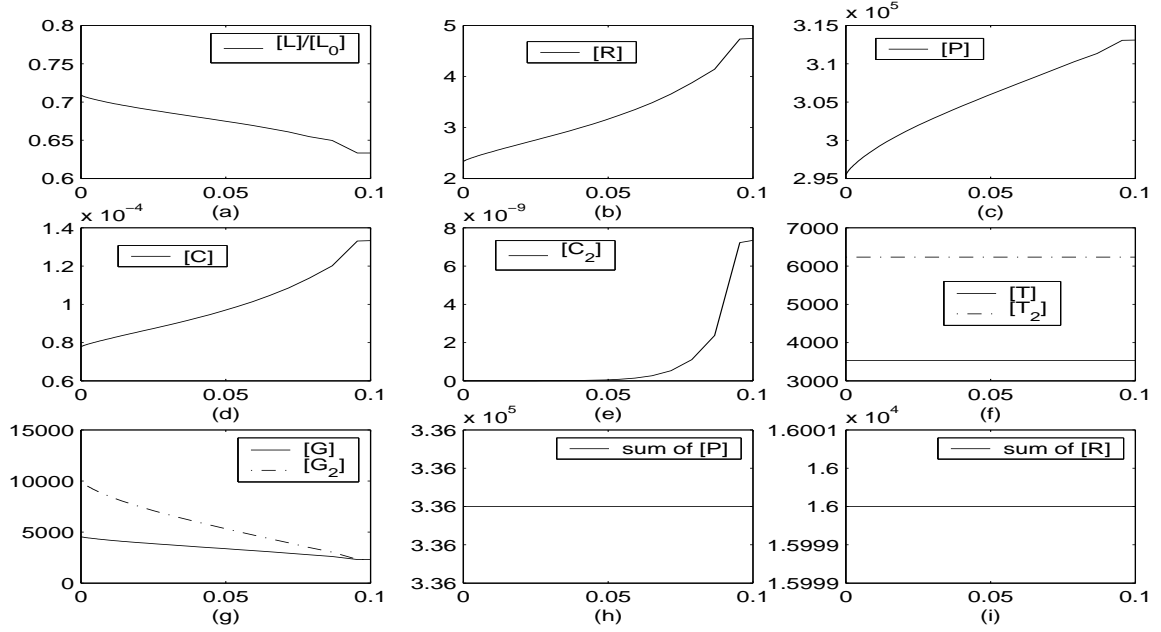


Figure 7.11: The dependency of species concentration at capillary wall on axial axis (x) at $t = 40$ minutes, (a) ligand $[L]/[L_0]$, (b) FGFR, (c) HSPG, (d) FGF-2-FGFR complex, (e) FGF-2-FGFR dimer, (f) FGF-2-FGFR-HSPG complex and its dimer, (g) FGF-2-HSPG complex and its dimer, (h) summation of $[P] + [G] + [T] + 2[G_2] + 2[T_2]$, and (i) summation of $[R] + [C] + [T] + 2[C_2] + 2[T_2]$.

results of ligand concentration are almost the same for the compared two cases. For example, Fig. 7.7(a) and Fig. 7.13(a) are exactly the same, so do Fig. 7.7(b) and Fig. 7.13(b). After running for a longer time, the difference between the two cases are becoming obvious. In the pair of Figs. 7.7(d) and 7.13(d), the same number of contour levels are used, and their contour plots look very much alike, but the actual values at each contour level are different. In the pair of Figs. 7.7(e) and 7.13(e), the values at each contour level are even more different. Such evidence might indicate that the internalization process may have a long time effect on the distribution of FGF-2 in the circulation.

The same phenomenon has been observed on the tube surface, as is shown in Figs. 7.14 ~ 7.18, in which the obtained results for the two cases of 4°C and 37°C are presented together for comparison purpose, for $[L]/[L_0]$, $[R]$, $[P]$, $[C]$, $[C_2]$, T , T_2 , $[G]$, $[G_2]$, $[R] + [C] + [T] + 2[C_2] + 2[T_2]$ and $[P] + [G] + [T] + 2[G_2] + 2[T_2]$, which

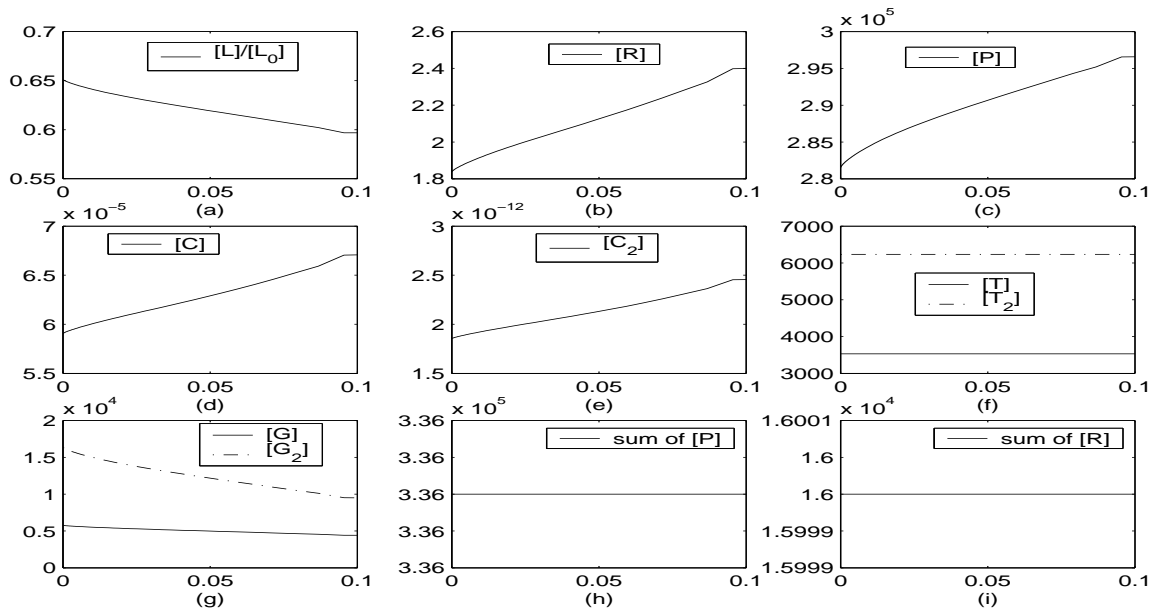
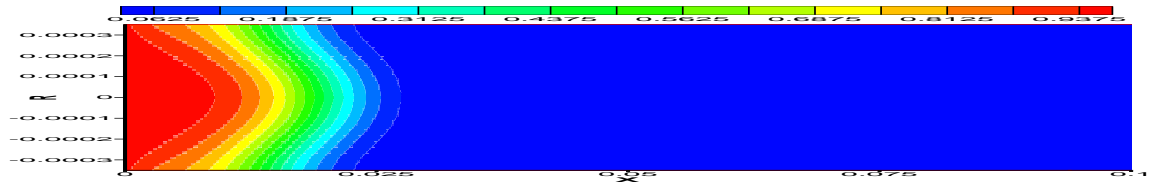
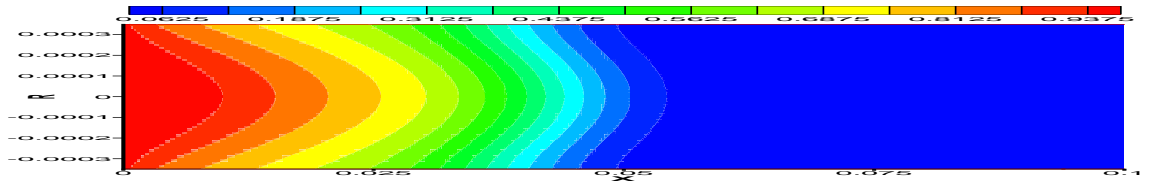


Figure 7.12: The dependency of species concentration at capillary wall on axial axis (x) at $t = 60$ minutes, (a) ligand $[L]/[L_0]$, (b) FGFR, (c) HSPG, (d) FGF-2-FGFR complex, (e) FGF-2-FGFR dimer, (f) FGF-2-FGFR-HSPG complex and its dimer, (g) FGF-2-HSPG complex and its dimer, (h) summation of $[P] + [G] + [T] + 2[G_2] + 2[T_2]$, and (i) summation of $[R] + [C] + [T] + 2[C_2] + 2[T_2]$.

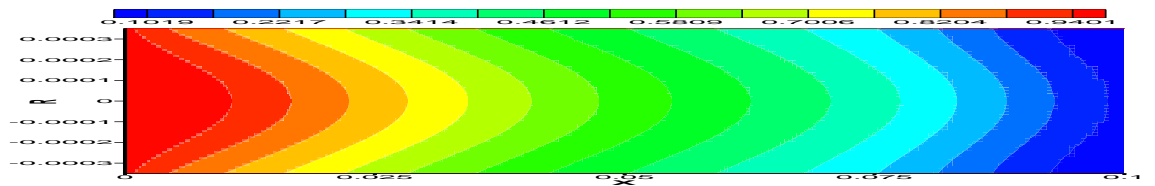
consists of eleven sub-figures. The effect of internalization can be seen more clearly by this arrangement. Consistent with what has been observed of FGF-2 distribution in the media, the concentration of FGF-2 near the tube surface does not change by introducing internalization in a short period of time, $t < 20$ minutes, shown in Figs. 7.14 and 7.15, and does change in a long time of $t > 20$ minutes, shown in Figs. 7.17 and 7.18. The populations of the two FGF-2 binding sites, FGFR (R) and HSPG (P), do not differ very much for the two cases of 4°C and 37°C at $t = 5$ and 10 minutes. No significant differences of population distribution have been observed for the bound complexes FGF-2-FGFR, FGF-2-HSPG, and FGF-2-HSPG dimer for the cases of 4°C and 37°C at $t = 5$ and $t = 10$ minutes. However, the population distribution of FGF-2-FGFR-HSPG and its dimer has changed noticeably for the two different temperature environment, at the early stage of the process, $t = 5$ and 10 minutes. Figs. 7.14 and 7.15 clearly show that for the same amount of FGF-2,



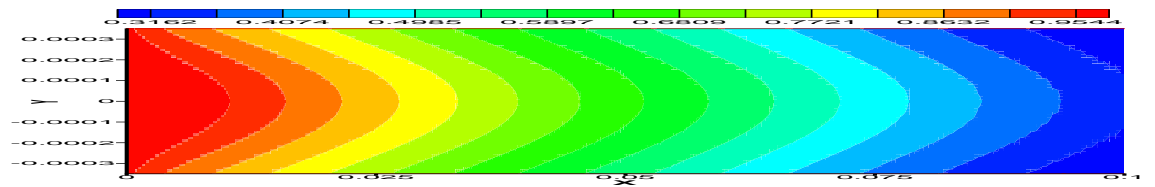
(a)



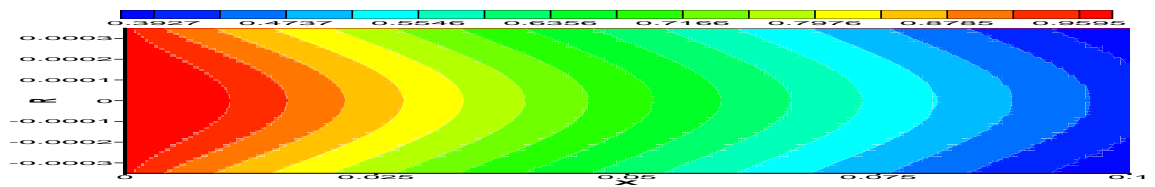
(b)



(c)



(d)



(e)

Figure 7.13: Visualization of ligand transport in the capillary at the condition of 37°C and inlet velocity $u = 0.0000866$ m/s, (a) at $t = 5$ minutes, (b) at $t = 10$ minutes, (c) at $t = 20$ minutes, (d) at $t = 40$ minutes, and (e) at $t = 60$ minutes.

FGFR, and HSPG, less amount of FGF-2-FGFR dimer, FGF-2-FGFR-HSPG and FGF-2-FGFR-HSPG dimer has been generated in the case of 37°C. This can explain why the summations of $[R] + [C] + [T] + 2[C_2] + 2[T_2]$ and $[P] + [G] + [T] + 2[G_2] + 2[T_2]$ can not be kept constant in the environment of 37°C.

The internalization of some species and its effect on the summations of $[R] + [C] + [T] + 2[C_2] + 2[T_2]$ and $[P] + [G] + [T] + 2[G_2] + 2[T_2]$ is closely related to FGF-2 distribution in the solution. Only in the region where FGF-2 has already been transported by convection and diffusion, the internalization effect can be seen. The summations of $[R] + [C] + [T] + 2[C_2] + 2[T_2]$ and $[P] + [G] + [T] + 2[G_2] + 2[T_2]$ remain constant in the region that lacks FGF-2. For the bound complexes, the concentrations of T , T_2 , G and G_2 are in the order of $10^3 \#/\text{cell}$, while the concentrations of C and C_2 are orders of magnitude lower. The impact of internalization process on components distribution is mixed. The concentrations of FGF-2-HSPG complex, FGF-2-HSPG dimer, FGF-2-FGFR-HSPG complex and FGF-2-FGFR-HSPG dimer are reduced due to internalization. The reduction can be explained by the term that describes the loss due to internalization for these components, in the ordinary differential equation system that is obtained from the mass-action kinetics. For species of FGFR, HSPG, and FGF-2-FGFR, however, their concentrations are increased by the internalization. It seems not very reasonable at the first glimpse, but after taking a close look at the corresponding model equations of the three components, the predicted increase in concentration can be interpreted by Eqs. (8.1), (8.6) and (8.2). In Eq. (8.1), one of the dominant terms is $-k_c R G$, which represents the loss of FGFR due to binding with FGF-2-HSPG to form FGF-2-FGFR-HSPG complex. Since the concentration of FGF-2-FGFR-HSPG on the surface is reduced by internalization, consequently, less FGFR is involved in binding to FGF-2-HSPG, and the concentration of FGFR is increased rather than reduced due to internalization. Eq. (8.6) governs the surface concentration of HSPG, and the dominant term is $-k_f^P L P$, which states the loss of P by binding

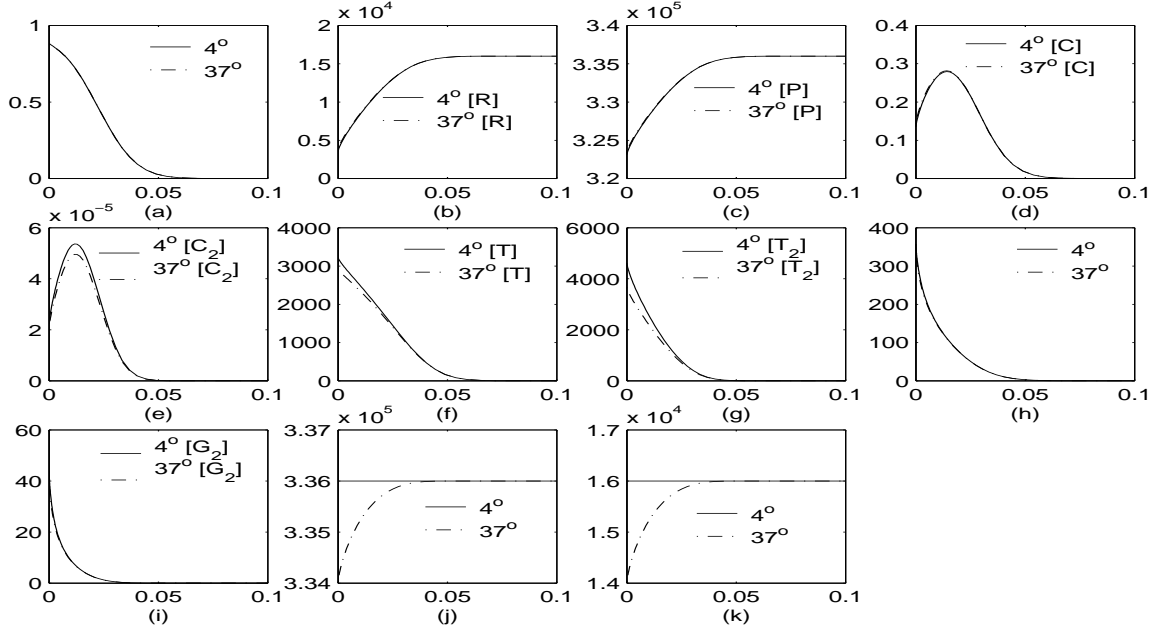


Figure 7.14: The effect of internalization on species distribution at $t = 5$ minutes, (a) ligand $[L]/[L_0]$, (b) FGFR, (c) HSPG, (d) FGF-2-FGFR complex, (e) FGF-2-FGFR dimer, (f) FGF-2-FGFR-HSPG complex, (g) FGF-2-FGFR-HSPG dimer, (h) FGF-2-HSPG complex, (i) FGF-2-HSPG dimer, (j) $[P] + [G] + [T] + 2[G_2] + 2[T_2]$, and (k) $[R] + [C] + [T] + 2[C_2] + 2[T_2]$.

with ligand to form FGF-2-HSPG. A reduced concentration of FGF-2-HSPG on the capillary surface means less HSPG loss, hence an increased concentration of P is predicted by internalization. The concentration of FGF-2-FGFR is determined by Eq. (8.2), in which $k_f^R LR$ is the dominant term. A large concentration of R results in a large concentration of C.

7.6.4 The effect of flow on ligand transport

The binding kinetics and signaling pathways of FGF-2 are very complicated, and many mathematical models have been proposed to predict the behavior of FGF-2 in fluid as well as cell surface [40, 36, 33, 29, 68, 43]. These models include pure reaction models [40, 33, 43], where a system of ordinary differential equations is provided and it is assumed that the movement of FGF-2 is not considered, and reaction-diffusion models [36, 69, 29], which are relatively more complex and the movement of FGF-

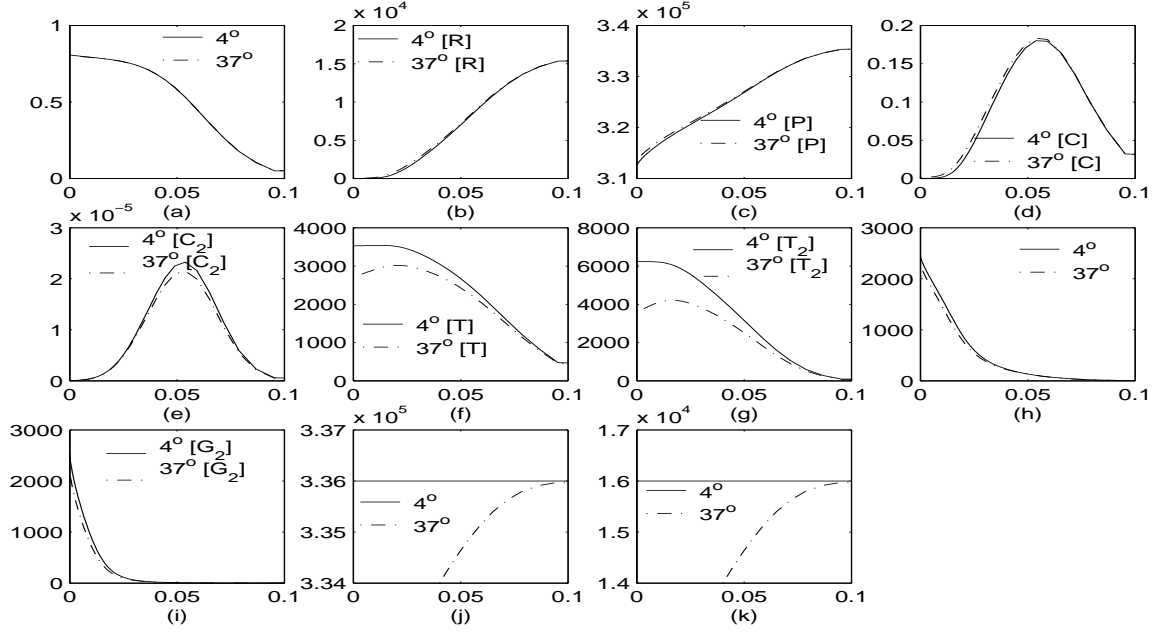


Figure 7.15: The effect of internalization on species distribution at $t = 10$ minutes, (a) ligand $[L]/[L_0]$, (b) FGFR, (c) HSPG, (d) FGF-2-FGFR complex, (e) FGF-2-FGFR dimer, (f) FGF-2-FGFR-HSPG complex, (g) FGF-2-FGFR-HSPG dimer, (h) FGF-2-HSPG complex, (i) FGF-2-HSPG dimer, (j) $[P] + [G] + [T] + 2[G_2] + 2[T_2]$ and (k) $[R] + [C] + [T] + 2[C_2] + 2[T_2]$.

2 molecules from fluid to cell surface is modeled by diffusion. Filion and Popel [36] proposed a one-dimensional diffusion-reaction model, in which FGF-2, FGF-2 dimers, soluble heparin-like glycosaminoglycans (HLGAGs), FGF-2-HLGAG compounds, and FGF-2 dimer-HLGAG compounds are located in the fluid layer. Those molecules move from fluid to cell surface by diffusion. The diffusion model is valid only if the fluid is quiescent, which is not consistent with the actual biological environment of moving bio-fluids. Our model is unique, in which a coupled convection-diffusion-reaction model is applied, and the motion of bio-fluids is fully considered.

Based on our proposed convection-diffusion-reaction model and the corresponding simulation software, the effect of bio-fluid flow on ligand transport, which has never been revealed previously, is able to be investigated systematically. As shown before, Fig. 7.13 is the time dependent concentration distribution of ligand in the capillary of flow velocity $u = 0.0000866$ m/s. Figs. 7.19 and 7.20 are the corresponding results

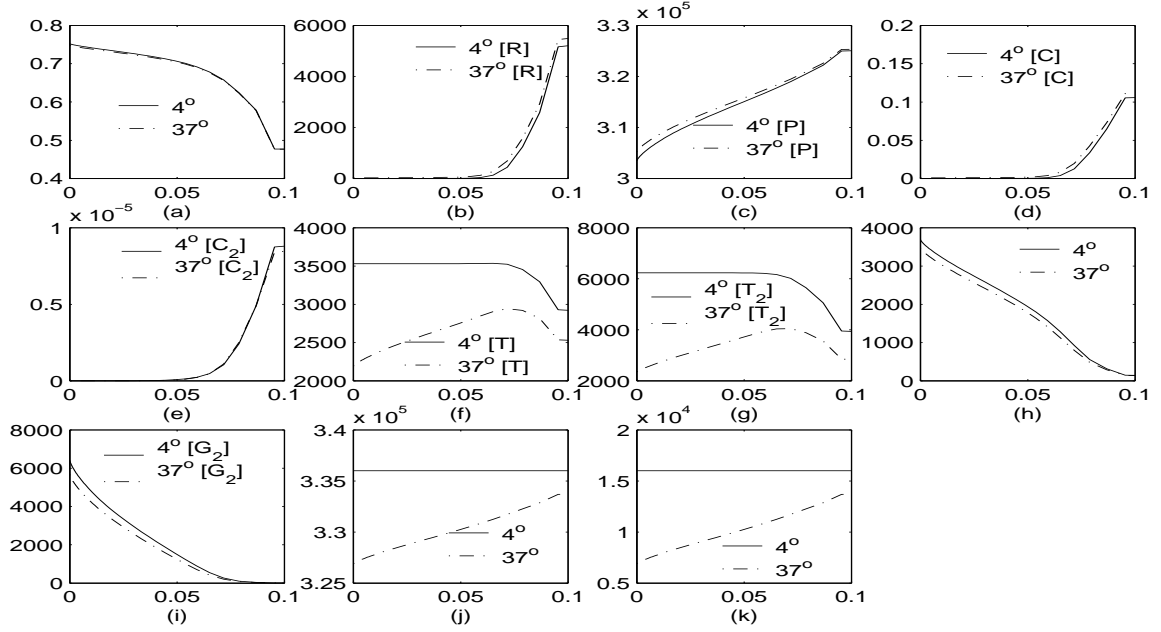


Figure 7.16: The effect of internalization on species distribution at $t = 20$ minutes, (a) ligand $[L]/[L_0]$, (b) FGFR, (c) HSPG, (d) FGF-2-FGFR complex, (e) FGF-2-FGFR dimer, (f) FGF-2-FGFR-HSPG complex, (g) FGF-2-FGFR-HSPG dimer, (h) FGF-2-HSPG complex, (i) FGF-2-HSPG dimer, (j) $[P] + [G] + [T] + 2[G_2] + 2[T_2]$, and (k) $[R] + [C] + [T] + 2[C_2] + 2[T_2]$.

when flow velocities are $u = 0.0001732$ m/s and $u = 0.00003464$ m/s, doubled and reduced to one third respectively. All these three figures display the transient concentration field of FGF-2 in capillary for the first hour after FGF-2 is added to the tube inlet. Five subfigures are included in each individual of Figs. 7.13, 7.19, and 7.20, for different time intervals, $t = 5$, $t = 10$, $t = 20$, $t = 40$, and $t = 60$ minutes. Our results clearly indicate that FGF-2 distribution is greatly affected by the flow velocity. An increased flow velocity results in high concentrations of FGF-2 on the capillary surface and at the tube exit, shown in Fig. 7.19. On the contrary, a reduced velocity lowers concentrations of FGF-2 on the capillary surface as well as tube exit, which can be seen in Fig. 7.20. If we denote high velocity $u = 0.0001732$ m/s, middle velocity $u = 0.0000866$ m/s, and low velocity $u = 0.00003464$ m/s in the three test cases, for example, at $t = 5$ minutes, FGF-2 occupies more than a half space of the capillary in high velocity case (Fig. 7.19(a)), reaches about one fourth of the tube

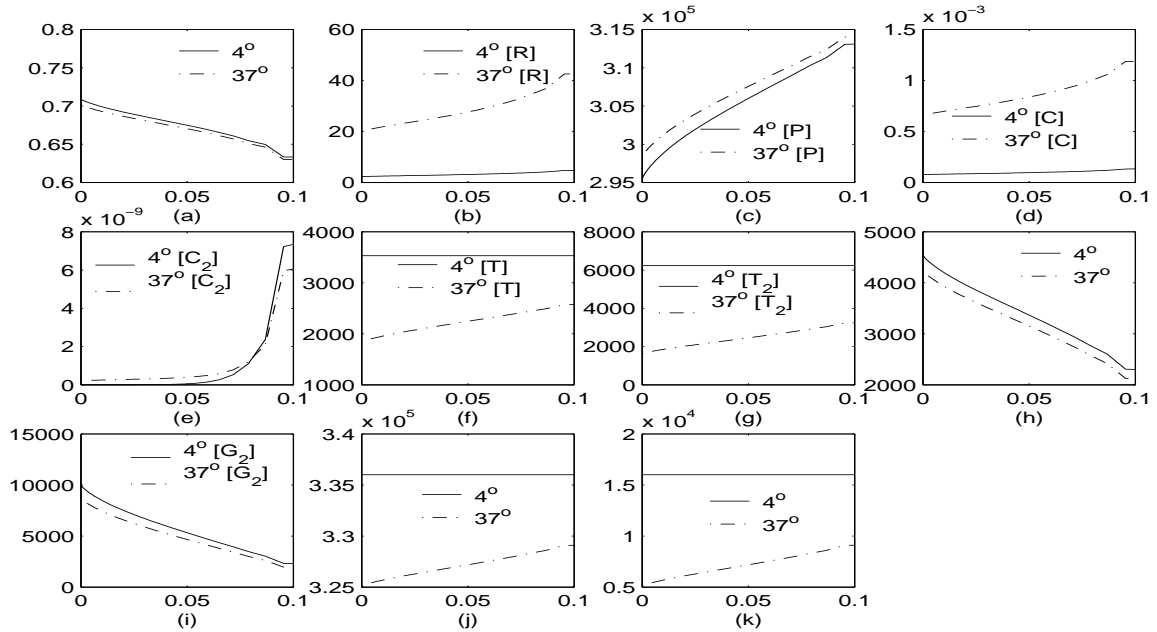


Figure 7.17: The effect of internalization on species distribution at $t = 40$ minutes, (a) ligand $[L]/[L_0]$, (b) FGFR, (c) HSPG, (d) FGF-2-FGFR complex, (e) FGF-2-FGFR dimer, (f) FGF-2-FGFR-HSPG complex, (g) FGF-2-FGFR-HSPG dimer, (h) FGF-2-HSPG complex, (i) FGF-2-HSPG dimer, (j) $[P] + [G] + [T] + 2[G_2] + 2[T_2]$, and (k) $[R] + [C] + [T] + 2[C_2] + 2[T_2]$.

space in middle velocity case (Fig. 7.13(a)), and propagates to a location less than one eighth of the tube length in the low velocity case (Fig. 7.20(a)). At $t = 60$ minutes, the normalized concentration of FGF-2 is between 0.6 and 0.7 in high velocity case, around 0.4 in middle velocity case, and less than 0.1 in the low velocity case.

7.7 Discussion

Growth factors play a very important role in modulating cell activities of proliferation and differentiation. The MAP kinase pathway starts with the growth factor ligand binding to its transmembrane receptors followed by the activation of tyrosine kinases inherent in the receptor molecules [98, 40]. Such activation triggers the dimerization and phosphorylation of the transmembrane receptors. Computational models have recently been applied to growth factor signaling systems, most of which are epidermal growth factor (EGF) systems [68, 69]. A complex model has been used by Schoeberl

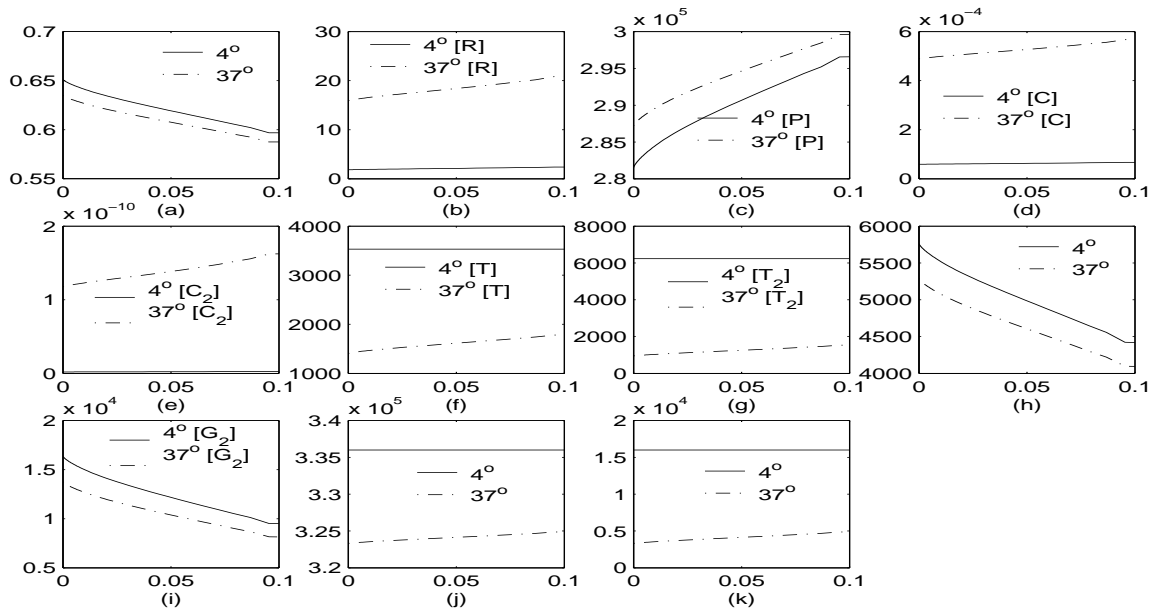
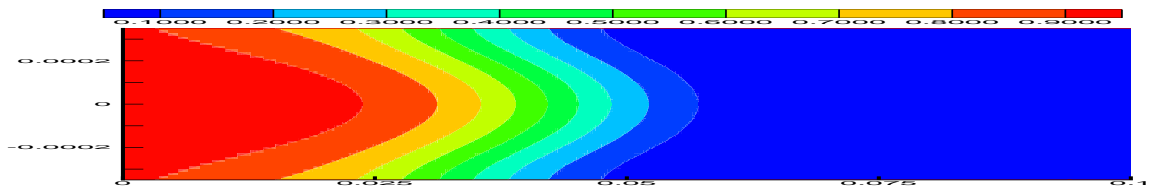
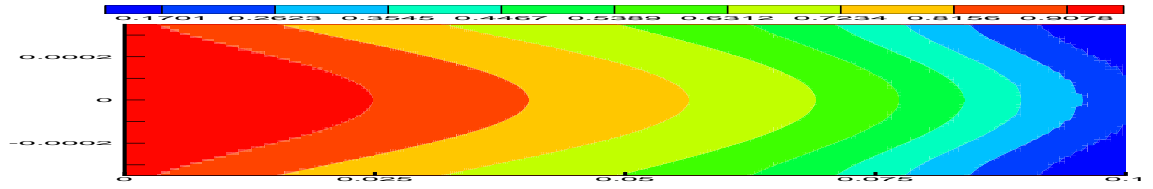


Figure 7.18: The effect of internalization on species distribution at $t = 60$ minutes, (a) ligand $[L]/[L_0]$, (b) FGFR, (c) HSPG, (d) FGF-2-FGFR complex, (e) FGF-2-FGFR dimer, (f) FGF-2-FGFR-HSPG complex, (g) FGF-2-FGFR-HSPG dimer, (h) FGF-2-HSPG complex, (i) FGF-2-HSPG dimer, (j) $[P] + [G] + [T] + 2[G_2] + 2[T_2]$, and (k) $[R] + [C] + [T] + 2[C_2] + 2[T_2]$.

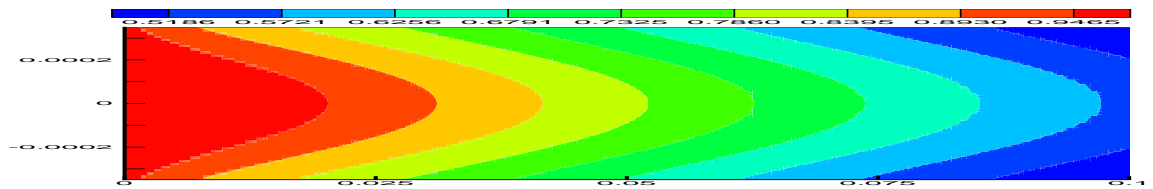
et al. [98] to study the activation of the MAP kinase signaling pathway by EGF, and intracellular signaling steps have been represented by a majority of the 94 compounds involved in the model. Complex models with up to 42 reactions have been developed by Kholodenko and collaborators [56] to interpret EGF signaling by considering downstream interconnections. In contrast, far less modeling work has been done on FGF system. Our work is focused on the modeling of extracellular binding of FGF-2 on cell surface. Forsten *et al.* [39] and Fannon *et al.* [34] have previously studied the regulation of heparin and heparin-like molecules on FGF-2 binding in solution. Filion and Popel [36] proposed a model to address the effect of FGF-2 dimerization on surface interactions. Forsten-Williams *et al.* more recently proposed a kinetic model [40], which consists of 60 reactions and 31 components including FGFR and HSPG dimerization, to investigate FGF-2 binding to heparan sulfate proteoglycans and MAP kinase signaling. That model is in a static environment where the con-



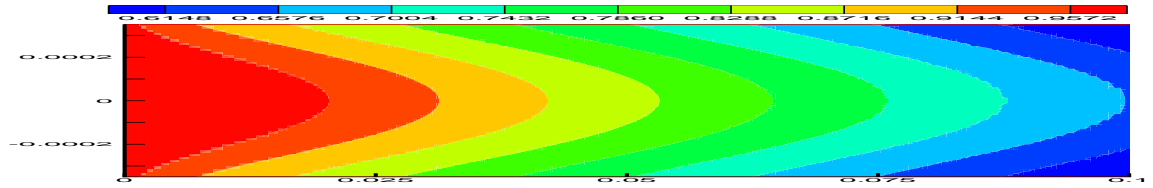
(a)



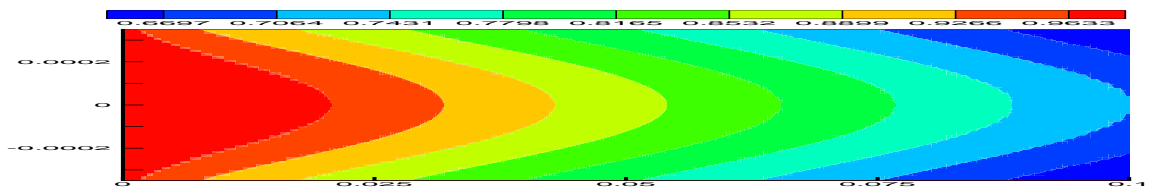
(b)



(c)

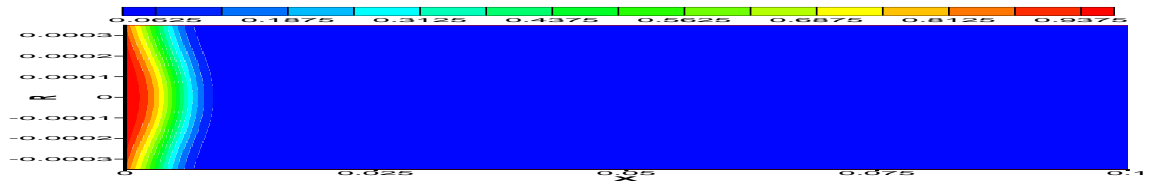


(d)

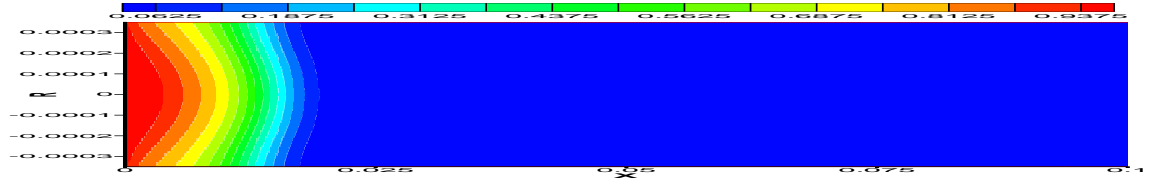


(e)

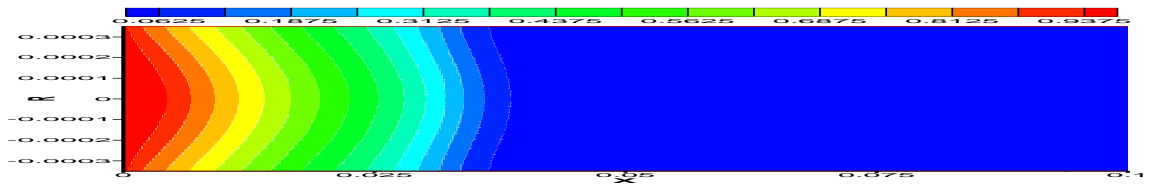
Figure 7.19: Visualization of ligand transport in the capillary at the condition of 37°C and inlet velocity $u = 0.0001732$ m/s, (a) at $t = 5$ minutes, (b) at $t = 10$ minutes, (c) at $t = 20$ minutes, (d) at $t = 40$ minutes, and (e) at $t = 60$ minutes.



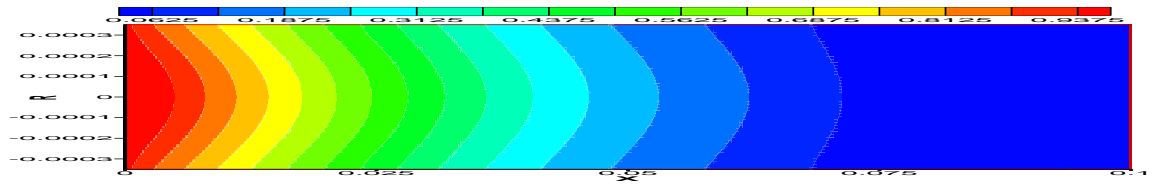
(a)



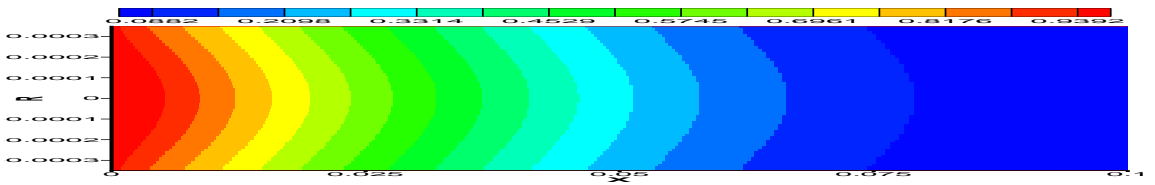
(b)



(c)



(d)



(e)

Figure 7.20: Visualization of ligand transport in the capillary at the condition of 37°C and inlet velocity $u = 0.00003464$ m/s, (a) at $t = 5$ minutes, (b) at $t = 10$ minutes, (c) at $t = 20$ minutes, (d) at $t = 40$ minutes, and (e) at $t = 60$ minutes.

concentrations of receptor ligand, receptors, HSPGs, complexes, dimers and triads are assumed to be uniformly distributed in the solution. This assumption is away from *in vivo* situation to some extent. This paper presents a dynamic model for FGF-2 binding and signaling on cell surface to include bio-fluid flow in it, and the concentrations of species are not necessarily assumed to be uniformly distributed in space. Currently we adopt the FGF-2 surface binding model proposed by Forsten et al. [40], in which dimers of FGFR or HSPG have been included as important signaling compounds. This model further assumes that the first step in high affinity dimerization is the formation of FGF-2-FGFR-HSPG triad and triads are formed by FGF-2 binding to FGFR or HSPG. The significance of dimers in signaling can be seen from their concentrations. For example, according to our computational results, the concentrations of HSPG dimers and FGF-2-FGFR-HSPG are in the order of 10^3 , which is too high to be neglected.

Our dynamic model puts FGF-2 binding and signaling in flow environment of a capillary, where FGF-2 molecules move with circulation flow inside capillary, bind to receptor and co-receptor molecules on tube surface, and signal MAP kinase pathway. Under current computation frame work, the Reynolds number is far less than the critical value for transition to turbulence, and the capillary flow is typical Hagen-Poiseuille flow with a parabolic profile, as indicated by our simulation results. The molecular motion of FGF-2 is represented by a convection-diffusion equation in macroscale in terms of concentration distribution, which is determined by media flow, diffusion coefficient of FGF-2 in media, and the rate of loss of FGF-2 due to reaction. Since the reaction rate of FGF-2 is obtained by the coupled differential system, the FGF-2 distribution in flow and the surface concentrations of receptors, complexes, dimers and triads are actually coupled. Our numerical solution reveals that the concentrations of FGF-2, FGFR, HSPG, FGF-2-FGFR, FGF-2-HSPG, FGF-2-FGFR-HSPG, FGF-2-FGFR dimer, FGF-2-HSPG dimer, and FGF-2-FGFR-HSPG dimer are indeed

location dependent. No direct results can be found in literature for simulating FGF-2 binding and signaling using a convection-diffusion-reaction model. Both experimental and computational work is required to investigate FGF-2 binding and signaling under flow condition, and our results may serve as a useful starting point.

In many cases, cell surface interactions include growth factor binding to more than a single receptor type. For example, heparin binding fibroblast growth factor-2 binds to heparan sulfate proteoglycans on the cell surface and within extracellular matrix. In this scenario, HSPG molecules have been considered accessory co-receptors serving to facilitate tyrosine kinase receptor binding [40]. Recent investigations indicate that HSPG molecules can act independently as signaling molecules besides their role as receptor binding partner [40, 20, 48]. Forsten-Williams *et al.* found in their paper [40] that HSPG played an important role in the kinetics of FGF-2 binding to FGFR and in the absence of FGFR signaling the kinetics of HSPG binding and dimerization correlated well with Erk1/2 signaling, indicating intracellular signal generated by FGF-2 binding to HSPG, an alternative receptor type. The cell signaling due to FGF-2 binding to HSPG can also be included in the current convection-diffusion-reaction model.

7.8 Summary

A novel mathematical model is proposed to reveal the dynamic interactions among FGF-2, its receptors, and HSPGs in bio-fluid. The complex model is solved by efficient PDE and ODE solvers. Numerical results shown in the chapter clearly demonstrate the significance of flow condition on FGF-2 transport, binding and signaling. Our convection-diffusion-reaction model provides a way to simulate FGF-2 binding and signaling on cell surface. A single proteoglycan species is considered in the current simulation, and more proteoglycan species can be included in the model without much effort. Dimerization of HSPG and FGFR, and internalization of HSPG, FGFR, FGF-

2-FGFR, FGF-2-HSPG, FGF-2-FGFR-HSPG and dimers of FGF-2-FGFR, FGF-2-HSPG, FGF-2-FGFR-HSPG have also been addressed in the model. Our results indicate that internalization has significant impact on the populations of binding sites and thereafter formed complexes on the tube surface, as well as FGF-2 distribution in the media. Additional experimental and computational studies are required for a better understanding of how cellular proteoglycans impact growth factor binding and signaling *in vivo* environment to achieve the goal of disease-healing by manipulating FGF-2-mediated cell activity.

8 Conclusion and Future Work

8.1 Conclusion

This dissertation presents our research work in computer modeling and simulation of physics, chemistry, and biology using deterministic dynamics. The whole simulation procedure is very complicated, which involves mathematical modeling, discretization of differential equations, solution of linear and nonlinear systems, and scientific visualization. Several typical simulation examples are discussed in the dissertation, including diffusion, convection-diffusion, and convection-diffusion-reaction problems. The dissertation work is summarized as follows.

- A mathematical model describing the thermomechanical interactions in biological bodies at high temperature is proposed by treating the soft tissue in biological bodies as a thermoporoelastic media. The heat transfer and elastic deformation in soft tissues are examined based on the Pennes bioheat transfer equation and the modified Duhamel-Neuman equations. The three dimensional governing equations based on the proposed model is discretized using a 19 point finite difference scheme. The resulting large sparse linear system is solved by a preconditioned Krylov subspace method. Numerical simulations show that the proposed model is valid under our test conditions and the proposed numerical techniques are efficient.
- Numerical experiments including hyperthermia and sinusoidal heating are conducted to investigate the heat transfer processes in soft tissues in biological bodies. We obtained the expected time-dependent temperature distribution as well as the corresponding thermal-induced mechanical responses. From the information presented in the dissertation, it is not difficult to draw a conclusion that the thermal-related mechanical properties can be modeled using the proposed method, and the technique introduced here can be used to predict

the outcome of a possible heat related medical therapy and estimate the corresponding damage to soft tissues due to high temperature exposure.

- A three-dimensional (3D) multilayer model based on the skin physical structure is developed to investigate the transient thermal response of human skin subject to laser heating. The temperature distribution of the skin is modeled by the bioheat transfer equation, and the influence of laser heating is expressed as a source term where the strength of the source is a product of a Gaussian shaped incident irradiance, an exponentially shaped axial attenuation, and a time function. The water evaporation and diffusion is included in the model by adding two terms regarding the heat loss due to the evaporation and diffusion, where the rate of water evaporation is determined based on the theory of laminar boundary layer. Cryogen spray cooling (CSC) in laser therapy is studied, as well as its effect on the skin thermal response. The time-dependent equation is discretized using the finite difference method with the Crank-Nicholson scheme and the stability of the numerical method is analyzed. The large sparse linear system resulted from discretizing the governing partial differential equation is solved by GMRES solver and expected simulation results are obtained.
- The three-dimensional multilayer model is further extended for the quantitative prediction of skin injury resulting from certain thermal exposure on the surface. The model is based on the skin damage equation proposed by Henriques and Moritz for the process of protein denaturation. Different from the standard Arrhenius model for protein damage rate, in which the activation energy includes chemical reaction only, strain energy of tissue due to thermal stress is also considered in the current model. Skin thermal response is modeled using the bioheat transfer equation by including water diffusion on the skin surface, and the corresponding thermal stress is predicted by using the modified Duhamel-

Neuman equation. Strain energy is then obtained by the stress-strain relation. The extent of burn injury is computed from the transient temperature solution and the effect of strain energy on skin damage is investigated.

- The newly-emerged vorticity-velocity formulation of the Navier-Stokes equations is used for both steady and unsteady compressible flows to avoid staggered mesh discretization. The nonlinear Navier-Stokes equations are discretized using finite difference method, and a second-order backward Euler scheme is applied for the time derivatives. Central difference is used for diffusion terms to achieve better accuracy, and a monotonicity-preserving upwind difference is used for convective ones. We use an unequal-sized single grid mesh for unsteady flow and a three level multigrid method for steady flow. The coupled nonlinear system is solved via the damped Newton's method for both steady and unsteady flows. The Newton Jacobian matrix is formed numerically, and the resulting linear system is ill-conditioned and is solved by the iterative solver Bi-CGSTAB with the Gauss-Seidel preconditioner.
- This dissertation introduces a novel convection-diffusion-reaction model to simulate fibroblast growth factor (FGF-2) binding to cell surface molecules of receptor and heparan sulfate proteoglycan and MAP kinase signaling under flow condition. This model includes three parts: the flow of media using incompressible Navier-Stokes equation, the transport of FGF-2 using a convection-diffusion transport equation, and the local binding and signaling by chemical kinetics. The whole model consists of a set of coupled nonlinear partial differential equations (PDEs) and a set of coupled nonlinear ordinary differential equations (ODEs). To solve the time-dependent PDE system, we use a second order implicit Euler method by finite volume discretization. The ODE system is stiff and is solved by an ODE solver VODE using backward differencing formulation

(BDF). The spatial distribution of FGF-2, FGFR, HSPG and their bond complexes are obtained and presented. Findings from this study have implications with regard to regulation of heparin-binding growth factors in circulation.

- Although there are many studies to investigate binding and signaling of angiogenic molecule in extracellular matrix (ECM) and on cell surface, studies on perlecan's role as a competitive binding site in the blood stream to regulate the bioavailability of other molecules are limited. At every moment a multitude of molecules are transported simultaneously and continuously by blood circulation to specific targets in the vasculature. Because of the complexity of this system, it is difficult to characterize at a macro level using in vitro or in vivo approaches alone. Computer modeling provides us with a powerful tool to test parameters and conditions, such as multiple ligand interactions in solution and on vascular surfaces under flow, which are indispensable for an accurate understanding of the underlying physiological mechanism.

8.2 Future Work

Some fundamental work has been done related to simulation and modeling of physical and biological processes. In depth research needs to be done to make the simulation as close to nature phenomenon as possible, the linear and nonlinear solver as fast and reliable as possible, and the visualization more realistic. Possible future research directions in bioheat transfer, diffusion flame, and protein transport are listed as follows.

- The simulation results presented in the dissertation are based on the assumption that the skin tissue is basically water and the heat transfer in tissue is isotropic. However, the tissue comprises of a microstructure embedded in a biofluid which is basically salt, and the preferential orientation of the collagen fibres in the dermis makes the tissue anisotropic. In other words, either the water diffusion

or the heat transfer process in the skin tissue may be anisotropic. We may investigate the anisotropic heat and mass transfer in biological tissue in the future.

- The vorticity-velocity formulation of the Navier-Stokes equations is used in the dissertation for the simulation of laminar diffusion flame, to avoid staggered grid arrangement and apply multigrid methods. However, the vorticity-velocity formulation is not straight-forward in 3D geometry and difficult to implement in applications involving irregular boundaries. We may apply the widely used pressure-based Navier-Stokes equations with colocated arrangements of variables in the future work. The colocated discretization will make the software attractive to non-orthogonal grid, complex geometry, and multigrid method with relatively easy efforts.
- Develop a multiphysics mathematical model for simulating ligand-receptor binding, dissociation and transport in blood circulation using a group of nonlinear differential equations. In the one phase model of ligand transport presented in the dissertation, we consider blood stream as a single phase, and the proteins are transported passively and their effect to blood flow is neglected. In the multiphase model, we may consider blood stream as a mixture of several phases, in which plasma is considered as the continuous phase, while protein molecules are regarded as dispersed phases. The multiphase model allows us to take a closer look at the motion of protein molecules in the blood stream and its influence on the fluid dynamic behavior of the mixture of blood and proteins. The dynamic system can be modeled by a set of partial differential equations, where each phase has its own continuity and momentum equations.
- Develop high performance computing techniques, such as high order discretization, multilevel multigrid acceleration, and efficient preconditioning to achieve

the goal of high order accuracy and low computing cost. To be specific, adaptive multilevel multigrid method can achieve high order accuracy by mesh refinement in large gradient region and low computing cost by mesh coarsening in small gradient region.

- The mathematical models and corresponding software for diffusion flame simulation and protein transport prediction in circulation are developed for 2D applications in axisymmetrical coordinates. We would like to extend the 2D codes to 3D for applications involved in complex 3D geometries, such as real combustion chambers, buildings that catch fire, blood flows in heart and lung. In such cases, the assumption of axisymmetry may not be applicable. The extension from 2D to 3D is a tedious as well as challenging work, but it will make our simulation closer to reality.
- The load of computing is very heavy for 2D applications with fine mesh, and even more burdensome for 3D applications. It may take a single workstation or PC hours, days, or weeks for a computation task. We will parallelize the code through message passing interface (MPI) libraries by the method of domain decomposition to cut the solution time. The parallel code may be run on super computers or linux clusters.

Appendix

The model system used in the current study consists of the following 9 equations, which describe the rate of components change with respect to time. This model is about the system that expresses only a single class of HSPG [40]:

$$\frac{dR}{dt} = -k_f^R LR + k_r^R C + k_r^T T - k_c RG - k_{int} R + V_R, \quad (8.1)$$

$$\frac{dC}{dt} = k_f^R LR - k_r^R C - k_c CP - k_c C^2 + 2k_{uc} C_2 - k_{int} C, \quad (8.2)$$

$$\frac{dC_2}{dt} = \frac{k_c}{2} C^2 - k_{uc} C_2 - k_{int}^D C_2, \quad (8.3)$$

$$\frac{dT}{dt} = k_c RG + K_c CP - k_r^T T - k_c T^2 + 2k_{uc} T_2 - k_{int} T, \quad (8.4)$$

$$\frac{dT_2}{dt} = \frac{k_c}{2} T^2 - k_{uc} T_2 - k_{int}^D T_2, \quad (8.5)$$

$$\frac{dP}{dt} = -k_f^P LP + k_r^P G + k_r^T T - k_c CP - k_{int} P + V_P, \quad (8.6)$$

$$\frac{dG}{dt} = k_f^P LP - k_r^P G - k_c RG - k_c G^2 + 2k_{uc} G_2 - k_{int} G, \quad (8.7)$$

$$\frac{dG_2}{dt} = \frac{k_c}{2} G^2 - k_{uc} G_2 - k_{int} G_2, \quad (8.8)$$

$$V \frac{dL}{dt} = -k_f^R LR + k_r^R C + k_r^T T - k_f^P LP - k_r^R G, \quad (8.9)$$

where L is FGF-2, R is FGFR, C is FGF-2-FGFR complex, P is HSPG, G is FGF-2-HSPG complex, T is FGF-2-FGFR-HSPG complex, C_2 is FGF-2-FGFR dimer, G_2 is FGF-2-HSPG dimer, and T_2 is FGF-2-FGFR-HSPG dimer.

Bibliography

- [1] G. Aguilar, B. Choi, J. A. Viator, D. Anderson, and J. S. Nelson, Experimental study of multiple-intermittent cryogen spurts and laser pulses for the treatment of port wine stain birthmarks. *IEEE Transactions on Biomedical Engineering*, **50**, 863-869, 2003.
- [2] G. Aguilar, S. H. Díaz, E. J. Lavernia, and J. S. Nelson, Cryogen spray cooling efficiency: improvement of port wine stain laser therapy through multiple-intermittent cryogen spurts and laser pulses. *Lasers in Surgery and Medicine*, **31**, 27-35, 2002.
- [3] D. A. Anderson, J. C. Tannehill, and R. H. Pletcher, *Computational Fluid Mechanics and Heat Transfer*, Hemisphere Publishing Corporation, Washington, 1984.
- [4] R. R. Anderson and J. A. Parrish, Selective photothermolysis: precise microsurgery by selective absorption of pulsed radiation. *Science*, **220**(4596), 524-527, 1983.
- [5] R. R. Anderson and J. A. Parrish, Microvasculature can be selectively damaged using dye lasers: a basic theory and experimental evidence in human skin. *Lasers in Surgery and Medicine*, **1**, 263-276, 1981.
- [6] D. Arora, M. Skliar, R. B. Roemer, Model-predictive control of hyperthermia treatments, *IEEE Trans. Biomed. Eng.*, **49**, 629-639, 2002.
- [7] P. D. Ballyk, D. A. Steinman, and C. R. Ethier, Simulation of non-Newtonian blood flow in an end-to-end anastomosis, *Biorheology*, **31**(5), 565-586, 1994.
- [8] J. K. Bell and P. Colella and H. M. Glaz, A Second-Order Projection Method for Incompressible Navier-Stokes Equations, *Journal of Computational Physics*, **85** (2), 257-283, 1989.
- [9] J. K. Bell and D. L. Marcus, A Second-Order Projection Method for Variable-Density Flows, *Journal of Computational Physics*, **101** (2), 334-348, 1992.
- [10] B. A. V. Bennett and M. D. Smooke, Local Rectangular Refinement with Application to Axisymmetric Laminar Flames, *Combust. Theory Modelling*, **2** (3), 221-258, 1998.
- [11] B. A. V. Bennett and M. D. Smooke, Unsteady Axisymmetric Laminar Diffusion Flames: an Application of Local Rectangular Refinement, *Eastern States Section of the Combustion Institute, Technical Meeting*, 332-335, Combustion Institute, 2001.
- [12] P. N. Brown, G. D. Byrne, and A. C. Hindmarsh, VODE: A variable coefficient ODE solver, *SIAM J. Sci. Stat. Comput.*, **10**, pp. 1038-1051, 1989.

- [13] T. D. Brown, Techniques for mechanical stimulation of cells in vitro: a review, *J. Biomech.*, **33**, pp. 3-14, 2000.
- [14] G. R. Buchanan, *Theory and Problems of Finite Element Analysis*, Schaum's Outline Series, McGraw-Hill, New York, NY, 1995.
- [15] S. P. Burke and T. E. W. Schumann, Diffusion Flames, *Industrial and Engineering Chemistry*, **20** (10), 998-1004, 1928.
- [16] J. R. Cebal and R. Löhner, Efficient simulation of blood flow past complex endovascular devices using an adaptive embedding technique, *IEEE Transactions on Medical Imaging*, **24**(4), 468-476, 2005.
- [17] D. R. Chapman, Computational Aerodynamics Development and Outlook, *AIAA Journal*, **17**, 1293-1313, 1979.
- [18] M. M. Chen and K. R. Holmes, Microvascular contributions in tissue heat transfer, in *Thermal Characteristics of Tumors: Applications in Detection and Treatment (Ann. New York Academy of Sciences, Vol. 335) (New York: Academy of Sciences)*, 137-150, 1980.
- [19] Y. I. Cho and K. R. Kenney, Effects of the non-Newtonian viscosity of blood on flows in a diseased arterial vessel, Part I: steady flows, *Biorheology*, **28**, 241-262, 1991.
- [20] C. C. Chua, N. Rahimi, K. Forsten-Williams, M. A. Nugent, Heparan sulfate proteoglycans function as receptors for fibroblast growth factor-2 activation of extracellular signal-regulated kinases 1 and 2, *Circulation Research*, **94**, pp. 316-323, 2004.
- [21] M. P. Cleary, Fundamental solutions for a fluid-saturated porous solid, *Int. J. Solids Structures*, **13**, 785-806, 1977.
- [22] P. Colella and P. R. Woodward, The piecewise parabolic method (PPM) for gas-dynamical simulation, *Journal of Computational Physics*, **54**, 174-201, 1984.
- [23] T. Dai, B. M. Pikkula, J. W. Tunnell, D. W. Chang, and B. Anvari, Thermal response of human skin epidermis to 595-nm laser irradiation at high incident dosages and long pulse durations in conjunction with cryogen spray cooling: an ex-vivo study. *Lasers in Surgery and Medicine*, **33**, 16-24, 2003.
- [24] C. P. van Dam and M. Hafez and J. Ahmad, Calculations of Viscous Flow with Separation Using Newton's Method and Direct Solver, *AIAA Journal*, **28** (5), 937-939, 1990.
- [25] Z. S. Deng and J. Liu, Analytical study on bioheat transfer problems with spatial or transient heating on skin surface or inside biological bodies, *ASME J. Biomech. Eng.*, **124**, 638-649, 2002.

- [26] T. Deschamps, P. Schwartz, D. Trebotich, P. Colella, D. Saloner, and R. Maladi, Vessel segmentation and blood flow simulation using level-set and embedded boundary methods, *International Congress Series*, **1268**, 75-80, 2004.
- [27] L. B. Director, S. E. Frid, V. Y. Mendeleev, and S. N. Scovorod'ko, Computer simulation of heat and mass transfer in tissue during high-intensity long-range laser irradiation, *Annals New York Academy of Sciences*, **858**, 56-65, 1998.
- [28] C. C. Douglas and A. Ern and M. D. Smooke, Numerical Simulation of Flames Using Multigrid Methods, *IMACS Series in Computational and Applied Mathematics*, **4**, 149-154, 1998.
- [29] C. J. Dowd, C. L. Cooney, and M. A. Nugent, Heparan sulfate mediates bFGF transport through basement membrane by diffusion with rapid reversible binding. *The Journal of Biological Chemistry*, **274**, No. 8, pp. 5236-5244, 1999.
- [30] J. W. Durkee Jr. and P. P. Antich, Exact solutions to the multi-region time-dependent bioheat equation with transient heat sources and boundary conditions, *Phys. Med. Biol.*, **36**, 345-368, 1991.
- [31] A. Ern, *Vorticity-Velocity Modeling of Chemically Reacting Flows*, PhD Thesis, Yale University, New Haven, Connecticut, 1994.
- [32] M. Fannon and M. A. Nugent, Basic fibroblast growth factor binds its receptors, is internalized, and stimulates DNA synthesis in Balb/c3T3 cells in the absence of heparan sulfate. *J. Biol Chem*, **271**, 17949-17956, 1996.
- [33] M. Fannon, K. E. Forsten, and M. A. Nugent, Potentiation and inhibition of bFGF binding by heparin: a model for regulation of cellular response, *Biochemistry*, **39**(6), 1434-1445, Feb 2000.
- [34] M. Fannon, K. Forsten-Williams, C. J. Dowd, D. A. Freedman, J. Folkman, and M. A. Nugent, Binding inhibition of angiogenic factors by heparan sulfate proteoglycans in aqueous humor: potential mechanism for maintenance of an avascular environment. *The FASEB Journal*, **17**, pp. 902-904, 2003.
- [35] J. H. Ferziger and M. Perić, *Computational Methods for Fluid Dynamics*, Springer, Berlin, Germany, 1999.
- [36] R. J. Fillion, A. S. Popel, A reaction-diffusion model of basic fibroblast growth factor interactions with cell surface receptors, *Annals of Biomedical Engineering*, **32**, 645-663, 2004.
- [37] J. Folkman, R. Langer, R. J. Linhardt, C. Haudenschild, and S. Taylor, Angiogenesis inhibition and tumor regression caused by heparin or a heparin fragment in the presence of cortisone. *Science*, **221**, pp. 719-725, 1983.
- [38] K. E. Forsten, and D. A. Lauffenburger, Probability of autocrine ligand capture by cell-surface receptors: implications for ligand secretion measurements. *J. Comp. Bio.*, **1**, pp. 15-23, 1994.

- [39] K. E. Forsten, M. Fannon, and M. A. Nugent, Potential mechanisms for the regulation of growth factor binding by heparin. *J. Theor. Biol.*, **205**, pp. 215-230, 2000.
- [40] K. Forsten-Williams, C. C. Chua, and M. A. Nugent, The kinetics of FGF-2 binding to heparan sulfate proteoglycans and MAP kinase signaling. *Journal of Theoretical Biology*, **233**, pp. 483-499, 2005.
- [41] Y. C. Fung, *Biomechanics Mechanical Properties of Living Tissues*, Springer-Verlag, New York, 1981.
- [42] Y. C. Fung, *Foundations of Solid Mechanics*, Prentice-Hall, New Jersey, 1965.
- [43] F. M. Gabhann, M. T. Yang, and A. S. Popel, Monte Carlo simulations of VEGF binding to cell surface receptors in vitro. *Biochimica et Biophysica Acta*, **1746**, 95-107, 2005.
- [44] M.J.C. van Gemert, G.W. Lucassen, and A.J. Welch, Time constants in thermal laser medicine: II. distributions of time constants and thermal relaxation of tissue. *Phys. Med. Biol.*, **41**, 1381-1399, 1996.
- [45] H. C. Hardee and D. O. Lee, A simple conduction model for skin burns resulting from exposure to chemical fireballs, *Fire Research*, **1**, 199-205, 1977/78.
- [46] F. C. Henriques and A. R. Moritz, Studies of thermal injury, I: the conduction of heat to and through skin and the temperatures attained therein, a theoretical and experimental investigation, *Amer. J. Pathol.*, **23**, 531-549, 1947.
- [47] K. Hisatake, S. Tanaka, and Y. Aizawa, Evaporation rate of water in a vessel, *J. Appl. Phys.*, **73**, 7395-7401, 1993.
- [48] A. Horowitz, E. Tkachenko, and M. Simons, Fibroblast growth factor-specific modulation of cellular response by syndecan-4, *Journal of Cell Biology*, **157**, pp. 715-725, 2002.
- [49] F. P. Incropera and D.P. Dewitt, *Fundamentals of Heat and Mass Transfer*, 4th Edition, John Wiley & Sons, 1996.
- [50] L. M. Jiji, S. Weinbaum, and D. E. Lemons, Theory and experiment for the effect of vascular microstructure on surface tissue heat transfer—part II: model formulation and solution, *ASME J. Biomech. Eng.*, **106**, 331-341, 1984.
- [51] B. M. Johnson, P. R. Johnston, S. Corney, and D. Kilpatrick, Non-Newtonian blood flow in human right coronary arteries: steady state simulations, *Journal of Biomechanics*, **37**, 709-720, 2004.
- [52] J. Niamtu, Clinical applications of the 532-nm Diode Laser for the treatment of facial telangiectasia and pigmented lesions: literature review, history, and discussion of clinical experience. *The American Journal of Cosmetic Surgery*, **18(2)**, 71-81, 2001.

- [53] S. Karaa and J. Zhang and C. C. Douglas, Preconditioned Multigrid Simulation of an Axisymmetric Laminar Diffusion Flame, *Math. Comput. Modeling*, **38**, 269-279, 2003.
- [54] S. Karaa, J. Zhang, and F. Yang, A numerical study of a 3D bioheat transfer problem with different spatial heating, *Mathematics and Computers in Simulation*, **68(4)**, 375-388, 2005.
- [55] C. T. Kelley, *Iterative Methods for Linear and Nonlinear Equations*, SIAM, Philadelphia, 1995.
- [56] B. N. Kholodenko, O. V. Demin, G. Moehren, and J. B. Hoek, Quantification of short term signaling by the epidermal growth factor receptor, *Journal of Biological Chemistry*, **274**, 30169-30181, 1999.
- [57] D. A. Knoll and D. E. Keyes, Jacobian-Free Newton-Krylov Methods: a Survey of Approaches and Applications, *Journal of Computational Physics*, **193** (2), 357-397, 2004.
- [58] M. E. Kowalski, J. M. Jin, Model-order reduction of nonlinear models of electromagnetic phased-array hyperthermia, *IEEE Trans. Biomed. Eng.*, **50**, 1243-1254, 2003.
- [59] S. J. Kowalski, Thermomechanics of the drying process of fluid-saturated porous media, *Drying Technology*, **12**, 453-482, 1994.
- [60] J P Ku, M T Draney, F R Arko, W A Lee, F P Chan, N J Pelc, C K Zarins, and C A Taylor, *In vivo* validation of numerical prediction of blood flow in arterial bypass grafts, *Annals of Biomedical Engineering*, **30**, 743-752, 2002.
- [61] J. W. Lee, K. S. Kim, S. M. Lee, S. J. Eom, and R. V. Troitsky, A novel design of thermal anomaly for mammary gland tumor phantom for microwave radiometer, *IEEE Trans. Biomed. Eng.*, **49**, 694-699, 2002.
- [62] R. LeVeque, *Finite Volume Methods for Hyperbolic Problems*, Cambridge University Press, Cambridge, UK, 2002.
- [63] D. R. Lide, Editor-in-Chief, Handbook of Chemistry and Physics, 74th Edition, CRC Press, Boca Raton, 6-10, 1993.
- [64] D. R. Lide, Editor-in-Chief, Handbook of Chemistry and Physics, 74th Edition, CRC Press, Boca Raton, 6-15, 1993.
- [65] D. R. Lide, Editor-in-Chief, Handbook of Chemistry and Physics, 74th Edition, CRC Press, Boca Raton, 6-203, 1993.
- [66] J. Liu, Uncertainty analysis for temperature prediction of biological bodies subject to randomly spatial heating, *J. Biomechan.*, **34**, 1637-1642, 2001.

- [67] J. Liu and L. X. Xu, Estimation of blood perfusion using phase shift in temperature response to sinusoidal heating at skin surface, *IEEE Trans. Biomed. Eng.*, **46**, 1037-1043, 1999.
- [68] M. A. Lovich and E. R. Edelman, Computational simulations of local vascular heparin deposition and distribution. *American Journal of Physiology*, **275** (*Heat and Circulatory Physiology*), **40**, pp. H2014-2024, 1996.
- [69] M. A. Lovich, M. Philbrook, S. Sawyer, E. Weselcouch, and E. R. Edelman, Arterial heparin deposition: role of diffusion, convection, and extravascular space. *American Journal of Physiology*, **275** (*Heat and Circulatory Physiology*), **44**, pp. H2236-2242, 1998.
- [70] D. J. Maitland, D. D. Eder, R. A. London, M. E. Glinsky, and B. A. Soltz, Dynamics simulations of tissue welding, Proceedings of Lasers in Surgery: Advanced Characterization, Therapeutics, and Systems VI, R. Rox Anderson, M.D., Editor, Proc. SPIE **2671**, 234-242, 1996.
- [71] Manuel, FiberCell Systems, Inc. <http://www.fibercellsystems.com>.
- [72] R. K. Mohammed and M. A. Tanoff and M. D. Smooke and A. M. Schaffer Computational and Experimental Study of a Forced, Time-Varying, Axisymmetric, Laminar Diffusion Flame, twenty-Seventh Symposium (International) on Combustion/The Combustion Institute, 693-702, Combustion Institute, 1998.
- [73] A. R. Moritz and F. C. Henriques, Studies of thermal injury II: the relative importance of time and surface temperature in the causation of cutaneous burns. *American Journal of Pathology*, **23**, 695-720, 1947.
- [74] C. A. Nanni and T. S. Alster, Complications of cutaneous laser surgery. A review. *Dermatol Surg.*, **24**(2), 209-219, 1998.
- [75] E. Y. Ng and L. T. Chua, Prediction of skin burn injury. Part 1: numerical modeling. *Proc Instn Mech Engrs, Part H: J Engineering in Medicine*, **216**, 157-170, 2002.
- [76] J. W. Nichols, *Simulation and Stability Analysis of Jet Diffusion Flames*, PhD Thesis, University of Washington, Seattle, Washington, 2005.
- [77] M. Noskov, *An Implicit Compact Scheme Solver for Modeling Steady-State and Time-Dependent Axisymmetric Flows with Application to Laminar Diffusion Flame Simulations* PhD Thesis, Yale University, New Haven, Connecticut, 2003.
- [78] P. J. Orchard, C. M. Smith, 3rd, W. G. Woods, D. L. Day, L. P. Dehner, and R. Shapiro, Treatment of hemangi endotheliomas with alpha interferon, *Lancet*, **2**, 565-567, 1989.
- [79] M. J. Ott and B. J. Ballermann, Shear stress-conditioned, endothelial cell-seeded vascular grafts: improved cell adherence in response to in vitro shear stress, *Surgery*, **117**, pp. 334-339, 1995.

- [80] K. R. Pardasani and V. P. Saxene, Temperature distribution in skin with uniformly perfused tumor in subdermal tissues, *Biomechanics*, Editors: K.B. Sahay and R. K. Saxena, John Wiley & Sons, 1989.
- [81] S. V. Patankar, *Numerical Heat Transfer and FluidFlow*, The McGraw-Hill Company, Inc., New York, 1980.
- [82] A. T. Patera, B. B. Mikic, G. Eden, and H. F. Bowman, Prediction of tissue perfusion from measurement of the phase shift between heat flux and temperature, *Winter Annual Meeting of ASME, Advances in Bioengineering*, 187-191, 1979.
- [83] P. B. Pember and L. H. Howell and J. H. Bell and P. Colella and C.Y. Crutchfield and W.A. Fivel and J.P. Jessee, An Adaptive Projection Method for Unsteady, Low-Mach Number Combustion, *Combust. Sci. Tech.*, **140**, 123-168, 1998.
- [84] M. Pelikan *Hierarchical Bayesian Optimization Algorithm: toward a new generation of evolutionary algorithms*, Springer, 2005.
- [85] H. H. Pennes, Analysis of tissue and arterial blood temperatures in resting human forearm, *J. Appl. Physiol.*, **1**, 93-122, 1948.
- [86] K. Perktold and G. Rappitsch, Computer simulation of local blood flow and vessel mechanics in a compliant carotid artery bifurcation model, *Journal of Biomechanics*, **28**, 845-856, 1995.
- [87] D. M. Price, Modulated-temperature thermomechanical analysis, *J. Therm. Anal.*, **51**, 231-236, 1998.
- [88] A. Rabbits, N. E. Alden, G. O'Sullivan, G. J. Bauer, P. Q. Bessey, J. R. Turkowski, and R. W. Yurt, Firefighter burn injuries: A 10-year longitudinal study. *J. Burn Care Rehab.*, **25**, 430-434, 2004.
- [89] B. B. Riley, M. P. Savage, B. K. Simandl, B. B. Olwin, and J. F. Fallon, Retroviral expression of FGF-2 (bFGF) affects patterning in chick limb bud, *Development*, **118**, 95-104, 1993.
- [90] P. Roe, Approximate Riemann Solvers, Parameter Vectors and Difference Schemes, *Journal of Computational Physics*, **27**, 1-31.
- [91] R. B. Roemer, Engineering aspects of hyperthermia therapy, in *Annual Review of Biomedical Engineering*, M. L. Yarmush, K. R. Killer, and M. Toner, Eds., Palo Alto, CA, Annual Reviews, 347-376, 1999.
- [92] Y. Saad and M. H. Schultz, GMRES: a generalized minimal residual algorithm for solving nonsymmetric linear systems, *SIAM J. Sci. Stat. Comput.*, **7**, 856-869, 1986.
- [93] Y. Saad, ILUT: a dual threshold incomplete LU preconditioner. *Numer. Linear Algebra Appl.*, **1**, 387-402, 1994.

- [94] Y. Saad, *Iterative Methods for Sparse Linear Systems*, PWS Pub., New York, 1996.
- [95] J. R. Saffle, B. Davis, and P. Williams, Recent outcomes in the treatment of burn injury in the United States: A report from the American Burn Association Patient Registry, *J. Burn Care Rehab.*, **16**, 219-232, 1995.
- [96] M. T. A. Saif, B. E. Alaca, and H. Sehitoglu, Analytical modeling of electrostatic membrane actuator for micro pumps, *IEEE Journal of Microelectromechanical System*, **8(3)**, 335-345, 1999.
- [97] R. J. Scheuplein, I. H. Blank, Permeability of the skin, *Physiol. Rev.*, **51**, 702-747, 1971.
- [98] B. Schoeberl, C. Eichler-Jonsson, E. D. Gilles, and G. Muller, Computational modeling of the dynamics of the MAP kinase cascade activated by surface and internalized EGF receptors, *Nature Biotechnology*, **20**, 370-375, 2002.
- [99] N. Shahcheraghi, H. A. Dwyer, A. Y. Cheer, A. I. Barakat, and T. Rutaganira, Unsteady and three-dimensional simulation of blood flow in the human aortic arch, *Transactions of ASME Journal of Biomedical Engineering*, **124**, 378-387, 2002.
- [100] W. Shen and S. Han, Numerical solution of two-dimensional axisymmetric hyperbolic heat conduction. *Computational Mechanics*, **29**, 122-128, 2002.
- [101] W. Shen, J. Zhang, and F. Yang, Modeling and numerical simulation of bioheat transfer and biomechanics in soft tissue, *Mathematical and Computer Modelling*, **41(11-12)**, 1251-1265, 2005.
- [102] W. Shen and J. Zhang, Newton's method for steady and unsteady reacting flows, *Proceedings of the 2006 ACM Symposium of Applied Computing*, ACM, Melbourne, FL, 2006, pp. 756-757.
- [103] W. Shen, J. Zhang, and F. Yang, Performance of ILUT preconditioners in modeling bioheat and mass transfer in skin thermal injury, *Proceedings of the Third M.I.T. Conference on Computational Fluid and Solid Mechanics*, editor: K.J. Bathe, 1175-1178, Elsevier, 2005.
- [104] W. Shen, J. Zhang, and F. Yang, Three-dimensional model of thermal response of skin subject to laser heating. *Computer Methods in Biomechanics and Biomedical Engineering*, **8(2)**, 115-125, 2005.
- [105] W. Shen, C. Zhang, and J. Zhang, Multiscale simulation of ligand-receptor binding and dissociation in circulation, *Proceedings The 45th ACM Southeast Conference*, March 23-24, 2007, ACM, Winston-Salem, NC, 2007, pp. 519-520.
- [106] C.-W. Shu, High-order Finite Difference and Finite Volume WENO Schemes and Discontinuous Galerkin Methods for CFD, *International Journal of Computational Fluid Dynamics*, **17 (2)**, pp. 107-118.

- [107] M. A. Singer and S. B. Pope, Exploiting ISAT to solve the reaction-diffusion equation, *Combustion Theory and Modelling*, **8**, 361-383, 2004.
- [108] A. N. Skempton, The pore pressure coefficients A and B, *Geotechnique*, **4**, 143-147, 1954.
- [109] J. M. Smith, *Mathematical Modeling and Digital Simulation for Engineers and Scientists*, John Wiley & Sons, New York, 1987.
- [110] M. D. Smooke and R. E. Mitchell and D. E. Keyes, Numerical Solution of Two-Dimensional Axisymmetric Laminar Diffusion Flames, *Combust. Sci. Tech.*, **67**, 85-122, 1989.
- [111] G. A. Sod, *Numerical Methods in Fluid Dynamics*, Cambridge University Press, New York, 1985.
- [112] G. V. Sperinde and M. A. Nugent, Heparan sulfate proteoglycans control bFGF processing in vascular smooth muscle cells. *Biochemistry*, **37**, pp. 13153-13164, 1998.
- [113] A. M. Stoll and L. C. Green, Relationship between pain and tissue damage due to thermal radiation, *Journal of Applied Physiology*, **14**, 373-382, 1959.
- [114] H. L. Stone, Iterative Solution of Implicit Approximations of Multidimensional Partial Differential Equations, *SIAM J. Numer. Anal.*, **5**, pp. 530-558, 1968.
- [115] L. O. Svaasand, L. L. Randeberg, G. Aguilar, B. Majaron, S. Kimel, E. J. Lavernia, and J. S. Nelson, Cooling efficiency of cryogen spray during laser therapy of skin. *Lasers in Surgery and Medicine*, **32**, 137-142, 2003.
- [116] P. K. Sweby, High Resolution Schemes Using Flux Limiters for Hyperbolic Conservation Laws, *SIAM Journal of Numerical Analysis*, **21** (5), 995-1011, 1984.
- [117] H. S. Tharp and R. B. Roemer, Optimal power deposition with finite-sized, planar hyperthermia applicator arrays, *IEEE Trans. Biomed. Eng.*, **39**, 569-579, 1992.
- [118] T. S. Alster, Review of cutaneous lasers and their applications. *Southern Medical Journal*, **91**(9), 806-814, 1998.
- [119] J. H. Torres, M. Motamedi, J. A. Pearce, and A. J. Welch, Experimental evaluation of mathematical models for predicting the thermal response of tissue to laser irradiation, *Appl. Opt.*, **32**, 597-606, 1993.
- [120] D. A. Torvi and J.D. Dale, A finite element model of skin subject to a flash fire. *ASME Tran. J. of Biomechanical Engineering*, **116**, 250-255, 1994.

- [121] S. Tungjitkusolmun, S. T. Staelin, D. Haemmerich, J. Z. Tsai, H. Gao, J. G. Webster, F. T. Lee, Jr., D. M. Mahvi, and V. R. Vorperian, Three-dimensional finite-element analyses for radio-frequency hepatic tumor ablation, *IEEE Trans. Biomed. Eng.*, **49**, 3-9, 2002.
- [122] B. Van Leer, Towards the ultimate conservative difference schemes, V: A second order sequel to Godunov's method, *Journal of Computational Physics*, **43**, 357-372, 1981.
- [123] H. A. van der Vorst, Bi-CGSTAB: a Fast and Smoothly Converging Variant of Bi-CG for the Solution of Nonsymmetric Linear Systems, *SIAM J. Sci. Statist. Comput.*, **13** (2), 631-644.
- [124] A. Vanne and K. Hynynen, MRI feedback temperature control for focused ultrasound surgery. *Phys. Med. Biol.*, **48**, 31-43, 2003.
- [125] V. Venkatakrishnan, Newton Solution of Inviscid and Viscous Problems, *AIAA Journal*, **27** (7), 885-891, 1989.
- [126] W. Verkruysse, B. Majaron, G. Aguilar, L.O. Svaasand, and J. S. Nelson, Dynamics of cryogen deposition relative to heat extraction rate during cryogen spray cooling, *ProcSPIE*, **3907**, 37-48, 2000.
- [127] C. A. Walsh, H. K. D. H. Bhadeshia, A. Lau, B. Matthias, R. Oesterlein, and J. Drechsel, Characteristics of high-power diode-laser welds for industrial assembly *Journal of Laser Applications*, **19**, 68-76, 2003.
- [128] J. Warnatz, U. Maas, and R. W. Dibble, *Combustion Physical and Chemical Fundamentals, Modeling and Simulation, Experiments, Pollutant Formation*, Springer, Berlin, 2001.
- [129] S. Weinbaum, L. M. Jiji, and D. E. Lemons, Theory and experiment for the effect of vascular microstructure on surface tissue heat transfer—part I: anatomical foundation and model conceptualization, *ASME J. Biomech. Eng.*, **106**, 321-330, 1984.
- [130] A. J. Welch, The thermal response of laser irradiated tissue, *IEEE Journal of Quantum Electronics*, **QE-20**, 1471-1481, 1984.
- [131] J. R. Welty, C. E. Wicks, R. E. Wilson, and G. L. Rorrer, *Fundamentals of Momentum, Heat, and Mass Transfer*, 4th Edition, John Wiley & Sons, Inc., New York, 2001.
- [132] Y. Xu, *Numerical Calculation of an Axisymmetric Laminar Diffusion Flame with Detailed and Reduced Reaction Mechanism*, PhD Thesis, Yale University, New Haven, Connecticut, 1991.
- [133] Y. Xu and M. D. Smooke, Primitive Variable Modeling of Multidimensional Laminar Flames, *Combust. Sci. Tech.*, **90**, 289-313, 1993.

- [134] C. Zhang, W. Shen, and J. Zhang, Modeling and simulation of FGF-2 transport in capillary with binding and signaling on cell surface, *2007 International Conference on Life System Modeling and Simulation*, Shanghai, China, September 14-17, 2007 (Submitted).
- [135] J. Zhang and J. J. Zhao Unconditionally stable finite difference scheme and iterative solution of 2D microscale heat transport equation, *Journal of Computational Physics*, **170**, 261-275, 2001.
- [136] Y. Zhang, D. B. Goldgof, S. Sarkar, and L. V. Tsap, A modeling approach for burn scar assessment using natural features and elastic property, *IEEE Transactions on Medical Imaging*, **23**, 1325-1329, 2004.

Vita

Personal Data:

Name: Wensheng Shen

Date of Birth: 12/26/1968

Place of Birth: Jinxian, Anhui, China

Educational Background:

- Doctor of Philosophy in Engineering, Tennessee Technological University, 2003.
- Master of Science in Chemical Engineering, South China University of Technology, China, 1996.
- Bachelor of Science in Chemical Engineering, Donghua University, China, 1990.

Professional Experience:

- Research Assistant, 08/2003 - present. Department of Computer Science, University of Kentucky.
- Teaching Assistant, 08/2002 - 05/2003. Department of Mechanical Engineering, Tennessee Technological University.
- Research Assistant, 08/1999 - 07/2002. Department of Mechanical Engineering, Tennessee Technological University.
- Assistant Professor, 04/1996 - 07/1999. Chemical Engineering Research Institute, South China University of Technology, China.
- Research Assistant, 09/1993 - 03/1996. Chemical Engineering Research Institute, South China University of Technology, China.

- Thermal Energy Engineer, 07/1990 - 08/1993. Maanshan Steel and Iron Inc., China.

Awards:

- Fellowship Award, the 7th DOE ACTS Workshop, Lawrence Berkeley National Lab, 2006.
- Presidential Fellowship Award, Graduate School, University of Kentucky, 2006-2007.
- Thaddeus B. Curtz Memorial Scholarship Award, Department of Computer Science, University of Kentucky, 2006.
- Kentucky Opportunity Fellowship Award, Graduate School, University of Kentucky, 2005-2006.
- Young Researcher Fellowship Award, Third MIT Conference on Computational Fluid and Solid Mechanics, Cambridge, MA.
- Student Travel Support, Graduate School, University of Kentucky, 2006-2007.
- Student Travel Support, Graduate School, University of Kentucky, 2005-2006.
- Student Travel Support, Graduate School, University of Kentucky, 2004-2005.
- SIAM Student Travel Award, SIAM, 2004.

Refereed Publications:

- Wensheng Shen, Changjiang Zhang, and Jun Zhang, Multiscale simulation of ligand-receptor binding and dissociation in circulation, *Proceedings of The 45th ACM Southeast Conference*, March 23-24, 2007, ACM, Winston-Salem, NC, pp. 519-520.

- Wensheng Shen, Jun Zhang, and Fuqian Yang, Newton's method for steady and unsteady reacting flows, *Proceedings of the 2006 ACM Symposium of Applied Computing*, ACM, Melbourne, FL, 2006, pp. 756-757.
- Wensheng Shen, Jun Zhang, and Fuqian Yang, Performance of ILUT preconditioners in modeling bioheat and mass transfer in skin thermal injury, *Proceedings of the Third M.I.T. Conference on Computational Fluid and Solid Mechanics*, editor: K.J. Bathe, pp. 1175-1178, Elsevier, 2005.
- Wensheng Shen, Jun Zhang, and Fuqian Yang, Three-dimensional model of thermal response of skin subject to laser heating, *Computer Methods in Biomechanics and Biomedical Engineering*, **8**(2), 115-125, 2005.
- Wensheng Shen, Jun Zhang, and Fuqian Yang, Modeling and numerical simulation of bioheat transfer and biomechanics in soft tissue, *Mathematical and Computer Modelling*, **41**(11-12), 1251-1265, 2005.
- Wensheng Shen, Jun Zhang, and Fuqian Yang, Skin thermal injury prediction with strain energy, *International Journal of Nonlinear Science and Numerical Simulation*, **6**(3), 317-328, 2005.
- W. Shen and S. Han, Two-dimensional hyperbolic heat conduction with temperature-dependent properties, *AIAA Journal of Thermophysics and Heat Transfer*, **18**(2), 285-287, 2004.
- W. Shen and S. Han, A numerical solution of two-dimensional hyperbolic heat conduction with non-linear boundary conditions, *Heat and Mass Transfer*, **39**, 499-507, 2003.
- W. Shen and S. Han, Numerical solution of two-dimensional axisymmetric hyperbolic heat conduction, *Computational Mechanics*, **29**, 122-128, 2002.

- W. Shen and S. Han, An explicit TVD scheme for hyperbolic heat conduction in complex geometry, *Numerical Heat Transfer (Part B)*, **41**, 565-590, 2002.
- W. Shen and S. Han, Hyperbolic heat conduction in composite materials, *8th AIAA/ASME Joint Thermophysics and Heat Transfer Conference*, St. Louis, Missouri, AIAA paper 2002-3003, 1-8.

Professional Affiliations:

- Member, Society for Industrial and Applied Mathematics (SIAM)
- Member, American Society for Engineering Education (ASEE)